KU LEUVEN

FACULTEIT INGENIEURSWETENSCHAPPEN

Analysis of the cyclic behaviour of steel fibre reinforced concrete

Eline Vandecruys

Thesis voorgedragen tot het behalen van de graad van Master of Science in de ingenieurswetenschappen: bouwkunde, optie Civiele techniek

Promotoren:

Prof. dr. ir. L. Vandewalle
Prof. dr. ir.-arch. E. Verstrynge

Assessoren:

Prof. dr. ir. S. François
Dr. ir. R. Vrijdaghs

Begeleider:

Ir. M. De Smedt

Academiejaar 2020 – 2021

Preface

Deze thesis is het resultaat van een jaar lang onderzoek naar staalvezelbeton, akoestische emissie en sectieanalyse. Dit onderzoek vervolledigt mijn opleiding als burgerlijk ingenieur bouwkunde, met als optie civiele techniek. De drijfveer voor het kiezen van dit onderwerp is vooral mijn sterke interesse in bouwmaterialen. Aangezien de opleiding de meest gebruikelijke bouwmaterialen al omvat, leek deze masterproef mij een unieke kans om ook een meer innovatief materiaal te analyseren.

Graag wil ik gebruik maken van dit voorwoord om enkele personen te bedanken die me hebben bijgestaan tijdens het schrijven van mijn masterproef. Zonder mijn promotoren Lucie Vandewalle en Els Verstrynge was dit onderzoek niet mogelijk geweest. De gedrevenheid van beide professoren gedurende de lessen “Beton 1”, “Sterkteleer 1” en “Renovation of structures” heeft mij overtuigd om dezelfde richting in te slaan, met als resultaat een zeer boeiende masterproef.

Verder was ook Maure De Smedt een grote steun gedurende dit project. Niet enkel kon ik dagelijks bij haar terecht met vragen, ze heeft me ook bijgestaan bij het uitvoeren van de verschillende experimentele testen en deze afgerond wanneer het coronavirus roet in het eten gooide. Hierbij dienen ook techniekers Bernd en Jan vermeld te worden, wiens mankracht duidelijk nodig was bij het uitvoeren van de testen. Daarnaast heeft Rutger Vrijdaghs me telkens opnieuw geholpen met het implementeren van het model in MATLAB, en me zo vaak gerustgesteld.

Naast de academische steun binnen het departement bouwkunde, hebben ook mijn vrienden en familie veel mentale steun geboden gedurende deze uitdagende studies. Vooral mijn ouders zijn een grote hulp geweest tijdens de voorbije jaren. Bedankt papa, om mijn eerste interesse op te wekken voor staalvezels. Jouw passie en fierheid gaven me telkens weer goede moed om het beste van mezelf te geven. Mama wil ik vooral bedanken voor haar luisterend oor, behulpzaamheid en dagelijkse wandelingetjes. Zonder jouw aandringen had ik waarschijnlijk nooit meer mijn bureau verlaten.

Tot slot verdienen ook Jan, Jana, Justine, Kato, Lucie, Mathilde, Menno en Seppe een plaatsje in dit dankwoord. Hoewel we onze studies niet hebben kunnen afsluiten zoals we gehoopt hadden, ga ik al onze leuke tijden samen blijven koesteren. Dankzij jullie kwam ik altijd met plezier naar de les en is het studentenleven zo veel leuker geworden.

Eline Vandecruys

Contents

Abstract

The aim of this research is to analyse the cyclic behaviour of steel fibre reinforced concrete. Since only few codes are established concerning the material, this study tries to contribute to the current knowledge. Steel fibre reinforced concrete optimises the cyclic behaviour of plain concrete by increasing its residual tensile strength. This is achieved by bridging cracks and dissipating energy, which is further investigated.

First of all, experiments have been carried out on concrete with different fibre types and fibre volumes. These tests include both monotonic and cyclic loading of the material. Strain - stress diagrams are therefore composed during direct tensile testing and flexural testing in order to gain a better understanding of the properties of the material. Additionally, acoustic emission sensors are added to the test setup to study the signals emitted by the propagation of cracks. The received waves contain a lot of information about the amount of damage, the damage process, and the location of the crack.

Subsequently, a model is established using these results to predict the behaviour of steel fibre reinforced concrete. This model is based on sectional analysis, which divides the cracked section into several layers. In each of these layers, a uniform stress is assumed to approximate the non-uniform stress profile. Imposing the force and momentum equilibrium then results in the correct stress profile. This principle is first applied to monotonic bending tests. When the difference between the experimental results and the modelled results is minimised, a constitutive equation can be derived and verified with the experimental tensile tests.

Finally, the cyclic behaviour is modelled using the constitutive equations and the experimental results. The same principle is used as before, but with a different input. The external force now decreases at several crack widths. Because of the repeated loading, the tensile stresses depend on the damage introduced in the specimen during the previous load steps. The damage reduces the tensile stresses. This effect is quantified in two ways. First, the stiffness during unloading and reloading is determined from the experimental tensile tests, which can be related to the damage. In addition, the damage is also derived from the crack width after unloading. This value appears to be independent of the fibre type and volume, therefore the cyclic behaviour can be deduced from only the monotonic bending tests and the equation that determines the plastic crack width.

Samenvatting

Het doel van dit onderzoek is het analyseren van het cyclische gedrag van staalvezelbeton. Aangezien weinig normen zijn opgesteld over dit materiaal, probeert deze studie bij te dragen aan de huidige kennis. Staalvezels optimaliseren het cyclische gedrag van beton door het nascheurgedrag te verbeteren. Dit wordt gerealiseerd door het overbruggen van scheuren en het dissiperen van energie, wat verder is onderzocht.

Eerst en vooral zijn experimenten uitgevoerd op beton met verschillende vezeltypes en vezelvolumes. Deze testen omvatten zowel het monotone als het cyclische belasten van het materiaal. Spanning - rek diagrammen zijn bijgevolg opgesteld gedurende trek- en buigtesten om een beter inzicht te krijgen in de eigenschappen van het materiaal. Ook akoestische emissie sensoren zijn toegevoegd aan de testopstelling om de signalen, uitgezonden door het ontstaan van scheuren, te bestuderen. De ontvangen golven bevatten immers veel informatie over de hoeveelheid aan schade, het schadeproces en de locatie van de scheur.

Vervolgens is met behulp van deze resultaten een model opgesteld om het gedrag van staalvezelbeton te voorspellen. Dit model is gebaseerd op sectie-analyse, wat de gescheurde doorsnede opdeelt in verschillende lagen. In elk van deze lagen is een uniforme spanning verondersteld die het niet-uniforme spanningsprofiel benadert. Het eisen van een krachten- en momentenevenwicht resulteert dan in het juiste spanningsprofiel. Dit principe is eerst toegepast op monotone buigtesten. Wanneer het verschil tussen de experimentele resultaten en de gemodelleerde resultaten wordt geminimaliseerd, kan een constitutieve vergelijking worden opgesteld.

Uiteindelijk is met behulp van de constitutieve vergelijkingen en de experimentele resultaten ook het cyclische gedrag gemodelleerd. Hetzelfde principe is gebruikt als voorheen, maar met een verschillende input. De uitwendige kracht gaat nu bij enkele scheurwijdtes dalen. Hierdoor hangen de trekspanningen af van de schade die geïntroduceerd is in het proefstuk tijdens de voorgaande belasting. Deze schade doet de trekspanningen dalen. Dit effect is gekwantificeerd op twee manieren. Eerst is de stijfheid gedurende de cycli bepaald uit de experimentele trektesten, die gerelateerd is aan de schade. Daarnaast is de schade ook berekend afhankelijk van de scheurwijdte die het proefstuk bevat op het einde van ontladen. Deze blijkt onafhankelijk te zijn van het vezeltype en vezelvolume, waardoor het cyclische gedrag kan worden afgeleid uit enkel de monotone buigtesten en de vergelijking die de plastische scheurwijdte bepaalt.

List of Figures

List of Tables

List of Abbreviations

3PBT	Three-point bending test
AE	Acoustic emission
AF	Average frequency
CMOD	Crack mouth opening displacement
DTT	Direct tensile test
EN	European standard
fib	Fédération internationale du béton
FRC	Fibre reinforced concrete
LOP	Limit of proportionality
LR	Load ratio
LVDT	Linear variable differential transformer
MC2010	Model Code 2010
NDT	Non destructive technique
ppp	Post-peak points
PZT	Piezoelectric transducer
RA	Rise angle
SFRC	Steel fibre reinforced concrete
SLS	Serviceability limit state
ULS	Ultimate limit state
UTT	Uniaxial tensile test

List of Symbols

$\bar{\square}$	Mean value
$\hat{\square}$	Value calculated with linear regression
α	Orientation factor of fibres
A_f	Cross-sectional area of a steel fibre
A_n	Cross-sectional area of the notched section
A_s	Cross-sectional area of a specimen
b	Width of a cross-section
$CMOD$	Crack mouth opening displacement at a height of $y = 0\,mm$
$CMOD_y$	Crack mouth opening displacement at a height of y
δ	Displacement
δ_{top}	Displacement of the top fibre of the section
D	Damage
ε	Strain
ε_{pl}	Plastic strain
E_{ci}	Tangent modulus of elasticity of concrete
E_{cm}	Mean secant modulus of elasticity of concrete
f_{ck}	Characteristic value of the cylindrical compressive strength
f_{cm}	Mean value of the cylindrical compressive strength
$f_{cm,cube}$	Mean value of the cube compressive strength
f_{ctm}	Mean value of the uniaxial tensile strength
f_{Fts}	Tensile stress when $w = 0.5\,mm$
f_{Ftu}	Tensile stress when $w = 2.5\,mm$
$f_{k,ln}$	Characteristic strength, assuming a log-normal distribution
f_L^f	Limit of proportionality (LOP)
$f_{m,ln}$	Mean strength, assuming a log-normal distribution
f_{Rj}	Residual flexural tensile strength for $\mathrm{CMOD_j}$
f_{Rjk}	Characteristic flexural tensile strength for $\mathrm{CMOD_j}$
F_{ext}	Externally applied load
F_i	Load at $\mathrm{CMOD_i}$
F_L	Load corresponding to the LOP
G_F	Fracture energy

h	Height of the specimen
h_j	Height of layer j in the sectional analysis
h_{sp}	Remaining height at location of the notch
ΔH_i	Error of horizontal equilibrium at CMOD_i
K	Stress intensity factor
K_0	Stiffness of the uncracked specimen
K_i	Stiffness of the cracked specimen
K_{ul}	Stiffness during unloading
l_{cs}	Characteristic length of the structural element
L	Length of the specimen
m	Amount of layers in the sectional analysis
M_{ext}	Externally applied bending moment
$M_{ext,i}$	External bending moment at CMOD_i
$M_{int,i}$	Internal bending moment at CMOD_i
ΔM	Error of momentum equilibrium summed over all CMOD_i
ΔM_i	Error of momentum equilibrium at CMOD_i
n	Amount of test specimens
n_f	Nominal amount of fibres in the cross-section
N	Number of loading cycles
N	Discretisation of the range of the points of the constitutive law
N_{CMOD}	Amount of CMODs calculated
N_{loops}	Amount of times the interval is CMOD decreases
N_{top}	Amount of δ_{top} calculated
P	An applied load
P_{AE}	Load at which AE activity is detected
P_{1st}	Maximum load in history
r^2	Coefficient of determination
σ	Stress
σ_j	Mean stress in layer j
$\sigma_{j,i}$	Mean stress in layer j at CMOD_i
s	Standard deviation
s_{ln}	Standard deviation, assuming a log-normal distribution
S	Stress level
V_f	Fibre volume fraction
w	Crack width
w_{pl}	Plastic crack width at the end of unloading
w_{tu}	Crack opening at peak stress
w_{unl}	Crack width at the start of unloading
y	Height measured from the bottom of the beam
y_j	Height of layer j, measured from the bottom of the beam
y_N	Height of the neutral axis, measured from the bottom of the beam

Chapter 1

Introduction

1.1 Problem statement

Concrete is one of the most widely used materials in civil engineering because of its high compressive strength and low cost. The use of concrete is still increasing and the material is evolving. However, an important drawback is the almost nonexistent tensile strength. Due to this limitation of concrete, cracks can easily be formed when a structure is subjected to bending or tensile forces. In recent years, flexural and tensile tests have shown that the residual tensile strength of concrete can improve by adding fibres to the cement mixture. The propagation of cracks is retained by the fibres that bridge the cracks and absorb energy, resulting in an improved post-cracking behaviour. The material becomes more ductile and the disadvantages of the brittle material fade.

For cyclic loading, the initiation of cracks becomes more significant because the material permanently deteriorates. Irreversible strains are introduced in the material and the stiffness decreases. This effect is commonly referred to as fatigue. Extensive research has shown that the addition of fibres to the concrete mix can enhance the resistance against fatigue failure. Because the performance of lots of concrete structures depends on the cyclic behaviour due to repeated loads (e.g. bridge decks, industrial pavements, structures in earthquake-prone areas), fibres can prolong their lifespan.

Recently, there has been an increasing interest in detecting the fatigue damage in structures, due to the great number of concrete buildings and other civil engineering structures reaching the end of their lifetime. Because of their broad life span, fatigue failure is more likely to occur. To detect the internal cracks, and therefore the induced damage in the structure, the promising non-destructive technique (NDT) *Acoustic Emission testing* (AE) is proposed. Sensors can be attached to the structure, continuously measuring the waves sent from crack propagation. When the internal damage cannot be visually observed, AE sensors are already able to detect the problem, by relating AE parameters to the damage process. Therefore, AE testing is used in this study to measure the cyclic behaviour of fibre reinforced concrete (FRC).

1.2 Objectives

Because FRC has only been used in the last decades, few codes are established involving the design of fibre reinforced structures. The lack of information stimulates the need for more research on the topic of fibre reinforced concrete, to maximise its potentials in the construction sector. This study provides new insights into the cyclic behaviour of steel fibre reinforced concrete (SFRC), measured with acoustic emission. Hence, the main objective of this thesis is: "How does steel fibre reinforced concrete behave under cyclic loading?".

The answer is found in two different ways. The first method is by performing sectional analysis, based on the results of a three-point bending test, and damage curves. By fulfilling the equilibrium equations in the cracked section during the three-point bending test, the constitutive law of the material can be derived and therefore the monotonic tensile behaviour. Next, cyclic tensile tests are performed to obtain the damage curves. Combining both results, the cyclic tensile and flexural behaviour is predicted. Therefore, a first research subquestion is added: "Can the cyclic behaviour of steel fibre reinforced concrete be modelled?". The results of the model are compared to experimental results to verify the sectional analysis. Secondly, the AE results of a cyclic tensile test are used to estimate the cyclic behaviour as well. The parameters of the waves sent from crack propagation are correlated to the damage of the material. Hence, the behaviour of SFRC inside the material can be understood, resulting in improved insights into the failure mechanism. Therefore, the second research subquestion is: "How do the parameters of AE signals relate to the damage in the material?".

1.3 Outline of the text

Chapter 2 of this thesis contains a literature study, to obtain a general understanding of the above-mentioned topics. The current knowledge of both SFRC and AE testing is discussed. Afterwards, the test-setup and obtained experimental results are reviewed in Chapter 3. It contains results from bending tests, which are performed in a previous study [17, 19], as well as the results of a direct tensile test, performed during this study. Both monotonic and cyclic loading of the test specimens is executed. The mechanical and AE results are discussed and compared for different fibre types and volumes. Chapter 4 then provides a method to predict the results of a direct tensile test, by only performing a three-point bending test. Two models are proposed based on sectional analysis to obtain both the monotonic and cyclic behaviour of the material. Further, a comparison with the experimental results is made to verify the models, and a sensitivity study analyses the effect of all parameters used in the model. Lastly, Chapter 5 concludes this thesis with the most important results and suggestions for further research.

Chapter 2

Literature study

Concrete structures are often exposed to repeated loading and could therefore suffer fatigue problems. Previous studies state that the addition of fibres to a concrete matrix improves the resistance to repeated loading [40, 52]. The formation of micro-cracks in concrete structures due to cyclic loading can be detected with an acoustic emission (AE) technique, without damaging the structure. This thesis consists of the above-mentioned topics, which have been studied before, but not necessarily together. A literature study is performed to create a better understanding of the core of the thesis and comparable recent studies. In the next paragraphs, a summary of the most important information found in literature is given.

Section 2.1 discusses steel fibre reinforced concrete (SFRC). A general overview is given on the composite material and its improved behaviour. Also the guidelines provided in the Model Code, different tests, the fatigue behaviour and some applications are discussed. Section 2.2 contains a broad explanation of the operating method of AE testing, the characteristics of AE waves, the measuring system, and the analysis of the output. The literature study ends with a conclusion of the main aspects of this chapter in Section 2.3.

2.1 Steel fibre reinforced concrete

2.1.1 Description of the material

Fibre reinforced concrete (FRC) is a discontinuous material consisting of concrete or mortar and fibres. The main advantage of SFRC is the improvement of the tensile post-peak behaviour, making the material more ductile and limiting the crack width. However, the composite material also has some disadvantages. Introducing fibres to the concrete mixture has a negative impact on the workability, influenced by the fibre volume fraction and type of fibre. Additionally, fibres slightly increase the air content in concrete. This effect can reduce the compressive strength and reduce the bond strength between the fibres and concrete matrix [34]. Further, the surfaced fibres are prone to corrosion and the irregularity of the distribution can cause problems [57]. This thesis focuses mainly on the improvement of the post-peak tensile behaviour.

The behaviour of FRC is most importantly determined by the fibres. These fibres can be made of various materials such as steel, polymers, carbon, glass or natural materials [29] and are randomly distributed throughout the material. Only steel fibres in a cementitious matrix are discussed here: Steel Fibre Reinforced Concrete (SFRC). Next to the material of the fibre, also the physical and chemical properties, as well as the mechanical characteristics and geometry define the composite material. Some examples of fibres are shown in Figure 2.1. The bond between the fibres and concrete can be enhanced by roughening the surface or deforming the fibre [46].

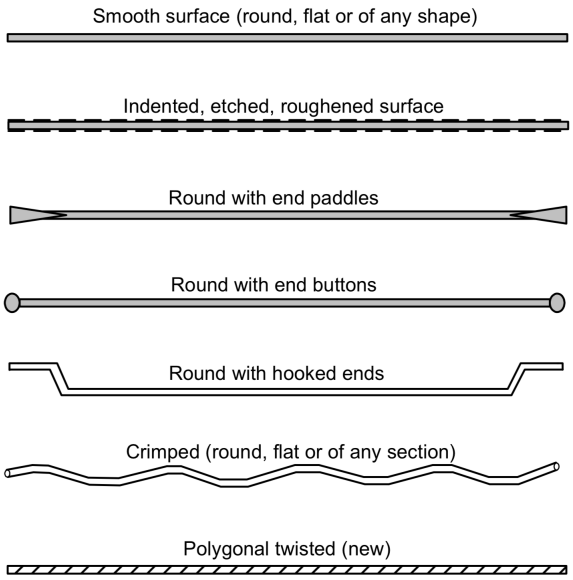

Figure 2.1: Common steel fibres, taken from [46].

The main properties defining the tensile post-peak behaviour of SFRC are the tensile strength, bond strength and elastic modulus of the fibres. The tensile and bond strength need to be higher than the tensile strength of the matrix to make optimal use of the steel fibres. Also the elastic modulus of the fibres needs to be larger than that of the concrete. Further, the fibre volume fraction strongly influences the behaviour of SFRC as well [46].

Depending on the type of steel fibre, they can replace the conventional reinforcement in thin slabs, determined by the ultimate limit state (ULS). On the other hand, fibres can also limit the crack width for the serviceability limit state (SLS). The latter means that the fire resistance increases, the shrinkage cracking reduces and thus the durability improves [22, 29].

The main goal of SFRC in this study is to change the post-cracking behaviour. The material becomes more ductile because the fibres can absorb more energy than plain concrete, and the stresses in the cracked section are redistributed. The most important processes providing this improved behaviour, are the fibre pull-out and the bridging of the cracks [31]. The fibre pull-out absorbs and dissipates energy.

Bridging the cracks reduces the stress at the crack tip, decreasing crack propagation [70]. Figure 2.2 shows all failure mechanisms of FRC. This figure highlights the importance of the tensile strength of the fibres, as well as the bond strength.

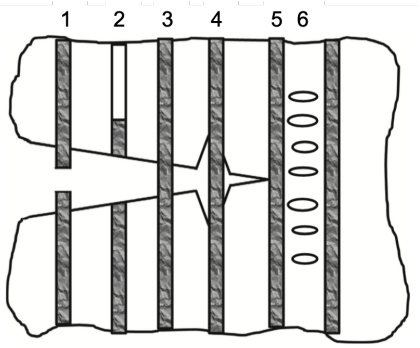

Figure 2.2: Failure mechanisms in fibre reinforced concrete: (1) fibre rupture, (2) fibre pull-out, (3) fibre bridging, (4) fibre/matrix debonding, (5) fibre preventing crack propagation, (6) matrix cracking, taken from [70, 71].

Although the fibres greatly influence the post-cracking behaviour, they do not have a large impact on the pre-cracking behaviour. The compressive and tensile peak strength do not differ from plain concrete [34, 70], as cracks have not yet been formed. The main difference is the post-cracking behaviour, which expresses itself in two different ways, shown in Figure 2.3.

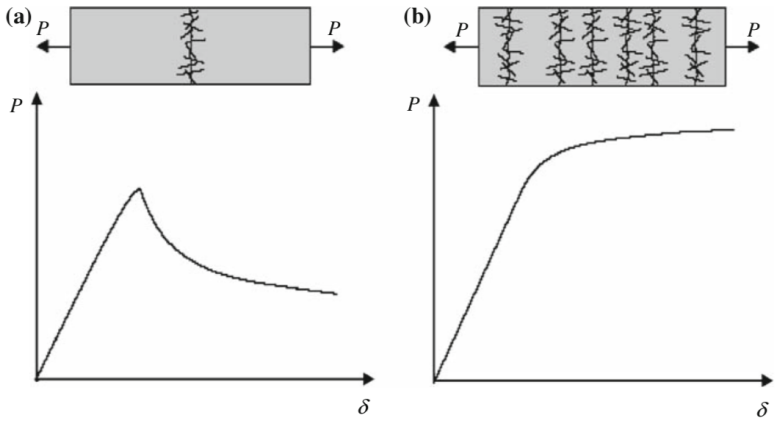

Figure 2.3: Typical load-deformation curve for FRC: post-cracking softening (left) and hardening (right) behaviour, taken from [22].

When the load increases after cracking, the term *hardening* is used. This can happen for high performance concrete and a large volume of fibres [22]. Generally hardening occurs when multiple cracks are generated in the specimen, the energy needed for crack initiation is smaller than crack propagation [37]. However, for notched specimens, this definition cannot be used as multiple cracking is excluded. A single

crack always occurs in the notched section, where the area is smaller and the stresses higher. When hardening occurs in bending, the term *deflection hardening* is used. Hardening in tension is called *strain hardening*. Deflection and strain hardening do not necessarily apply both to a certain material. The fibre volume fraction to obtain deflection hardening is smaller than the volume needed for strain hardening [21, 37]. A material showing hardening behaviour during bending tests can therefore show either a softening or hardening behaviour during tensile tests. For *softening* materials, the strength decreases right after the peak load is reached, and only one crack is formed. This occurs for a lower fibre content.

2.1.2 Model Code

Due to the lack of building codes regarding steel fibre reinforced concrete, the material remains unknown, resulting in a limited use with respect to its potentials. This problem led to the need for more research and codes. The fib Model Code 2010 (MC2010) [29] provides some general guidelines about SFRC and serves as a base for future building codes.

Since the behaviour in compression is in theory the same as for plain concrete, the compressive relations for FRC are the same as the ones used for plain concrete [29, 34]. However, the behaviour in tension will change significantly. This can be determined by a three-point bending test (3PBT) shown in Figure 2.4 and is described in the European Standard: EN 14651 [26]. The results of this test can be expressed in three different ways: the relation between the deformation and crack mouth opening displacement (CMOD), the limit of proportionality and the residual flexural tensile strengths.

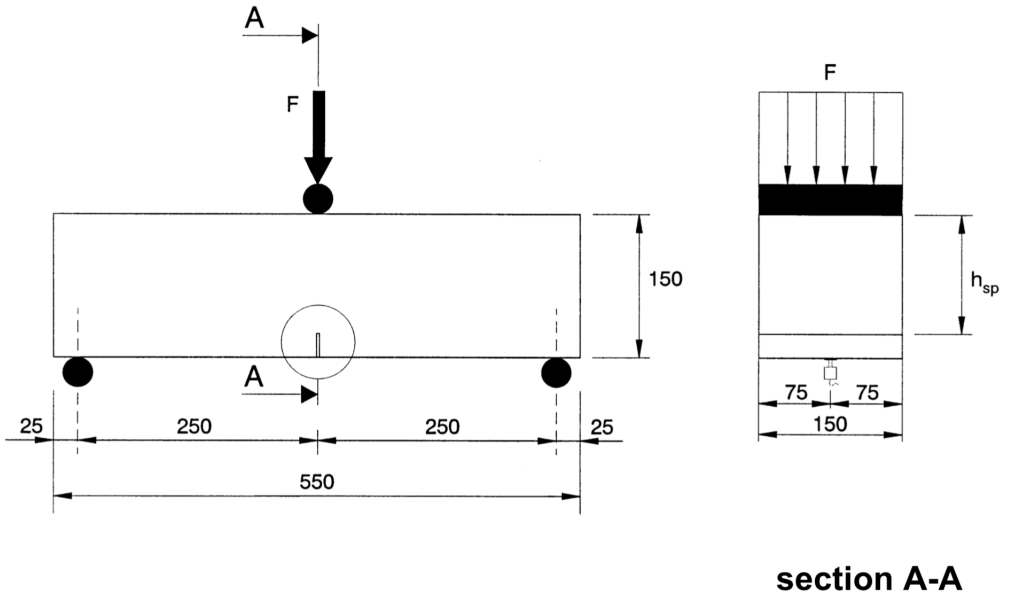

Figure 2.4: Three-point bending test, taken from [26].

The deflection of the specimen is expressed as a function of the CMOD. Both values are related by Equation 2.1. The CMOD in this formula is the crack width measured exactly at the bottom of the specimen. When the measurement is taken at a distance y beneath the beam, Equation 2.2 can derive CMOD from $CMOD_y$ [26].

$$\delta = 0.85 \cdot CMOD + 0.04 \tag{2.1}$$

$$CMOD = CMOD_y \cdot \frac{h}{h+y} \tag{2.2}$$

Next, the limit of proportionality (LOP) indicates the cracking strength or flexural tensile strength. It corresponds to the highest load for a CMOD between $0\,mm$ and $0.05\,mm$, and indicates the moment when tensile macro-cracking starts. The LOP is illustrated in Figure 2.5 and given by the expression [26, 39]:

$$f_L = \frac{3F_L L}{2bh_{sp}^2} \tag{2.3}$$

with

f_L The LOP [MPa]
F_L The load corresponding to the LOP [N]
L The span length [mm]
b The specimen's width [mm]
h_{sp} The remaining height at location of the notch [mm]

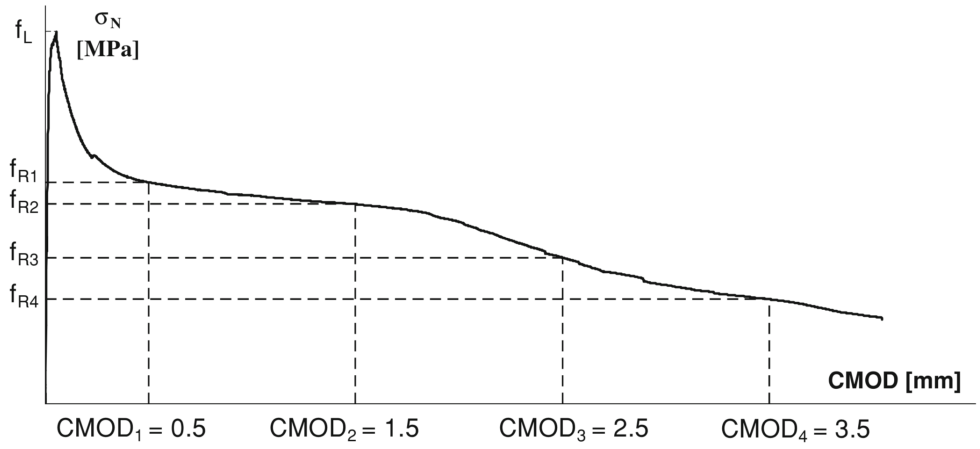

Figure 2.5: Typical curve of the stress versus CMOD for FRC, taken from [22].

When assuming a simply supported beam with a linear stress profile, the post-cracking residual flexural tensile strength can be derived as follows [29]:

$$f_{Rj} = \frac{3F_j L}{2bh_{sp}^2} \tag{2.4}$$

Even though this formula is not valid in the cracked section of the beam due to the assumption of a linear stress profile, it is still used to evaluate the tensile stresses of the beam. Considering the stress profiles sufficiently removed from the crack stay linear, f_{Rj} can still be applied. Most parameters of Equation 2.4 are already explained as this formula is similar to Equation 2.3. The remaining variables are:

f_{Rj} The residual flexural tensile strength for CMOD_j [MPa]
F_j The load at CMOD_j [N]

The classification of SFRC is established with four different residual tensile strengths (f_{R1}, f_{R2}, f_{R3}, f_{R4}), corresponding to CMODs of 0.5, 1.5, 2.5 and 3.5 mm, indicated in Figure 2.5. The strengths f_{R1} and f_{R3} define the tensile residual strength for SLS and ULS, respectively. In addition, the classification needs two inputs [22, 29]:

- The strength class for f_{R1k} (characteristic value), equal to 1.0, 1.5, 2.0, 2.5, 3.0, 4.0, 5.0, 6.0, 7.0 or 8.0 MPa
- The f_{R3k}/f_{R1k} ratio, corresponding to:
  a If $0.5 < \frac{f_{R3k}}{f_{R1k}} < 0.7$
  b If $0.7 \leq \frac{f_{R3k}}{f_{R1k}} < 0.9$
  c If $0.9 \leq \frac{f_{R3k}}{f_{R1k}} < 1.1$
  d If $1.1 \leq \frac{f_{R3k}}{f_{R1k}} < 1.3$
  e If $1.3 \leq \frac{f_{R3k}}{f_{R1k}}$

Both values represent the enhanced post-cracking residual strength of the material, referred to as the toughness. The first value (f_{R1k}) describes the characteristic residual strength in ULS, and the latter value gives the ratio of SLS and ULS residual strength [22].

The Model Code considers the bending test, which is widely used because of its straightforward test setup and execution method [4, 7, 62]. However, deriving the constitutive law is more complicated than for direct tensile tests. Therefore, the Model Code proposes a linear relation for the stress - crack opening relation in uniaxial tension. The relation found in the Model Code and the paper by di Prisco [21], is constructed by using two points, depending on the tensile residual strength for SLS (f_{R1}) and ULS (f_{R3}). Following equations calculate both post-peak points:

$$f_{Fts} = 0.37 \cdot f_{R1} \tag{2.5}$$

$$f_{Ftu} = 0.5 \cdot f_{R3} - 0.5 \left(0.529 - 0.143 \frac{f_{R3}}{f_{R1}}\right) \cdot f_{R1} \tag{2.6}$$

The values f_{Fts} and f_{Ftu} resemble the stresses in the σ-w curve for w equal to 0.5 and 2.5 mm respectively. Figure 2.6 illustrates this linear relation, where $k_a = 0.37$ and $k_b = (0.529 - 0.143 \cdot f_{R3}/f_{R1})$. It should be noted that the tensile strength of the plain concrete, before cracking, is not taken into account with these equations. Only the influence of the fibres is illustrated in the figure.

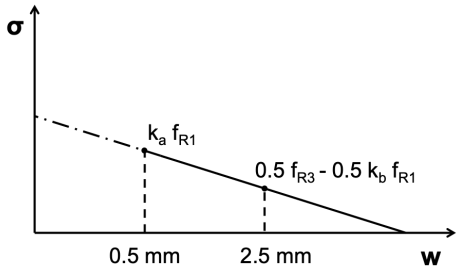

Figure 2.6: Post-peak constitutive law, adapted from [21].

2.1.3 Testing the tensile behaviour

Pull-out test

In a pull-out test, an individual fibre is pulled out of a concrete matrix. This can be executed to measure the influence of the geometry and inclination of the fibre. The process of pulling the fibre out of the concrete matrix can be observed and divided into four stages [55]. The first stage is the debonding stage, when the chemical anchorage between the matrix and the fibre reduces. In the second stage, the mechanical anchorage of the hooked ends of the fibres diminishes and the fibres deform after reaching the peak load. Energy is dissipated trough plastic deformation and friction between the fibres and concrete matrix. The third stage is when the fibre slides trough the matrix. Resistance, and therefore energy dissipation, is provided by the friction between the steel fibre and concrete matrix. In the last stage, the fibre is pulled out. All stages are indicated in Figure 2.7, where region I is enlarged for clarity.

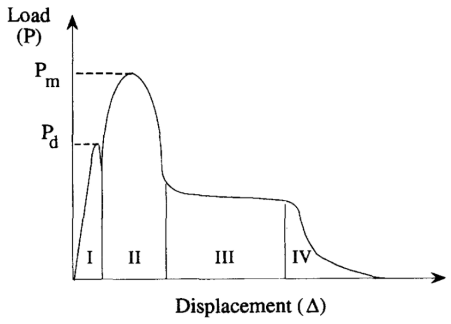

Figure 2.7: Typical load-displacement curve for fibres, taken from [55].

The type of fibre has a large influence on all stages of the fibre pull-out. The longer the fibre, the better the chemical anchorage (phase 1), and the longer the friction stage (phase 3). The more end-hooks the fibre contains, the larger the mechanical anchorage (phase 2) [18, 55]. This behaviour at a smaller scale provides better understanding of the total tensile behaviour of SFRC, measured with a 3PBT or direct tensile test.

Direct tensile test

Because adding steel fibres to the concrete matrix mostly affects the post-cracking tensile behaviour, obtaining the tensile mechanical behaviour is of great interest. A three-point bending test as described in Section 2.1.2 has some drawbacks because of the non-uniform stress distribution, complex multiple cracking and the complicated process to obtain the constitutive law from the flexural behaviour [32]. Performing a direct tensile test (DTT) is ideal because of the uniform stress distribution and clear interpretation. However, the results strongly depend on the test setup and boundary conditions [67]. The main technical problems are the alignment of the specimen, the manufacturing of the specimen and the gripping problem [65]. Therefore, DTTs or uniaxial tensile tests (UTTs) are not often performed on concrete specimens.

The goal of the DTT is to obtain the stress - crack opening (σ-w) curve. The stress is obtained by dividing the applied force by the area of the notched section [58]:

$$\sigma = \frac{P}{A_n} \tag{2.7}$$

The crack opening (w) can be derived from the displacement measurements (δ_j), with $\bar{\delta}_p$ the average displacement at peak stress and n the amount of measuring systems [58]:

$$\bar{\delta} = \frac{1}{n}\sum_{j=1}^{n}\delta_j \tag{2.8}$$

$$w = \bar{\delta} - \bar{\delta}_p \tag{2.9}$$

In the σ-w curves of the individual displacement measurements, the technical problem of the alignment of the test specimen is often observed. The individual σ-w curves generally show significant differences for small displacements because of non-symmetric crack propagation. The crack initiates and propagates further through the notched section resulting in an asymmetric crack. However, the influence of this irregularity is negligible because no problems occur for larger displacements [6]. Figure 2.8 illustrates this phenomenon. The crack initiates close to the linear variable differential transformers (LVDT) number 3, as δ_3 is largest after reaching the peak load. When further increasing the displacement, the other side of the specimen is even compressed, as δ_1 becomes smaller. After some time, the reverse is observed. Displacements δ_1 and δ_2 become larger as δ_3 becomes smaller. The equal crack opening throughout the whole section is restored [45].

Because this thesis only considers notched specimens, they are prone to the above-mentioned effect. However, notched specimens are preferred because the crack occurs in the notched cross-section due to the smaller area, and multiple cracking does not take place. This means that LVDTs placed over the notch are able to measure the crack opening. Also clip gauges are a possible way to determine the crack width at the notch. However, this notched section may not be the weakest section and possibly results in an overestimation of the post-cracking strength [37].

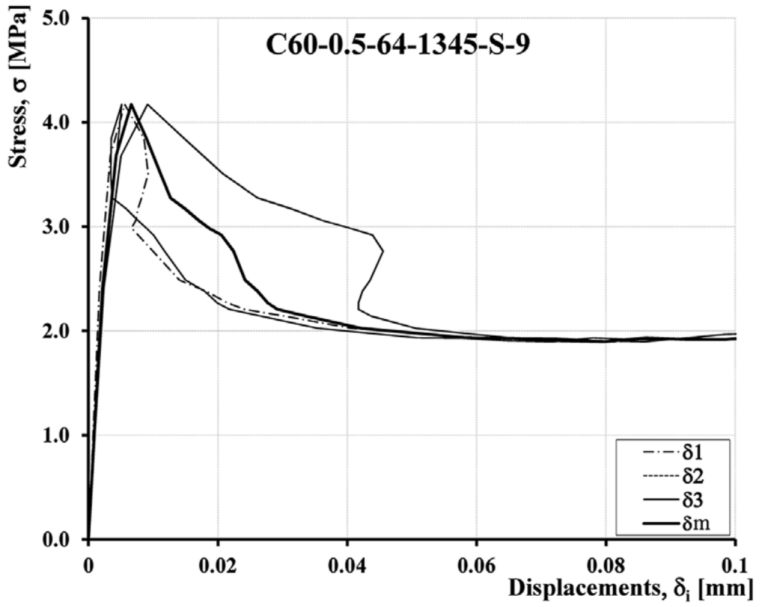

Figure 2.8: Stress versus individual displacement diagram from a typical test with 3 LVDTs, taken from [45].

2.1.4 Fatigue

Overview on the fatigue behaviour

Next to the improved post-peak behaviour during monotonic loading, another advantage of SFRC is the increase in lifetime under cyclic loading. Lots of structures suffer from fatigue problems due to traffic, wind, waves and other repeated loads. The cyclic loading leads to permanent internal structural changes, decreasing the stiffness of the material. Fatigue failure happens in three stages. First the cracks initiate in the weak regions. Secondly, the cracks evolve to micro-cracks. Finally a continuous macro-crack develops, leading to failure. Fibres can elongate the second stage, bridging the cracks and increasing the energy absorption [31, 40, 52]. This growth of a fatigue crack can be illustrated by the Paris' law. In Figure 2.9, a indicates the advancement of the crack, N is the amount of loading cycles and K is the stress intensity factor [56].

The existing literature is not always in agreement about the fatigue behaviour of SFRC. Two causes are mentioned regarding the conflicts in information. First of all, due to the lack of standards about the test procedure, various studies cannot be compared properly. Only general trends can be observed between the different data, using normalised S-N or Wöhler curves. In these curves, a stress ratio (S) is expressed as a function of the number of cycles to failure (N). This stress ratio is the upper load level divided by the maximum static load, making the curve dimensionless and independent on influences concerning the geometry, composition, curing conditions etc. of the concrete [37, 40]. For a certain stress ratio S, the

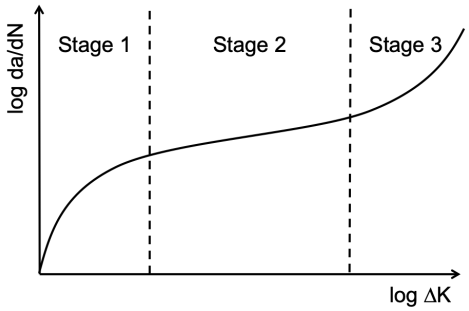

Figure 2.9: Schematic demonstration of Paris' law, adapted from [56].

number of cycles N increases up to failure. The experiment can be done for several values of S, resulting in a Wöhler curve. An example of such a curve is given in Figure 2.10, composed from several studies found in literature. The graph compares the S-N curves of plain concrete and SFRC under flexural loading and compression.

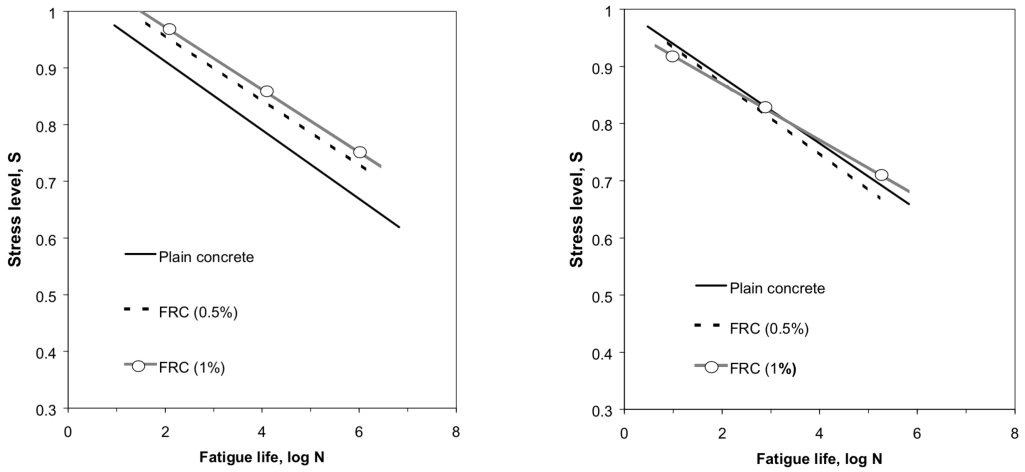

Figure 2.10: Comparison between S-N curves for plain concrete and SFRC (0.5% and 1.0% fibre content) under flexural loading (left) and compression (right), taken from [40].

The simplest version of the Wöhler curves is a power law, corresponding to following formula [59]:

$$S = a \cdot N^b \tag{2.10}$$

Where a and b are both material parameters. Equation 2.10 can predict the fatigue life of structures by calculating the amount of cycles until failure. These curves are a useful way to compare data from different studies. However, the load amplitude needs to be constant, which is never the case in real structures. Another disadvantage is the large amount of data and statistical analysis needed to predict the behaviour [48].

The second point of conflict involves the contradictory effects due to the addition of fibres to the mixture. The positive effect is that the fibres can bridge the micro-cracks, retarding their growth. This can be beneficial for specimens under tension. A general improvement in fatigue life is observed for specimens containing fibres, as illustrated in Figure 2.10. However, the fibres cause more pores and initial micro-cracks inside the concrete, making the material more sensitive to crack initiation. The parameter contributing most to these effects is the volume of fibres added [40]. Figure 2.10 illustrates this effect in the right graph. In compression, the fatigue life of SFRC can decrease due to these additional flaws. The positive effects such as crack bridging and fibre pull-out are not relevant for a specimen under compression. The same effect has been observed by Cachim et al. [12]. For bigger fibres, the initial micro-cracks are larger, and the fatigue life under compression for FRC is shorter than that for plain concrete.

There is also no agreement in literature on the existence of a possible fatigue limit. This means that for stress ratios under a certain limit, the amount of cycles until failure will reach infinity. The existence of such a limit can seriously enhance the use of SFRC. For instance, the applications which are mentioned in Section 2.1.5 such as bridges, industrial floors and airports, undergo cyclic loading. When the fatigue limit does not exist, failure after a certain amount of cycles is guaranteed. Li and Matsumoto [43] claim the existence of this limit for SFRC, thus introducing a significant added value to the material. However, 10^7 cycles need to be performed to confirm this statement [40].

Damage evolution

To estimate the damage of the structure, before failure, a simple method is proposed. The damage increases with the amount of loading cycles the specimen has endured, and therefore the stiffness decreases. The damage can thus be described by the loss of stiffness in the structure [11, 54]:

$$D = 1 - \frac{K_i}{K_0} \tag{2.11}$$

The stiffness of the uncracked specimen is denoted as K_0, and the stiffness of the cracked specimen during a certain loading cycle is K_i. The latter value decreases after every load cycle. The damage D becomes 1 when the stiffness is 0, and the damage is 0 when the specimen is not cracked.

Uniaxial tensile fatigue behaviour

Numerous studies about the cyclic behaviour of FRC under compression have been carried out [1, 12, 42]. The main conclusion of these studies is that the monotonic curves of compressive tests can be taken equal to the envelop curve of the cyclic tests. Tanigawa and Hatanaka [63] even successfully modelled the hysteretic characteristics of SFRC under compression. Next to the compressive behaviour, also the fatigue behaviour for flexural loading has been examined extensively [31, 40, 52, 57]. However,

the research on tensile cyclic behaviour is limited due to the several practical issues mentioned before.

Chen [14–16] introduced a constitutive model on the direct tensile post-peak cyclic behaviour of plain concrete, taking into account the hysteretic behaviour of the loading cycles. Paschalis and Lampropoulos [53] proposed a constitutive model for axial cyclic loading of FRC. Additionally, Li [41] modelled the direct tensile behaviour of SFRC under cyclic loading, extending the test setup with acoustic emission sensing. The main conclusion drawn from these studies is that the envelope curve of the cyclic tests can be taken equal to the monotonic direct tensile test, as concluded for the compressive behaviour as well. The cyclic tests never heavily exceed or deviate much from the monotonic tests. Secondly, the plastic strain is found to be independent on the fibre volume fraction and characteristics, as schematically indicated in Figure 2.11. Therefore, the monotonic curves and plastic strains can determine the elastic stiffness of the specimen, and consequently also the damage of the specimen.

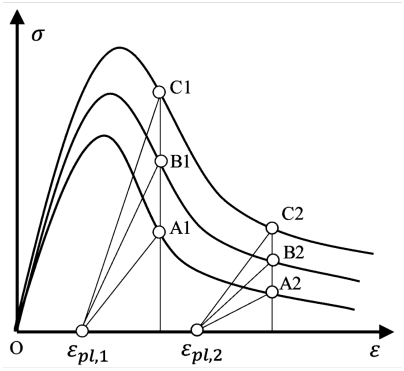

Figure 2.11: Plastic strain and elastic stiffness for various concrete mixtures, taken from [41].

2.1.5 Applications

Because of the lack of standards and building codes, SFRC has a limited use, especially in structural applications. This section covers some applications that already have been implemented in civil engineering structures [44, 67].

Thin slabs are currently the main application of SFRC. The conventional reinforcement can be completely or partially replaced by steel fibres. This results in thinner slabs with higher durability. The fibres bridge the cracks and therefore reduce their width, improving the durability. These slabs are generally used at places with high loads such as bridges, industrial pavements and airports [61].

When the structure is locally subjected to a high force, the local addition of steel fibres can be an economically efficient way to deal with the high stresses. Elevated slabs resting on piles [20], tunnel linings [13], prestressed beams or driven piles are

examples of concrete elements with increased stresses [44]. Adding fibres to those areas improves the strength of the structure.

All structures subjected to cyclic loading can be reinforced with steel fibres as well, such as offshore installations, bridge girders and again deck slabs [52]. As explained in section 2.1.4, fibres can enhance the fatigue life of structures with repeated loading.

Finally, some other applications are mentioned here as well. For instance structures exposed to temperature or moisture change, risk the initiation of cracks, which can be controlled by fibres [44]. Structures in earthquake-prone areas can be strengthened by fibres too [30]. The long-lasting repair of deteriorating infrastructure is the last application mentioned here [5]. Many more uses of FRC exist or will be invented in the future, but they all have in common that the durability and lifetime of the structure will be improved.

2.2 Acoustic emission

2.2.1 General operating method

Concrete buildings that were built years ago, are ageing and show some deterioration. This problem asks for a way to quantify the damage of the building, and to monitor crack development. By being able to determine the damage of the structure, the remaining capacity can be estimated. Acoustic emission is a way to accomplish such results.

Signals are sent from a source due to the release of energy, which can be measured at the surface. The crack formation is the source, which results in a stress wave and produces local deformation. The elastic waves travel through the material to the sensor, which converts the waves into electric signals [33, 48]. This is the main idea of acoustic emission. It is also called micro-seismology because of the resemblance with seismology [33].

To monitor structures such as bridges, AE can be used due to two main characteristics. Firstly, the structure can be in use while performing the test [48]. This means long-term, continuous measurements can be executed. Secondly, AE is a technique to monitor the cracking of concrete without breaking the specimen, a non-destructive technique (NDT). More specifically, it is a passive non-destructive technique because the source is localised inside the material. The source originates from the cracks which arise during loading. Therefore, the cracks that are already present in the material, cannot be measured [33]. However, the main disadvantage of this technique is the complex interpretation. The analysis of the results is more difficult than for other techniques. Also every structure and measuring system behaves differently, creating a different response [68].

In the next paragraphs, some important characteristics of the AE signals are listed (Section 2.2.2), different sensors are explained together with filters and amplifiers (Section 2.2.3) and the analysis of the signals is described (Section 2.2.4).

2.2.2 Characteristics

AE signals are elastics waves, produced by the elastic deformation of a solid material. It is important to notice that they are not acoustic waves, contrary to what the name suggests. The most essential characteristics of an AE signal are listed in this paragraph [33]. Some parameters are clarified in Figure 2.12 as well.

- Hit: The signal reaches a hit when the amplitude exceeds a set threshold.
- Event: When a group of hits, generated by the same source, is detected by more then one sensor [50].
- Count: The number of times the signal exceeds the threshold.
- Amplitude: The magnitude of the wave, expressed in decibel.
- Duration: The time between the first and final exceeding of the threshold.
- Rise time: The time between the exceeding of the threshold and reaching the peak amplitude.
- Energy: The area under the envelope of the signal.

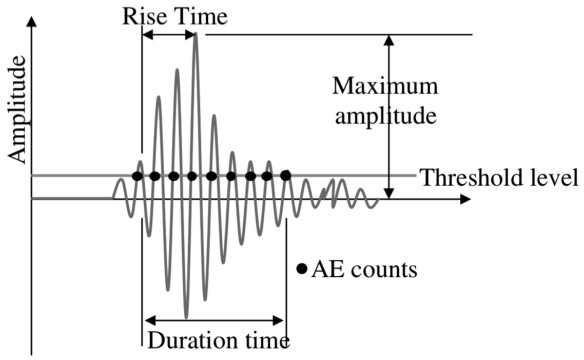

Figure 2.12: AE parameters in a AE hit, taken from [49].

Some other definitions are useful as well, as they are often used in literature. They are calculated by using the previously defined characteristics and contain no new information [33].

- Average frequency (AF): Count/Duration
- Initial frequency: Count to peak/Rise time
- Reverberation frequency: (Count − Count to peak)/(Duration − Rise time)
- Rise angle (RA): Rise time/Amplitude

2.2.3 Measuring system

The measuring system is shown in Figure 2.13. The sensors, amplifiers and filters are further elaborated in this section.

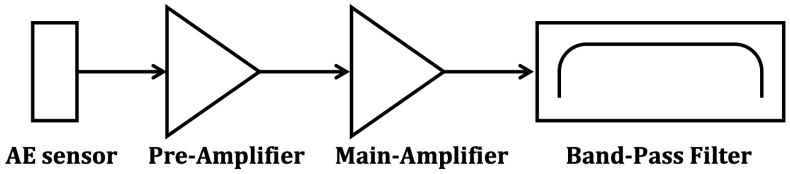

Figure 2.13: AE measuring system, adapted from [50].

Sensors

When energy is released inside the specimen, it is converted into cracks and elastic waves, or AE waves. Sensors detect the elastic waves and transform them into electric signals. The transformation of the signal can happen in two different ways, with two different types of sensors [33]. Resonance-type sensors are the most sensitive ones. They record the signals in a certain frequency range, which is determined in advance. The frequency range is limited, so it is hard to distinguish the different sources of the signal, which send signals at different frequencies. The second type is a broad-band sensor, which detects more frequencies, but is less sensitive. The advantage of this sensor is that it has a flat response and does not change the input as much as the resonance-type sensor does [33, 50].

The amount of sensors used, depends on the application and how accurate the results need to be. With four sensors, the source can be localised in 3D, one dimension less than the amount of sensors used. The difference in arrival time of the signals at the different sensors indicates the location of the source [33]. Additional sensors can improve the accuracy of the result. The setup of the sensors depends on the executed test.

Amplifiers

Because the waves attenuate inside the specimen, the signals themselves are not strong enough and amplifiers are needed. Figure 2.13 shows two amplifiers, as are used in most cases. The internal noise must be low enough, and the devices should be robust. The increase of both amplifiers in concrete is 20 dB - 40 dB with [50]:

$$dB = 20 \cdot log_{10}\left(\frac{V_0}{V_i}\right) \tag{2.12}$$

V_0 in this equation is the output voltage and V_i is the input voltage. The function of the pre-amplifier is to compensate the loss of voltage between the sensor and the recording instrument [48].

Filters

To make sure the noise of the environment is cancelled out, a threshold level is implemented in the sensors. When the signal reaches this threshold, a *hit* is detected. When the signal stays below this value, nothing is registered. In concrete, this threshold level is between 30 dB and 50 dB [50]. Also a band-pass filter is needed to cancel the noise, indicated in Figure 2.13. A band-pass filter between 10 kHz and several 100 kHz is generally used in concrete [50].

2.2.4 Analysis

There are two different ways to analyse and store AE signals. The first one is a signal-based technique, the whole signal is stored and therefore requires lots of memory space. The second technique is parameter based, only some parameters are stored, with which the signal can be reconstructed. This technique contains less information, but the signal reproduces faster [33].

The latter technique will be used in this study. Only some characteristics, listed in paragraph 2.2.2, need to be known to determine the behaviour of the SFRC. The evolution of single parameters throughout experimental tests can be observed to obtain correlations between the behaviour of SFRC and the AE signals. However, more advanced techniques frequently used in literature are explained in the next paragraphs.

Localisation

The principle of localisation relies on the difference in arrival time between different sensors, for a single signal. The sensor where a hit is detected first, is most likely closer to the source of the wave. When the location of the sensors is known (s), the onset time of each sensor (t_1 and t_2), and the travel speed of the waves inside the material (v), a simple method can determine the location of the crack. Figure 2.2.4 illustrates the method in a 1D situation, where the grey star indicates the source of the wave [33].

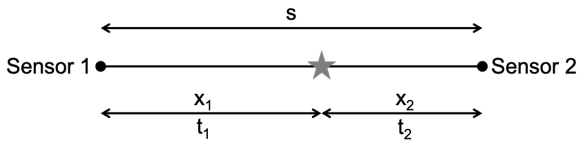

Figure 2.14: Schematic demonstration of the localisation technique in 1D, adapted from [33].

The unknowns are the source time (t_0) and the source location (x_1 and x_2). Following equations express the relation between all parameters [33]:

$$v(t_1 - t_0) = x_2 \tag{2.13}$$

$$v(t_2 - t_0) = x_1 \tag{2.14}$$

$$s = x_1 + x_2 \tag{2.15}$$

This simple 1D example can be extended to 2D and even 3D situations, depending on the amount of equations available. Equations can be added when more AE sensors are available. Therefore, the amount of sensors needed is always one more than the dimensions in which the localisation is desired. More sensors can be added to improve the accuracy [33].

Because concrete is a heterogeneous material, the travel speed of the waves can slightly differ throughout the material. Additionally, noise can also influence the localisation of the source. Therefore, the localisation cannot be determined exactly, but there is an uncertainty on the results [33].

Calm ratio - load ratio

The next analysis can be used during cyclic loading. If a specimen is loaded, unloaded, and reloaded again, the *Kaiser effect* can be observed. This effect indicates the fact that crack propagation mainly occurs after the specimen has reached stresses which are higher than the maximum stresses observed in its history. Accordingly, AE activity is only received when the maximum load is exceeded. This effect can be used to determine the maximum load the test specimen has ever endured [51]. However, in reality some AE activity can be detected even before reaching the maximum load. The ratio between these two loads is called the *Felicity ratio*:

$$\text{Felicity ratio} = \frac{P_{AE}}{P_{max}} \tag{2.16}$$

Theoretically, this value is higher than 1 when the specimen is not yet damaged. AE activity will be generated when the previous load is exceeded. However, when the specimen is damaged, the ratio becomes smaller than one and AE activity occurs for lower loads [33]. Therefore, this ratio can indicate the degree of damage of the specimen.

To display the Kaiser effect, an analysis of the *calm ratio* and *load ratio* is suggested [51]. The load ratio is equal to the Felicity ratio, defined in Equation 2.16. The calm ratio depends on the mode of failure inside the specimen. Three different modes of failure are considered: tensile fracture (mode I), shear fracture (mode II) and mixed-mode (see Figure 2.15). During flexural loading of a specimen, the mode changes from mode I in the beginning of the test to mode II towards the end [2, 33]. In mode I, crack openings are generated and little AE activity is measured during unloading. In mode II, the friction inside a crack results in much more AE activity. Lots of AE activity during unloading therefore corresponds with shear fracture [33]. However, mode II cracks are highly unlikely when SFRC is tested during a direct tensile test. Therefore, mixed-mode cracks are introduced, which are in between

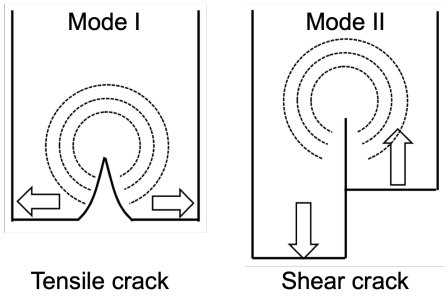

Figure 2.15: Illustration of the tensile and shear mode, taken from [41].

tensile and shear failure modes. During tensile testing, these cracks can occur due to the fibre and concrete interaction.

The ratio between the AE activity during unloading and the AE activity during the whole cycle, is the *calm ratio* [33, 51]. A high calm ratio means that mode II (or mixed-mode) failure is already happening, and heavy damage is expected. A combination of both the calm ratio and load ratio is indicated in Figure 2.16. Most damage is expected for high calm ratios and low load ratios.

AF/RA analysis

Similar to the previous analysis, an *AF/RA analysis* can show the mode of damage for monotonic and cyclic loading through two characteristics, defined in Section 2.2.2 [2]:

- Average frequency (AF) = Count/Duration
- Rise angle (RA) = Rise time/Amplitude

Usually, mode II failure results in AE signals with a large rise time and small frequency. This result may be explained by the fact that for shear cracks, most of the energy is transmitted into shear waves. These waves are slow, with large amplitudes and low frequencies. However, longitudinal waves are sent from the same crack as well. The latter waves arrive much faster at the sensor than the shear waves due to the increased speed. This results in a large time difference between the onset of the signal and the maximal amplitude. Therefore, the rise time is relatively large for mode II failure.

The contrary can be said of mode I failure signals, where the waves are mostly longitudinal [3]. The increased travel speed results in a shorter rise time. This means that a high AF is typical for mode I failure, and a high RA value is typical for mode II failure. This is shown in Figure 2.17, where tensile and shear cracks are divided based on their AF and RA values. However, an exact criterion for the crack modes does not exist yet, this analysis can only be made to achieve a general idea [49]. An approximation of the slope of the diagonal in Figure 2.17 can be made by dividing the maximal AF and RA value [47].

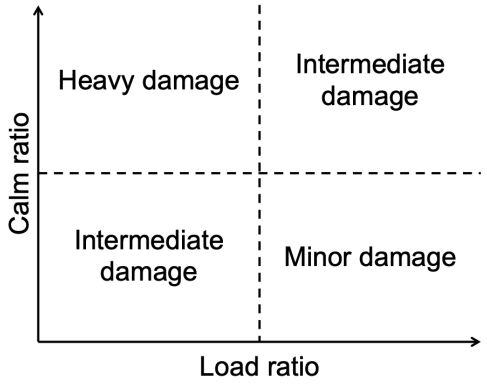

Figure 2.16: Damage quantification with a combination of Calm and Load ratio, adapted from [33].

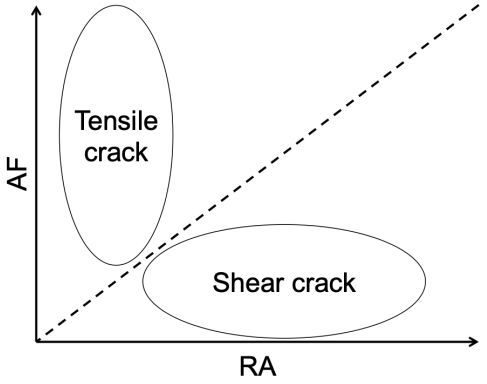

Figure 2.17: Crack type classification with a combination of average frequency and RA values, adapted from [33].

2.3 Conclusion

Steel fibre reinforced concrete and acoustic emission analysis are studied to obtain a clear understanding of the background of this thesis and to be able to formulate research questions. A brief conclusion is written in the next paragraphs.

The literature study starts with a discussion about steel fibre reinforced concrete (SFRC). The fibres cause the concrete to increase its tensile strength after reaching the tensile peak-stress and initiating a macro-crack. The ductility increases because energy can be absorbed by the fibres. In current research, three tests are executed to describe this improved mechanical behaviour. The first one is a pull-out test, where the fibres are pulled out individually to observe the fibre-concrete interaction. Next, a direct tensile test can measure the tensile behaviour, but encounters some technical difficulties. Lastly, a bending test can be carried out to obtain the flexural bending strength. This final test is described in the *fib* Model Code 2010. Due to the lack of building codes regarding SFRC, the MC2010 is one of the few general guidelines for designing SFRC.

An important characteristic of SFRC is the improved fatigue behaviour under cyclic loading. Adding the fibres can enhance the fatigue behaviour of the concrete, and possibly results in a fatigue limit. However, no consensus among researchers has yet been formed about its existence. To predict the lifetime of a structure, Whöler curves can be used, describing the relation between the stress ratio and number of cycles needed before failure. Because of the large amount of data required, another method is proposed in this chapter as well to estimate the damage during cyclic loading. This damage of the structure can be described as the loss of stiffness inside the material and therefore describes the fatigue behaviour.

Next to SFRC, acoustic emission is a second important subject of this research. This non-destructive technique is used to continuously measure the damage evolution in a structure. The formation of cracks is accompanied by elastic waves which are

captured by sensors on the surface of the specimen. The electric signals generated by the sensors are amplified and filtered and are characterised by some parameters which can be analysed to obtain further results.

Several analysing techniques can be executed to gain more information on the failure process inside the material. A localisation technique relates the arrival times at different sensors to the source of the crack. The calm ratio and load ratio show the severity of the damage inside a specimen. This method is specifically designed for cyclic loading and utilisesx the Kaiser effect. The AF/RA analysis shows the mode of failure in a component. Shear cracks and tensile cracks are distinguished by the difference in average frequency and rise time of the signals.

Chapter 3

Experimental research and results

The following chapter contains all experiments executed prior to and during the research of this thesis, needed to correctly interpret the final results. Section 3.1 describes all performed tests, and the different compositions of the SFRC. Next, the three-point bending test is discussed in Section 3.2. The test setup as well as the main results, which are needed further in this research, are presented. Finally the test setup and obtained results of the direct tensile tests are reviewed in Section 3.3. Afterwards all conclusions are summarised in Section 3.4.

3.1 Description of the test specimens

3.1.1 Overview of the experimental tests

In a previous study [17, 19], SFRC beams ($150\,mm \times 150\,mm \times 660\,mm$) were cast and tested in 3PBTs to obtain the flexural response. These beams developed a macro-crack in the middle of the beam, at the notched section. From the remaining halves of the beams, two cores were drilled ($\phi 100\,mm \times 300\,mm$) and notched to execute direct tensile tests. The latter are performed within the scope of this thesis. However, the results of the 3PBTs are included as well, as they are needed to predict and verify the cyclic behaviour of SFRC.

A total of 55 tests are performed (Table 3.1), divided into four test groups with different properties (Table 3.2). Three monotonic 3PBTs and three cyclic 3PBTs are executed for each group, a total of 24 3PBTs. Next, four monotonic DTTs are performed for each group as well. The final 15 tests are the cyclic DTTs. Here, the number of tests per group is based on the amount of fibres in the cross-section.

3.1.2 Fibres

To obtain a clear understanding of the behaviour of steel fibres in concrete, two different quantities and two different types of fibres are used. Table 3.2 shows the

Table 3.1: Total number of tests.

	Monotonic	Cyclic	Total
3PBT	12	12	24
DTT	16	15	31

different percentages of fibres with respect to the total volume of the specimens and their amount of end-hooks (Figure 3.1). The nomenclature indicated in Table 3.2 is based on the fibre type (first two characters) and the fibre volume (last two characters). Other properties of the fibres are indicated in Table 3.3, as provided by the manufacturer. The length of both fibres is equal, while the aspect ratio (length/diameter) differs. The tensile stress is the highest for the 5D fibre, but the modulus of elasticity is the same. Finally, the strain at ultimate strength differs significantly for both fibres. The 5D fibres are designed to offer "perfect anchorage". Therefore the fibres will withstand pull-out from the concrete matrix, and provide ductile deformation, as indicated by the high strain at ultimate strength [10].

Table 3.2: Fibre volume fractions in all test specimens.

	20 [kg/m^3] = 0.25 V%	**40 [kg/m^3] = 0.50 V%**
3D	3D20	3D40
5D	5D20	5D40

Table 3.3: Properties of the steel fibres [8, 9].

Fibre type	**Length [mm]**	**Diameter [mm]**	**Tensile strength [MPa]**	**Modulus of elasticity [GPa]**	**Strain at ultimate strength**
3D-80/60-BG	60	0.75	1225	200	0.8%
5D-65/60-BG	60	0.92	2300	200	6.0%

Figure 3.1: Illustration of 3D fibres (left) and 5D fibres (right), taken from [8, 9].

3.1.3 Concrete

All specimens are cast at KU Leuven and stored with a humidity of 90% at 20°C. The composition of the concrete is shown in Table 3.4 and equal for all test specimens. Only the fibre volume fraction and end-hooks differ for every test group, to be able to accurately measure the effect of the fibres themselves and experience no influence of the concrete.

Researchers showed that for a limited amount of fibres, the behaviour of SFRC in compression only depends on the concrete composition, and not on the fibres [29, 34].

The compressive strength is determined according to EN 12390-3 [28] on 28 days. For every test group indicated in Table 3.2, three cubes ($150\,mm \times 150\,mm \times 150\,mm$) are tested. Since each test specimen has the same mixture, the average value is calculated over all twelve cubes, resulting in a mean cube compressive strength of $f_{cm,cube} = 59\,MPa$ with a standard deviation of $3.5\,MPa$. This results in a mean cylinder compressive strength of [66]:

$$f_{cm} = 0.79 \cdot f_{cm,cube} = 46.61\,MPa \tag{3.1}$$

Therefore, the composition can be classified in class C40/50. Accordingly, the secant modulus of elasticity equals $E_{cm} = 35\,GPa$ [36].

Table 3.4: Concrete composition.

Material	**[kg/m^3]**
CEM I 52.5 R HES	350
Sand 0/4	835
Gravel 4/14	1099
Water	175
Superplasticizer Glenium 51	1 (=0.3 %)

3.2 Three-point bending test

3.2.1 Test setup

The bending test, as explained in the EN14651 [26] and in Section 2.1.2, has been executed in a previous study [17, 19]. The test setup (Figure 3.2 and 3.3) is therefore already determined [17] and the results are known. The 3PBTs are executed on notched beams ($150\,mm \times 150\,mm \times 660\,mm$), with a notch of $25\,mm$ deep. For the AE measurements, four sensors are placed in a vertical plane trough the middle of the specimen. Because they are situated in one plane, localisation of the source can only take place in 2D. However, the localisation is not as important as the signals themselves during this research. With four sensors, it is more certain that a signal can be recorded, even though there might be a crack preventing a signal to reach a certain sensor.

The executed 3PBT is CMOD controlled and stopped at a CMOD of $4\,mm$. With the bottom of the beam equal to $y = 0\,mm$, the CMOD is measured at $-20\,mm$ with an LVDT with a gauge length of $40\,mm$. The test setup also includes 5 additional LVDTs, positioned at heights of 35, 60, 90, 120 and $145\,mm$. They measure the strains in the middle of the specimen, where the beam is notched and the crack will occur. The strains are determined with a gauge length of $40\,mm$.

The same test setup is used during the cyclic tests, although the specimen is unloaded at CMODs of 0.1, 0.2, 0.3, 0.4, 0.5, 1.0, 1.5, 2.0, 2.5, 3.0, 3.5 and $4.0\,mm$. Unloading is stopped at around $0.7kN$, after which reloading starts.

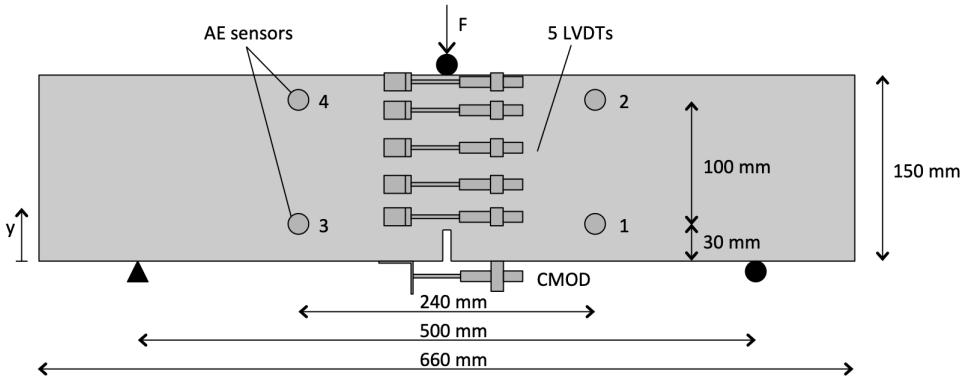

Figure 3.2: Test setup for the three-point bending test.

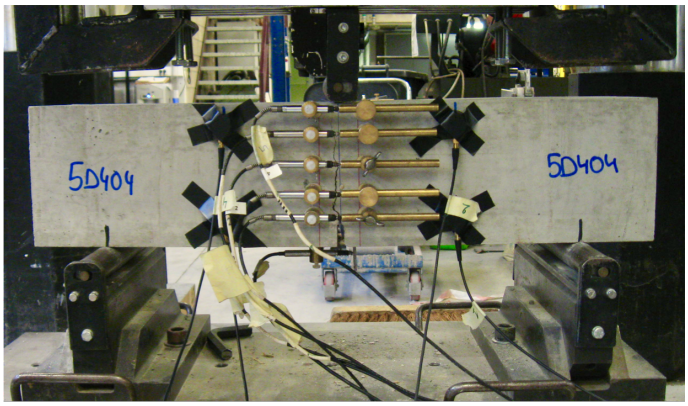

Figure 3.3: Photo of the 3PBT, taken by M. De Smedt.

3.2.2 Results and discussion

Monotonic 3PBTs

The stresses are shown as a function of the CMOD in Figure 3.4. For each fibre volume fraction, three tests are executed. The graphs show the mean values for each fibre type and content, together with the results of the individual tests. The CMOD is calculated according to EN14651 [26] and equals $0.882 \cdot CMOD_y$ (Equation 2.2).

The LOP is calculated (Equation 2.3) to determine the flexural tensile strength for each test group. Next, the classification of every test group can be assessed, using the residual tensile strengths f_{R1}, f_{R2}, f_{R3} and f_{R3}. Equation 2.4 calculates these values.

The characteristic values of the residual strengths are then determined by calculating the 5% characteristic value. Therefore, 3PBTs executed with the same material compositions as used during this research, have a 95% probability to reach higher residual strengths than the characteristic values. The characteristic strengths match f_m better when the certainty is higher, represented by the amount of tests which are

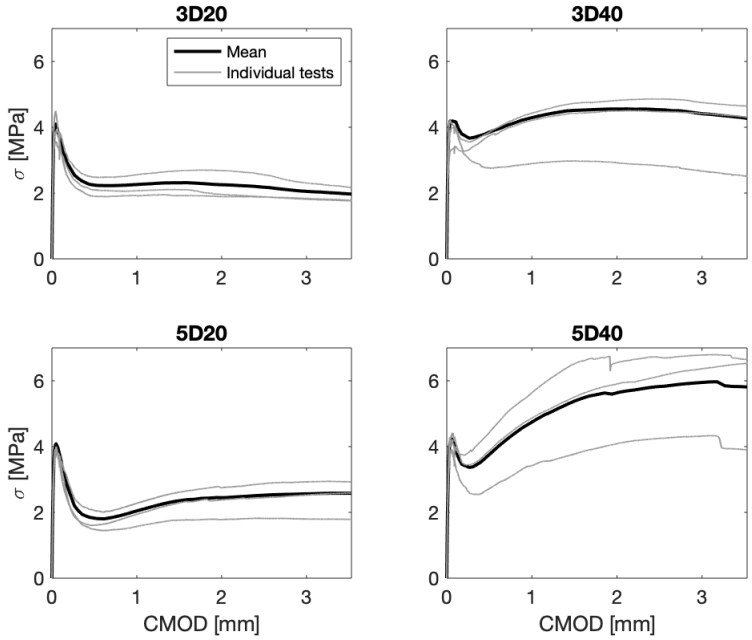

Figure 3.4: Results of the monotonic three-point bending test.

executed. This certainty is taken into account with k_n, determined in table D1 of EN 1990 [25].

There are two different approaches to calculate the characteristic value. The first approach is by assuming a normal distribution. However, using this method can result in negative values of the residual tensile strengths. Therefore, the second option is chosen, where a log-normal distribution is assumed. The characteristic value is obtained by applying following equations:

$$f_{k,ln} = \exp\left(f_{m,ln} - k_n \cdot s_{ln}\right) \tag{3.2}$$

$$f_{m,ln} = \frac{1}{n} \cdot \sum_{i=1}^{n} \ln\left(f_i\right) \tag{3.3}$$

$$s_{ln} = \sqrt{\frac{1}{n-1} \cdot \sum_{i=1}^{n} (\ln\left(f_i\right) - f_{m,ln})^2} \tag{3.4}$$

with

$f_{k,ln}$ The characteristic strength [MPa]
$f_{m,ln}$ The mean strength [MPa]
k_n Parameter taking into account the amount of tests = 3.37 for 3 test specimens
s_{ln} The standard deviation [MPa]
n The amount of test specimens

The classification of all four test groups is indicated in Table 3.5, together with the characteristic strengths and standard deviations. A higher fibre volume fraction increases the classification, as well as the usage of 5D fibres instead of 3D fibres.

Table 3.5: Residual tensile strengths and their characteristic value (k), in MPa.

	3D20	**3D40**	**5D20**	**5D40**
f_L	3.99	3.83	3.88	4.12
s_L	0.12	0.12	0.03	0.05
f_{Lk}	2.69	2.50	3.55	3.45
f_{R1}	2.16	3.45	1.72	3.67
s_{R1}	0.13	0.18	0.17	0.25
f_{R1k}	1.36	1.84	0.96	1.54
f_{R2}	2.23	4.04	2.22	5.72
s_{R2}	0.17	0.25	0.20	0.28
f_{R2k}	1.24	1.70	1.12	2.00
f_{R3}	2.11	4.05	2.38	5.70
s_{R3}	0.17	0.20	0.23	0.24
f_{R3k}	1.16	1.48	1.07	2.47
f_{R4}	1.91	3.83	2.43	5.69
s_{R4}	0.12	0.28	0.26	0.30
f_{R4k}	1.28	1.21	1.01	2.00
Classification	**1b**	**1.5b**	**1d**	**1.5e**

The first observation of the curves in Figure 3.4 is that, as stated before, the fibres have almost no influence on the pre-peak behaviour. The peak force is similar for every composition (f_L in Table 3.5). However, the post-peak behaviour can change significantly depending on the fibres. The compositions 3D20 and 5D20 show a softening behaviour because the force decreases right after the peak. Hardening is observed for the higher dosages of fibres, where the post-peak strength increases. More energy can be absorbed by the higher amount of fibres bridging the crack. Comparing the fibre types shows a smaller difference. The energy needed for the pull-out process is higher for the fibres of type 5D, but the influence on the results is not as significant as the fibre volume. Further, it can be noticed that the scatter in results is clearly higher for the higher fibre volume fraction. The higher the amount of fibres, the more the fibres will deviate from their nominal value. This effect is discussed later on.

In Chapter 4, a model is composed to predict the cyclic behaviour of SFRC, assuming a linear deformation profile. Therefore, the Euler-Bernoulli beam hypothesis is checked. The LVDTs measure the deformation of the beam over the cracked section and are therefore able to reconstruct the total deformation profile. This data is approached by a linear fit in Figure 3.5.

The linearity of all deformation profiles is determined using the coefficient of determination (r^2):

$$r^2 = 1 - \frac{\sum_{i=1}^{n}(x_i - \hat{x}_i)^2}{\sum_{i=1}^{n}(x_i - \bar{x})^2} \tag{3.5}$$

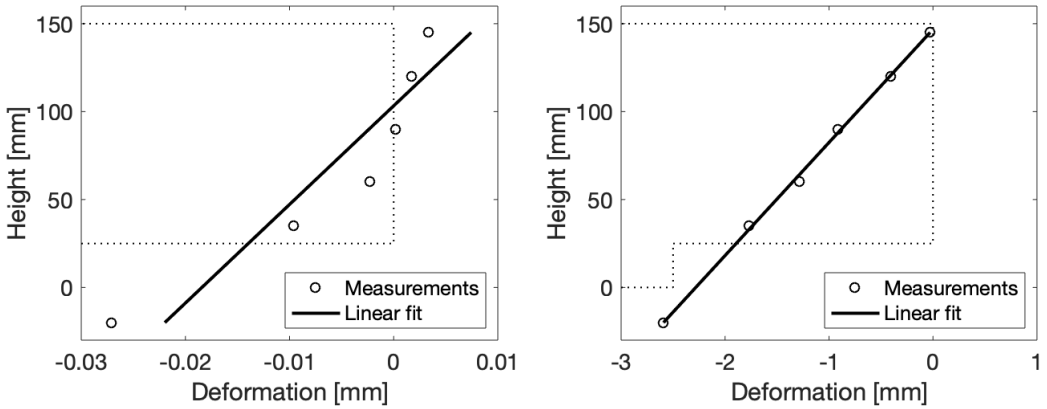

(a) $CMOD = 0.024\,mm$. (b) $CMOD = 2.287\,mm$.

Figure 3.5: Linear deformation profiles for 3D20 M1, at different CMODs.

In this equation, x_i are the measured deformations of the beam, $\hat{x}_i$ are the values calculated according to the linear regression, and $\bar{x}$ is the mean deformation. Two conclusions can be made after plotting the results (Figure 3.6). First, r^2 is low for smaller CMODs, which can be explained mathematically. For low CMODs, almost no deformations occur. Therefore, x_i is close to the mean value $\bar{x}$ and the denominator of Equation 3.5 tends to go to zero, increasing the second term of the equation. Secondly, a decrease in r^2 is noticed for CMODs close to the peak strength. When a macro-crack occurs, the deformations in the tensile zone of the beam will suddenly increase, creating a deformation profile which is bilinear, shown in Figure 3.5a. However, both effects are neglected in the further research as they do not have a great influence on the results. The mean results of all test groups show that the deformation profile is mainly linear, as r^2 almost equals 1 (Table 3.6). Therefore, the Euler-Bernoulli hypothesis can be used further in this thesis when analysing the monotonic bending behaviour.

Table 3.6: Mean coefficient of determination for linear deformation profiles during monotonic 3PBTs.

	3D20	**3D40**	**5D20**	**5D40**
r^2	0.994	0.989	0.992	0.994

Cyclic 3PBTs

The cyclic 3PBTs are again CMOD controlled. For the cyclic tests, the specimens are unloaded at certain CMODs. These CMODs are equal to: 0.1, 0.2, 0.3, 0.4, 0.5, 1.0, 1.5, 2.0, 2.5, 3.0, 3.5 and 4.0 mm. After unloading, the specimen is reloaded, resulting in the hysteresis behaviour which can be seen in the Figure 3.7.

All σ-$CMOD$ curves are shown in Figure 3.7. For every test group, three individual specimens are tested. The mean results of all tests are indicated on the figure as

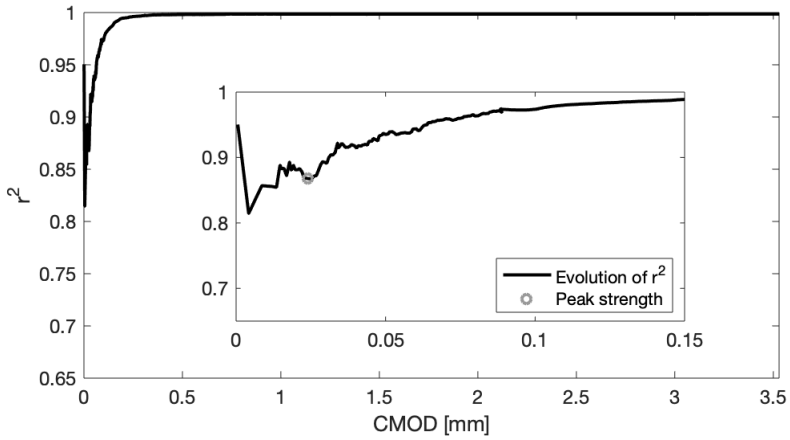

Figure 3.6: Evolution of the coefficient of determination for the first monotonic test of group 3D20, and a detailed view.

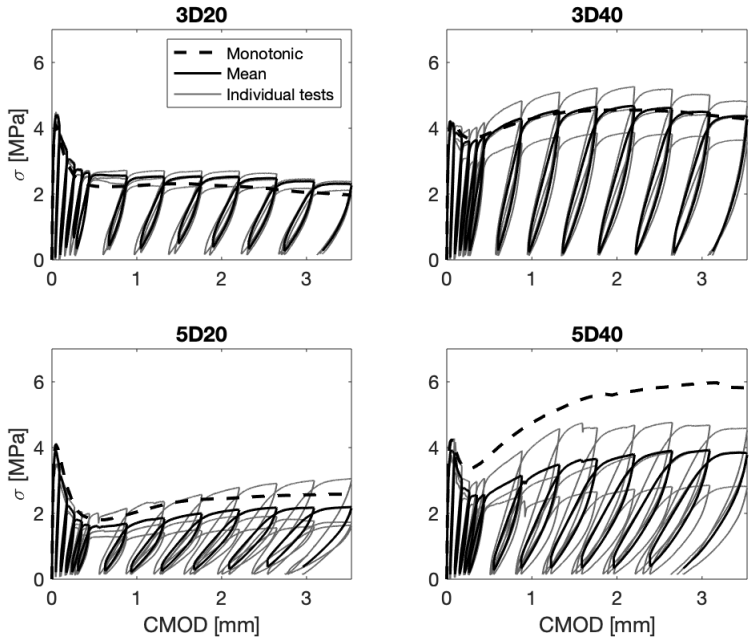

Figure 3.7: Results of the cyclic three-point bending test.

well. Finally, the striped curve shows the mean results of the monotonic response. Researchers concluded that the monotonic curves can be used as the envelope curves of the cyclic behaviour [41, 53], which is confirmed in this study. These envelope curves are defined as the boundaries of the cyclic curves, they both follow the same trend. However, test group 5D40 shows a greater difference between the monotonic and cyclic behaviour. This can be attributed to experimental scatter.

The deformation profiles are again checked with the LVDT measurements, to find out if the Euler-Bernoulli hypothesis is still valid. The coefficient of determination is calculated for all test groups with Equation 3.5. However, during two tests of the 5D40 test group, one of the LVDTs malfunctioned. Therefore, the r^2 is calculated with the results of five LVDTs. The same conclusion can be made as for the monotonic 3PBTs, due to the high r^2 values the deformation profiles are linear.

Table 3.7: Mean coefficient of determination for linear deformation profiles during cyclic 3PBTs.

	3D20	**3D40**	**5D20**	**5D40**
r^2	0.995	0.996	0.996	0.990

Finally, the damage is calculated for every unloading cycle with Equation 2.11. Figure 3.8 indicates the unloading and reloading stiffness (K_i) for one cycle. The unloading curve is defined between the point of unloading and the point when the lowest stress is reached, the reloading curve starts at the end of unloading and reaches to the point where the maximum CMOD is surpassed. The stiffness is equal to the steepness of these curves, which is higher for the unloading curves. The damage curves of Figure 3.9 therefore show more damage when reloading.

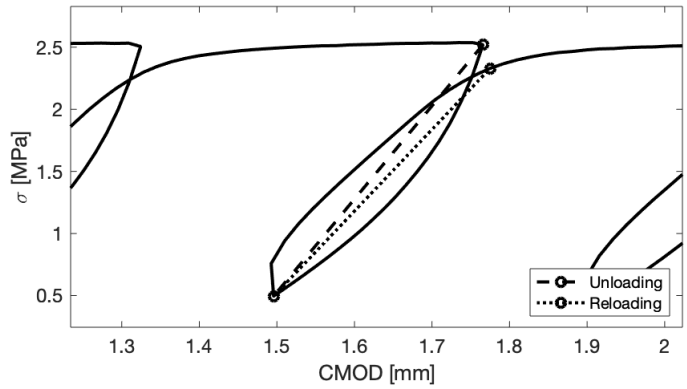

Figure 3.8: Indication of the unloading and reloading stiffness.

The damage curves clearly show the evolution of the damage when CMOD increases. The higher the CMOD, the higher the damage. However, after reaching the peak strength, the increase of D becomes less noticeable. The difference between the four test groups is quite small in Figure 3.9, but worth mentioning because of the big influence on the stress profile in the damaged section. When more fibres are added to the mixture, the damage decreases. The increase in resistance against tensile cracking caused by the higher amount of fibres therefore increases the stiffness. 5D fibres increase the damage, caused by the improved tensile strength of the fibres and increased amount of end-hooks. Both characteristics increase matrix cracking.

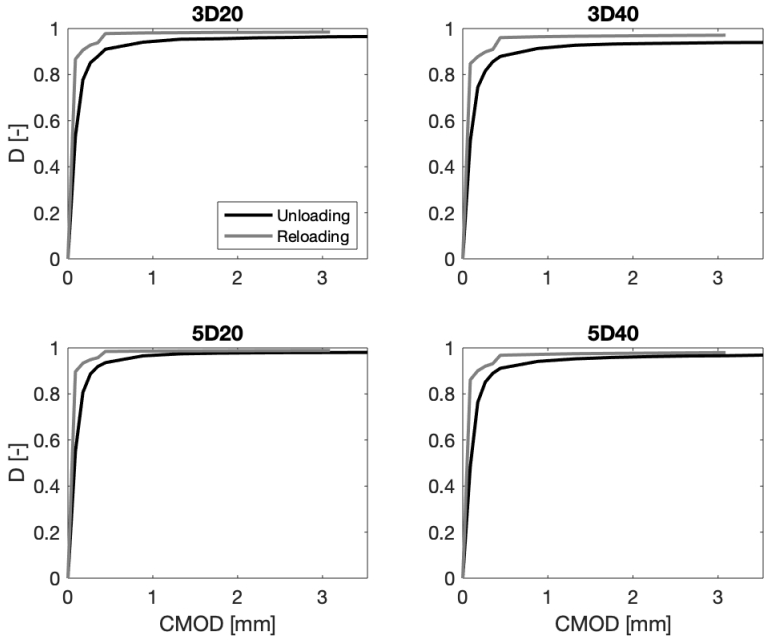

Figure 3.9: Unloading and reloading damage curves for 3PBTs.

3.3 Direct tensile test

3.3.1 Test setup

After the three-point bending test, two cores ($\phi 100\,mm \times 300\,mm$) are taken from the beam to perform a direct tensile test. Their midsection is notched with a $10\,mm$ deep notch. No influence of the failure during the 3PBT is expected because the notched section is located far enough from the failed section in bending [67].

These cylinders are glued to two steel plates with epoxy glue. In order to avoid failure at the glued section, a cylindrical mould is placed around the specimen. The cylinder is then clamped by the testing machine, reaching a small compression force. Afterwards, the specimen is screwed onto the testing machine, until the uniaxial force is nearly zero. The force and stroke are measured by the machine itself. Clip gauges are placed at the notch to measure the crack width. Due to the smaller section, the macro-crack will develop here. A total of three clip gauges, positioned in angles of 120° is sufficient. The overall crack width is calculated taking the average of all clip gauges. Figure 3.10 shows a schematic overview.

The loading scheme is different for both the monotonic and cyclic tests. The monotonic curves are obtained by increasing the stroke by $0.005\,mm/min$ until the stroke reaches $0.1\,mm$. Afterwards, the loading rate is increased to $0.1\,mm/min$, until the loading is stopped at a stroke of $4\,mm$. Next, the cyclic tests contain the same load scheme as the monotonic tests. However, unloading and reloading cycles are included at strokes of 0.1, 0.2, 0.3, 0.4, 0.5, 1.0, 1.5, 2.0, 2.5, 3.0, 3.5 and $4.0\,mm$.

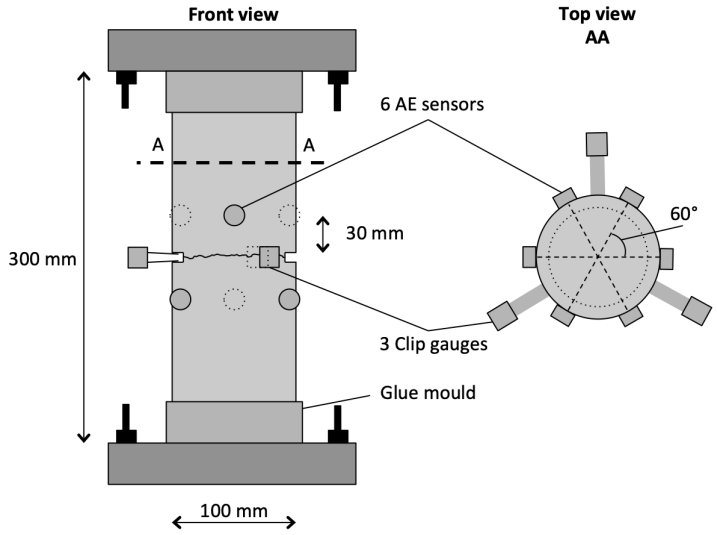

Figure 3.10: Test setup for the direct tensile test.

3.3.2 AE setup

Section 2.1.3 mentions the difficulty of a direct or uniaxial tensile test. Therefore, not many studies are executed performing these tests, especially while performing acoustic emission sensing. Zhah and Li [60] and Xiangqian et al. [69] executed DTTs combined with AE sensing, but both with the main intention of localising the cracks. These studies are not comparable with the results needed for this thesis, since the crack is initiated in the known notched section. Therefore, and a new setup is developed. As mentioned before, the required dimension of the localisation determines the amount and position of the sensors. At first, four sensors were used during the DTTs, which can obtain data in 3D. However, they were positioned in a single plane, to measure in 2D with a higher accuracy. They are placed at a distance of 30 mm above the notch, and attached to the concrete with a vacuum gel and tape (Figure 3.11).

After the placement of all sensors, a calibration is executed in two different ways. First, pencil lead breaks at the location of every AE sensor are carried out. This test indicates whether the location of cracks is captured accurately by the sensors and if all sensors can receive the signals. Then, each sensor individually sends signals, to again confirm that the AE sensors indeed receive signals. As the locations of all sensors are known, the arrival times of these signals give an indication on the speed at which the waves travel through the specimen. Concrete is a heterogeneous material and therefore the travel speed can differ significantly for each test specimen, in every direction. However, during all tests, the wave speed is taken equal to 3700 m/s, obtained from the calibration of the DTTs, combined with the results from the 3PBTs. As the localisation of the cracks is not the main goal of the current study, the influence of this simplification remains limited.

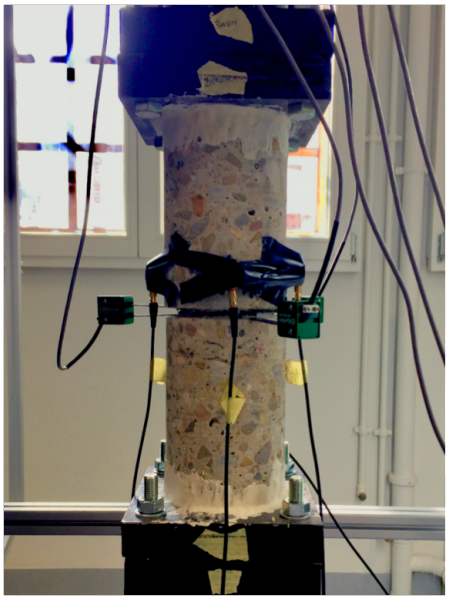

Figure 3.11: Photo of a DTT with 4 AE sensors.

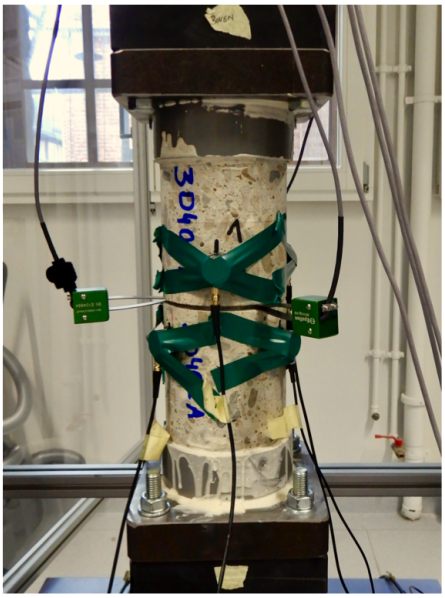

Figure 3.12: Photo of a DTT with 6 AE sensors.

Two negative effects occurred with the previously defined test setup. First of all, the symmetric placement of four sensors in a single plane resulted in a *ringing* effect during calibration. The signal sent from a single sensor reflects on the opposite sensor, creating a malfunction of the AE sensors. If the results of calibration cannot be used, the velocity of the signals in the test specimen can not be determined, creating an error in the localisation. A second important aspect is the blocking of signals due to the crack which is formed in the notched section. To register an event, at least three sensors need to detect the same group of hits. If all sensors are placed at one side of the notch, cracks can disturb the amount of events registered.

Both problems can possibly be solved by using six instead of four sensors. These sensors are placed in two parallel planes, one $30\,mm$ above and one $30\,mm$ below the notch (Figure 3.12). As there is no symmetry anymore, the first problem is solved. The second problem is solved as well, as the sensors are divided over both halves of the specimen. Even when a crack is formed, an event can still be registered. Both setups are tested during the DTTs, but the second one is preferred (Figure 3.10).

The AE sensors are $150\,kHz$ resonance sensors with an operating range of $100 - 450\,kHz$ (Vallen VS150-M). A Vallen AMSY-6 system is used with six-channel ASIP-2/S AE boards. The acquisition system makes use of a pre-amplifier with a $34\,dB$ gain (AEP5), a frequency filter of $50 - 850\,kHz$ and an amplitude threshold of $40\,dB$. A second amplitude filter of $50\,dB$ is added in post-processing and the data is retrieved at a sampling rate of $5\,MHz$. The location uncertainty determined by the pencil lead tests equals $20\,mm$.

3.3.3 Mechanical results and discussion

Stress - crack opening curves

Monotonic DTTs The direct tensile tests are stroke-controlled, the stroke monotonically increases during the test. This stroke is defined as the total displacement of the testing machine, therefore taking into account the elastic and plastic strain of the test specimen, as well as the elastic strain of the machine itself. Because the strain of the testing machine is an unwanted displacement, the stroke will not be used for further analysis of the results, only the crack width is taken into account. This latter value is measured by the three clip gauges in the notched section.

The results of the monotonic DTTs are shown in Figure 3.13. The first observation is that the pre-peak behaviour is poorly captured by the clip gauges. Before a macro-crack initiates, the clip gauges do not register any deformations. A second remark is that the curves show a large difference between all individual tests, for all test groups. This scatter can be explained by the fibres. The amount of fibres in the cracked section is a crucial factor to the post-cracking behaviour of the specimen. The more fibres, the higher the strength of the specimen. However, this amount is impossible to determine on beforehand. After completing the test, the cross-section is investigated to count the number of fibres, and a strong correlation is found between the amount of broken and pulled-out fibres, and the tensile post-cracking behaviour.

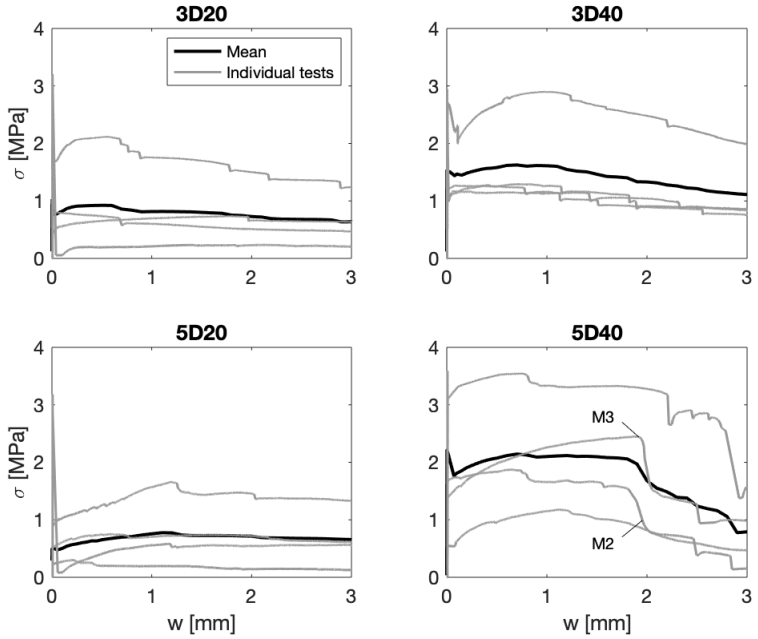

Figure 3.13: Results of the monotonic direct tensile test (original groups).

The nominal amount of fibres (n_f) is estimated by the following formula [24, 38]:

$$n_f = \alpha \cdot V_f \cdot \frac{A_n}{A_f} \tag{3.6}$$

The parameters A_s and A_f are the area of the cross-section and of an individual fibre respectively. V_f is the fibre volume fraction and α is the orientation factor dependant on the randomness of the fibres. A value of $\alpha = 1$ indicates the perfect alignment of the fibres in tensile direction. The formula also captures the fact that the scatter is bigger for the higher amount of fibres. The nominal values shown in Table 3.8 are calculated with $\alpha = 0.5$. Because the boundaries do not affect the orientation of the fibres in the notched section, the theoretical value for fibres in a 3D space is chosen [23].

Table 3.8: Nominal number of fibres in the cross-section.

	3D20	**3D40**	**5D20**	**5D40**
n_f	14.2	28.4	9.9	19.8

After the calculation of these nominal values, new test groups are formed, depending on the number of fibres in the cross-section. The fibres in every cross-section are counted and summarised in Table 3.9. The specimens for which the fibres deviate the most, are shaded. These would fit better in the other test group. Therefore, new test groups are composed in Table 3.10. The groups are now formed with the three specimens fitting the estimated n_f the best. Figure 3.14 illustrates the experimental results when new test groups are specified.

Table 3.9: Amount of fibres in the cross-section of every test specimen for monotonic DTTs.

3D20	14.2	**3D40**	28.4	**5D20**	9.9	**5D40**	19.8
3D20 M1	25	3D40 M1	21	5D20 M1	8	5D40 M1	12
3D20 M2	6	3D40 M2	27	5D20 M2	19	5D40 M2	21
3D20 M3	9	3D40 M3	41	5D20 M3	5	5D40 M3	26
3D20 M4	12	3D40 M4	23	5D20 M4	4	5D40 M4	24

Table 3.10: New test groups for the monotonic DTTs.

3D20	14.2	**3D40**	28.4	**5D20**	9.9	**5D40**	19.8
3D20 M3	9	3D20 M1	25	5D20 M1	8	5D20 M2	19
3D20 M4	12	3D40 M2	27	5D20 M3	5	5D40 M2	21
3D40 M1	21	3D40 M4	23	5D40 M1	12	5D40 M4	24

When studying the curves of Figure 3.14 in more detail, several drops are noticed in the stresses, often followed by a gain in tensile stress. These sudden jumps in the curves indicate a fibre fracture or pull-out in the notched section. The stress suddenly drops and is afterwards redistributed in the section.

A final remark on the σ-w curves of the monotonic DTTs, is the sudden stress drops in test group 5D40. These are larger than the drops discussed in the previous

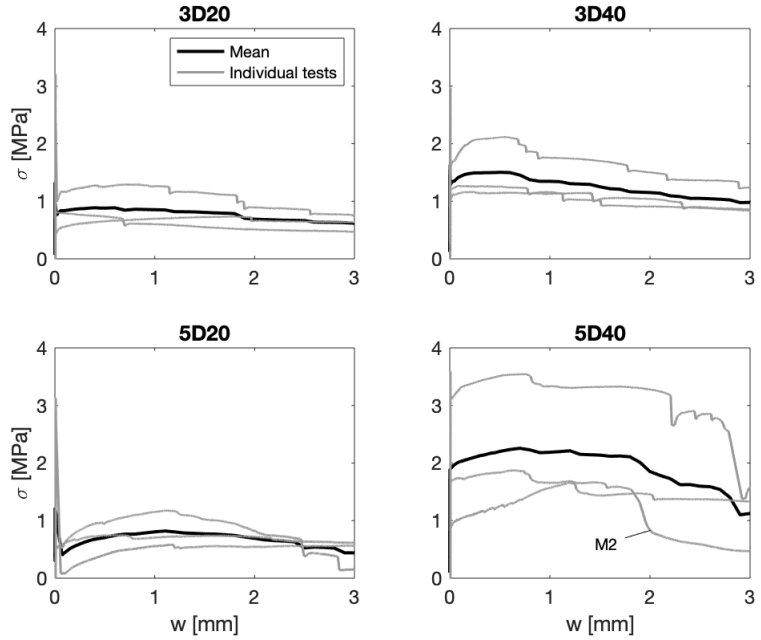

Figure 3.14: Results of the monotonic direct tensile test (new groups).

paragraph, and cannot be attributed to the fibre failures. The decrease in tensile stress can be explained by multiple cracking of the specimen. If less energy is required to initiate a new crack than enlarging the crack in the notched section, multiple cracking occurs. Due to the high resistance of 5D fibres and the high volume fraction in test group 5D40, it only occurred for these specimens, more specifically for 5D40 M2 and 5D40 M3, indicated in Figures 3.13 and 3.14. Therefore, the stress drops due to the formation of a multitude of cracks, and the clip gauges only measure the crack at the notched section. This results in an underestimation of the plastic deformations in the specimen and consequently the σ-w curve suddenly drops.

After analysing the post-peak behaviour of Figure 3.14, also the peak strength can be calculated for all test groups. Because the crack openings at peak strength differ slightly for all test specimens, these values are determined for every test specimen individually. Then, the average value can be calculated for all test groups, resulting in the peak stresses (f_{ctm}) and standard deviations (s) of Table 3.11. The stresses of all test groups are similar, as the fibres do not influence the peak strength of the material. The differences in peak strength are only attributed to experimental scatter. In the last column of the table, the mean of all tested specimens is given.

Table 3.11: Peak stresses for every test group during monotonic DTTs.

	3D20	**3D40**	**5D20**	**5D40**	**Mean**
f_{ctm} [MPa]	2.61	2.16	2.77	2.45	2.50
s [MPa]	0.60	1.47	0.39	0.61	0.82

Cyclic DTTs Figure 3.15 illustrates the stress - crack opening curves for the cyclic direct tensile tests. As the tests are now stroke-controlled, the unloading will occur at certain values of the stroke (0.1, 0.2, 0.3, 0.4, 0.5, 1.0, 1.5, 2.0, 2.5, 3.0, 3.5 and $4.0\,mm$). Since the stroke and crack width do not coincide, no average cyclic response can be calculated for the test groups. However, the mean envelope curve can be determined, as shown in the graphs.

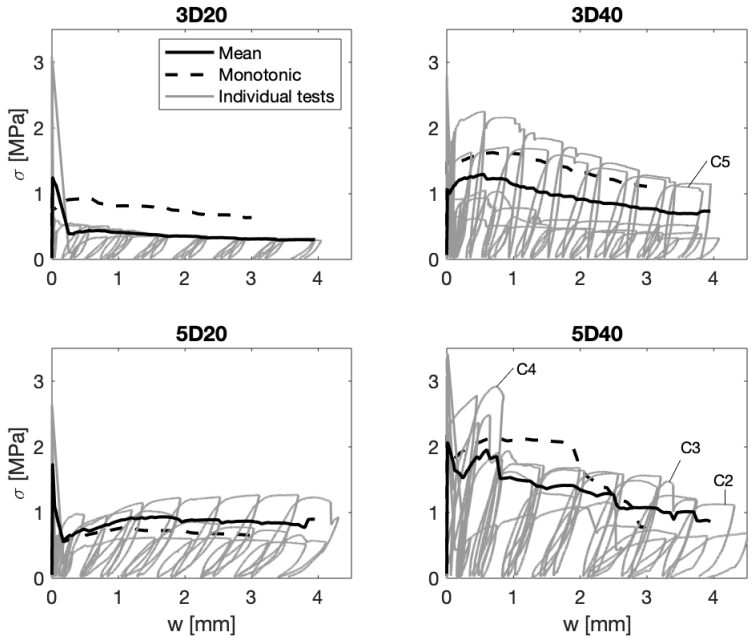

Figure 3.15: Results of the cyclic direct tensile test (original groups).

The results of the cyclic tests show the same problem as the monotonic DTTs. The amount of fibres has a large influence on the output of the tests. The nominal amount of fibres for every test group as well as the counted fibres for each test can be found in Table 3.12. Again, new test groups are determined, which are indicated in Table 3.13. The mean fibre amounts of these new groups are similar to the nominal value, except for test group 5D40. The mean amount of fibres is 28, which is much higher than the nominal amount of 19.8 fibres. Therefore, the residual stresses are expected to be larger than an average 5D40 test specimen. However, this is not observed in the results. Due to the high amount of fibres, the notched section offers too much resistance and therefore multiple cracking occurs. This suddenly lowers the tensile stresses, as observed in Figure 3.15 for test specimen 5D40 C2, C3 and C4.

As only two test specimens of group 3D40 showed amounts of fibres close to the nominal value, only two curves are kept within this group. One of them, 3D40 C5, also experienced multiple cracking. The results for the new groups are shown in Figure 3.16. All future results will be derived with the new test groups, both for the monotonic and cyclic test.

Table 3.12: Amount of fibres in the cross-section of every test specimen for cyclic DTTs.

3D20	14.2
3D20 C1	12
3D20 C2	9
3D20 C3	8

3D40	28.4
3D40 C1	20
3D40 C2	11
3D40 C3	28
3D40 C4	18
3D40 C5	31

5D20	9.9
5D20 C1	10
5D20 C2	10
5D20 C3	5

5D40	19.8
5D40 C1	10
5D40 C2	32
5D40 C3	25
5D40 C4	27

Table 3.13: New test groups for the cyclic DTTs.

3D20	14.2
3D20 C1	12
3D40 C2	11
3D40 C4	18

3D40	28.4
3D40 C3	28
3D40 C5	31

5D20	9.9
5D20 C1	10
5D20 C2	10
5D40 C1	10

5D40	19.8
5D40 C2	32
5D40 C3	25
5D40 C4	27

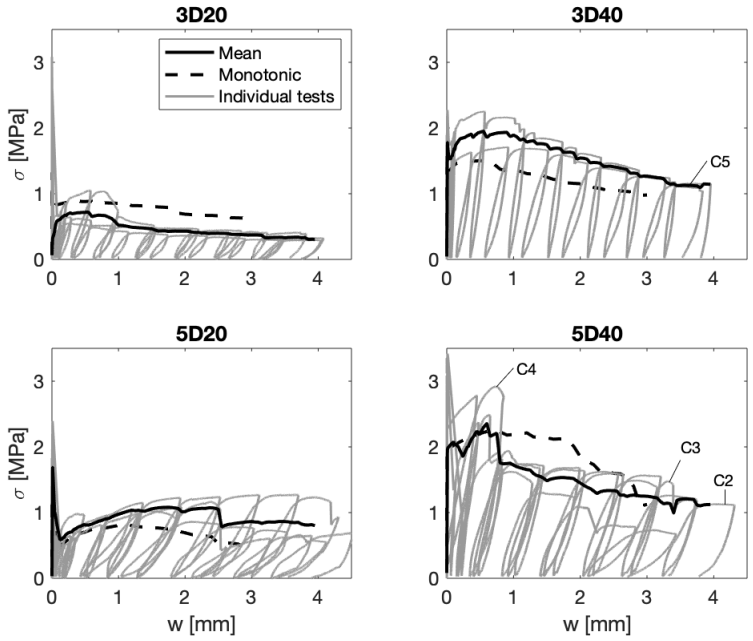

Figure 3.16: Results of the cyclic direct tensile test (new groups).

The graphs of Figure 3.16 show the similarity between the monotonic DTTs and cyclic DTTs. Therefore, it can be said that the monotonic curves are the envelope curves of the cyclic curves. The same conclusion was made for the 3PBTs. The biggest differences between the mean cyclic curve and the monotonic curve can be attributed to the difference in fibres. The mean amount of fibres in the cross-section for all test groups is shown in Table 3.14. Because the fibre amount during the cyclic tests of 3D40 is larger than for the monotonic tests, the cyclic post-peak behaviour shows larger tensile strengths. The same argumentation can be used for the 5D20

test group. However, multiple cracking occurs for test specimens 5D40 C2, C3 and C4, as well as for 3D40 C5 (indicated in Figure 3.15 and 3.16). This phenomenon is mainly visible for the 5D40 test group, which again shows large stress drops during cyclic loading. Therefore the monotonic curve deviates most for test group 5D40.

Table 3.14: Mean amount of fibres in the cross-sections for all new groups.

	3D20	**3D40**	**5D20**	**5D40**
Nominal	14.2	28.4	9.9	19.8
Monotonic	14	25	8.3	21.3
Cyclic	13.7	29.5	10	28

Similar to the monotonic tensile tests, again the mean peak stresses during the DTTs are determined. Table 3.15 contains the mean tensile stress and standard deviation for all test groups, as well as the overall average. The total peak strength is close to the value obtained during monotonic loading, in Table 3.15. Cyclic loading of the specimen therefore does not influence the tensile strength.

Table 3.15: Peak stresses for every test group during cyclic DTTs.

	3D20	**3D40**	**5D20**	**5D40**	**Mean**
f_{ctm} [MPa]	2.97	2.45	2.22	2.97	2.65
s [MPa]	0.15	0.37	0.40	0.50	0.47

Plastic deformation

The damage of SFRC is related to the irreversible plastic deformation (w_{pl}), equal to the deformation at the end of unloading. This crack opening remains even when the specimen is not loaded. When the specimen has not reached its peak strength yet, w_{pl} equals zero as the cross-section has only deformed elastically. After reaching the peak strength, a macro-crack is formed and plastic deformation occurs. Previous research [1, 41] states that the effect of fibres is insignificant to the plastic deformation and can therefore be determined by the deformation at unloading only (w_{unl}).

The plastic deformations for all tests are shown in Figure 3.17, as it is independent of the fibres. As expected by references [1, 41], the results reveal a linear relation between the plastic deformation and unloading deformation after reaching the peak strength. This linear fit is nearly independent on the fibres.

A linear function is composed to predict the plastic deformation of SFRC, and shown in the figure. Its coefficient of determination is $r^2 = 0.975$. The fit is calculated using only values of crack openings greater than the crack opening at peak stress (w_{tu}). Further, when w is equal to or smaller than the crack opening at peak stress, w_pl equals 0, because no plastic deformation occurs before cracking.

$$w_{pl} = \begin{cases} 0.8569 \cdot (w_{unl} - w_{tu}) & \text{if } w_{unl} > w_{tu} \\ 0 & \text{if } w_{unl} \leqslant w_{tu} \end{cases} \tag{3.7}$$

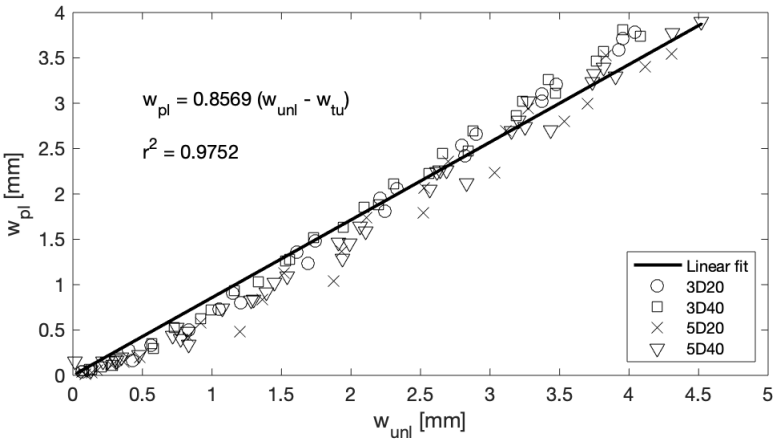

Figure 3.17: The plastic deformation w_{pl} for every test group.

The crack opening at peak stress w_{tu} is not yet defined because the clip gauges only measure the post-peak behaviour. When this relation is used in further calculations, w_{tu} depends on the pre-peak elastic deformation of the concrete matrix.

Additionally, it should be noted that this linear fit is calculated taking into account the future application of the relation. The crack widths shown in the figure are not exactly equal to the measured crack widths in the DTT. An elastic deformation is added to the measured values, as this will be needed for the future model. According to Hooke's law, the elastic strain equals:

$$\varepsilon = \sigma / E_{ci} \tag{3.8}$$

The elastic stiffness E_{ci} is calculated according to the Model Code [29], where f_{cm} is the compressive strength, calculated in Section 3.1.3.

$$E_{ci} = 21.5 \cdot 10^3 \cdot \left(\frac{f_{cm}}{10}\right)^{1/3} = 35.91\, GPa \tag{3.9}$$

However, the elastic strain needs to be related to a certain crack width. This is executed in the Model Code as well. A simple relation between ε and w makes the transition possible [29].

$$\varepsilon = w / l_{cs} \tag{3.10}$$

The parameter l_{cs} is the characteristic length of the structural element, equal to the height of the cracked section for sections without traditional reinforcement and only one crack [29]. This value relates the localised crack width to a smeared strain value [67]. In the model which is developed further in this thesis, 3PBTs are evaluated making use of Equation 3.7. Therefore, the crack widths are transformed to the needs of this model, and the characteristic length equals 125 mm. However, the influence of the characteristic length on Equation 3.7 is limited.

Elastic stiffness

The individual and mean damage functions for all test groups, derived from the experimental data, are shown in Figure 3.18. To obtain the damage curves, the crack width is deformed, taking into account Equations 3.8, 3.9 and 3.10 as explained before. During the elastic phase, the damage equals $D = 0$. After cracking occurs, D increases according to the experimental results. To obtain an average damage curve, the mean evolution of stiffness is determined over all test specimens in the same test group. Figure 3.18 shows this mean curve as well, for damages higher than 0.95.

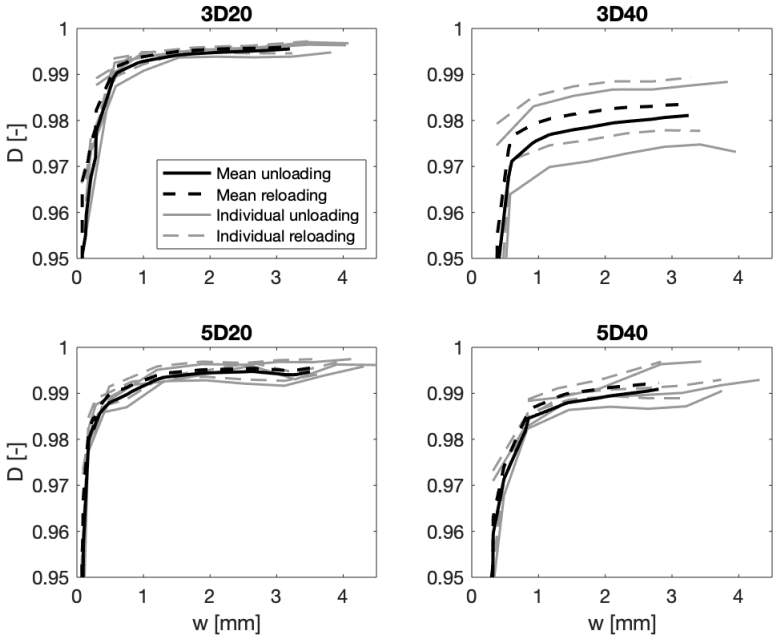

Figure 3.18: Detail of the experimental unloading and reloading damage functions for DTTs.

The monotonic direct tensile curves predict the envelope curves of the cyclic tests well, as concluded before from the experimental results. Therefore, when the envelope curves are known, as well as the linear relation between the plastic deformation and deformation at unloading (Figure 3.17), the plastic deformation and elastic stiffness can be computed. This is illustrated in Figure 2.11. Further, the elastic stiffness can be related to the accumulated damage of the specimen through Equation 2.11. The initial stiffness E_0 is calculated in Equation 3.9. However, as the stiffness during the experiments is expressed in MPa/mm, a characteristic length is needed. This length is again equal to 125 mm, determined in the previous paragraph.

Figure 3.19 illustrates the difference between the experimentally obtained unloading and reloading damages, as well as the damage calculated with the experimentally obtained monotonic curves and linear fit of the plastic deformation. The damage

curves obtained from the cyclic DTTs are not as smooth, because unloading only occurs at discrete points in time. But generally, the curves show good agreements. The damage decreases when the fibre content increases, for both methods. The higher fibre volume offers more resistance against crack formation, as the stress inside the cross-section is better redistributed. Using the 5D fibres shows an increase in damage, caused by the higher fibre strength and double end-hook. This is clearly visible in the experimental curves of Figure 3.18. However, using the plastic deformation results in lower damages for test group 5D40. This is caused by the high post-peak behaviour and the fact that no division is made between 3D and 5D fibres in Equation 3.7.

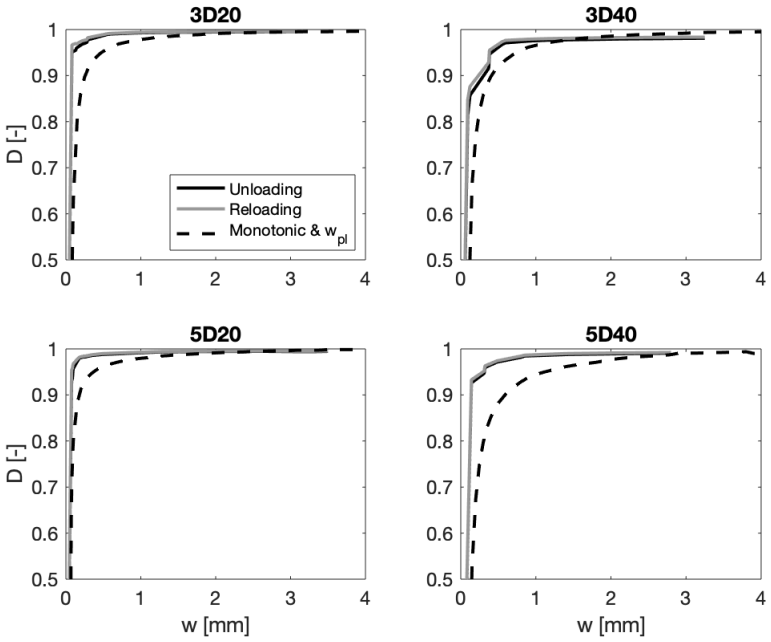

Figure 3.19: Experimentally determined unloading and reloading curves, compared to the predicted elastic stiffness by the monotonic curve and plastic deformation.

To obtain better results, separate linear regression curves are calculated in Figure 3.20. The decreased slope for 5D fibres illustrates the lower w_{pl} and therefore higher damage. Accordingly, 3D fibres show a slight decrease in damage. Figure 3.21 shows the change in damage when 3D and 5D fibres are treated separately. Because the change in curves in Figure 3.21 is very small, it is opted to further use the linear regression curve for all test groups together, as it is independent on the fibre characteristics. However, the results which are shown here, demonstrate that the w_{pl}-w_{unl} relation is slightly dependant on the fibre type, but independent on the fibre volume.

The experimental method and the method using the plastic deformation both have positive and negative aspects. The experimental damage curves have the advantage to differentiate between the unloading and reloading stiffness. However, this method

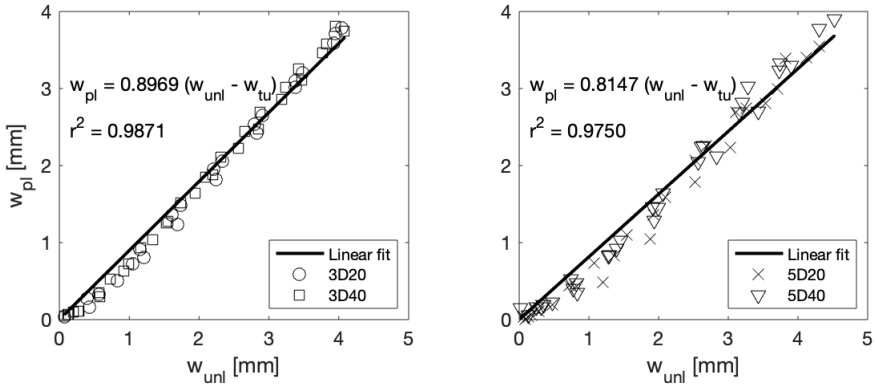

Figure 3.20: Plastic deformation calculations for 3D fibres (left) and 5D fibres (right).

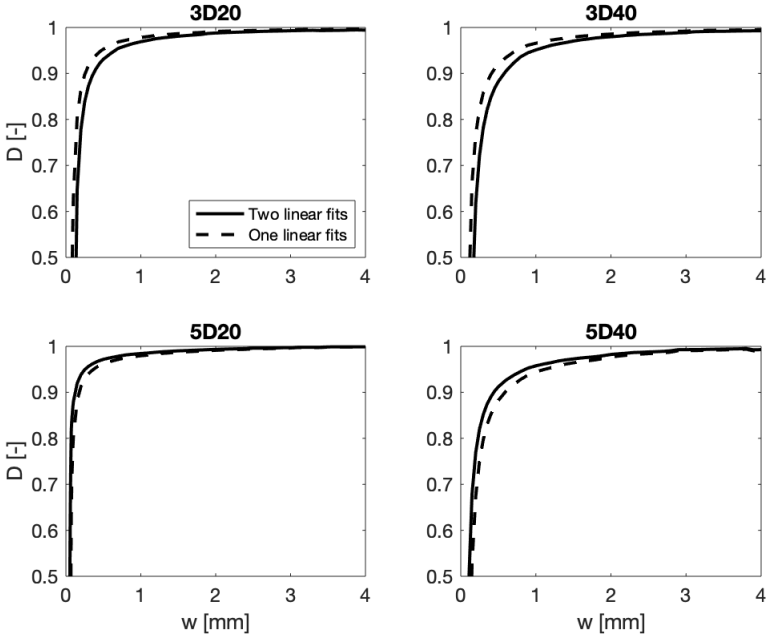

Figure 3.21: Comparison of the predicted damage using the single linear $w_{pl} - w_{unl}$ relation and the relations for 3D and 5D fibres separately.

involves many negative elements as well. The curve between the elastic deformation and the damage of the first cycle, is assumed to be linear as no information is available in this region. Next, the curves are also prone to experimental scatter. The damage curves highly depend on the amount of fibres. Finally, the curve is not smooth due to the discrete points at which cycles are carried out.

The drawback of the method using the linear relation, is that no difference can be obtained between unloading and reloading. However, when comparing the damage

curves of the DTTs to those of the 3PBTs (Figures 3.19 and 3.9), it can be concluded that the difference between unloading and reloading is negligible for DTTs. Unlike the experimental method, these curves also show a smooth behaviour throughout the whole interval of crack openings. This method is therefore preferred.

3.3.4 AE results and discussion

AE behaviour

Monotonic DTTs To observe the failure mechanism inside a specimen, the AE signals can be used. For most test specimens, these signals are received by six AE sensors, as described in Section 3.3.2. However, specimens 3D20 M1, 3D20 M2, 3D40 M1, 3D40 M2 and 3D40 M3 are monitored with only four AE sensors and therefore not comparable with the other results. 5D40 M1 has a similar problem, as two sensors malfunctioned and events were only registered for the remaining four.

When three of the six (or four) sensors detect a hit caused by the same source, an event is registered. The mean cumulative amount of events for each test group is shown in Figure 3.22. The graphs clearly show an increase of AE events when the amount of fibres is larger. The more fibres, the more cracks will initiate due to the increased fibre-matrix interaction.

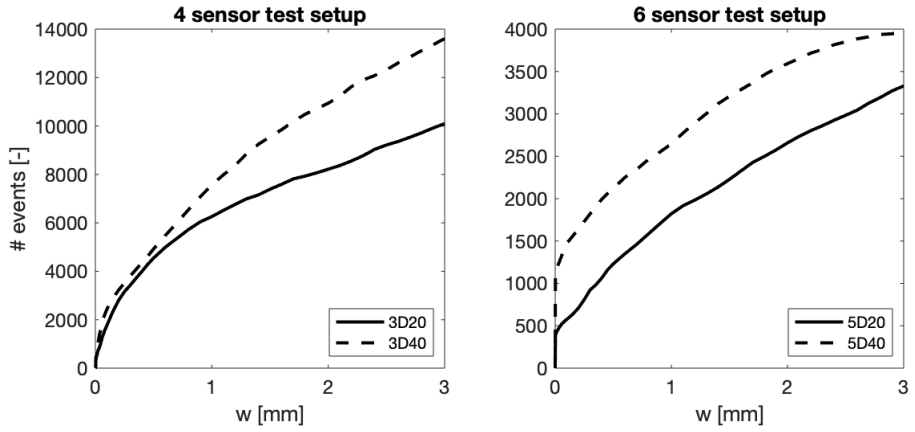

Figure 3.22: Cumulative amount of events during monotonic DTTs for 3D fibres (left) and 5D fibres (right).

An evolution of the amount of events in a single test specimen is shown in Figure 3.23 together with the energy of the signal. In this figure the result of the representative specimen 3D20 M4 is shown, as six AE sensors are used during the test and the observed amount of fibres corresponds well with the nominal amount of Table 3.8.

Figure 3.23 shows that the damage progress of the specimen can be divided into four stages. In the linear elastic stage (phase 1), no plastic deformations occur. As all strains in the material are elastic, no cracks are formed and therefore no AE events are received. Right before reaching the peak stress, some micro-cracks initiate.

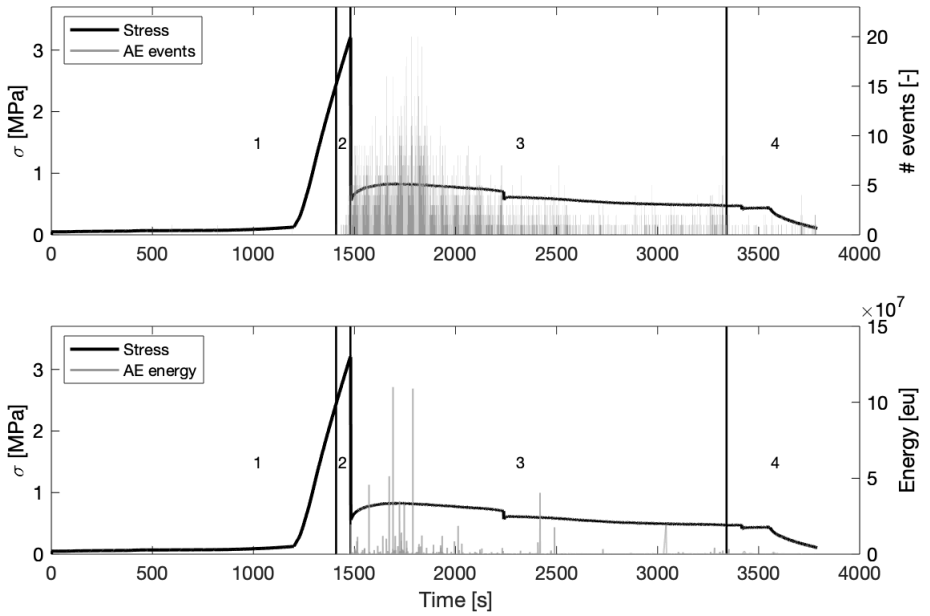

Figure 3.23: Amount of events and the energy received by the AE sensors for specimen 3D20 M4.

These generate little AE signals, with low energy (phase 2). After reaching the peak stress at around 1500 s, the number of events rapidly increases as the stress drops, accompanied by an increase in energy (phase 3). This third stage can be explained by the formation of a macro-crack. The crack causes the stress to drop significantly and lots of AE events are generated by matrix cracking. In this stage, the first signals are sent by matrix cracking, but soon also the fibres cause elastic waves inside the material due to their interaction with the concrete. Afterwards, at around 3300 s, the AE events stay constant and the energy is low, which implies the failure of the specimen (phase 4). Although the stages are only shown here for test specimen 3D20 M4, a similar conclusion can be made for all specimens.

Cyclic DTTs Figure 3.24 illustrates the mean cumulative amount of AE events during cyclic loading, for the test setup with six sensors. The cumulative AE events are clearly higher for the 3D40 fibres than for the 3D20 fibres. The larger amount of fibres in the notched section causes more AE activity, as was observed during the monotonic tests as well (Figure 3.22). Even though the 5D test groups contain less fibres, their cumulative amount of AE events is larger. The increased anchorage, strength and end-hooks of the 5D fibres results in more matrix cracking than for 3D fibres. When the fibres are pulled, two end-hoods need to be straightened instead of one. Additionally, the stresses inside the concrete concentrated around the fibres are larger due to the higher tensile strength. Figure 3.18 shows the same trend because the damage for 5D fibres is higher. This effect can be validated by Figure 3.20 as

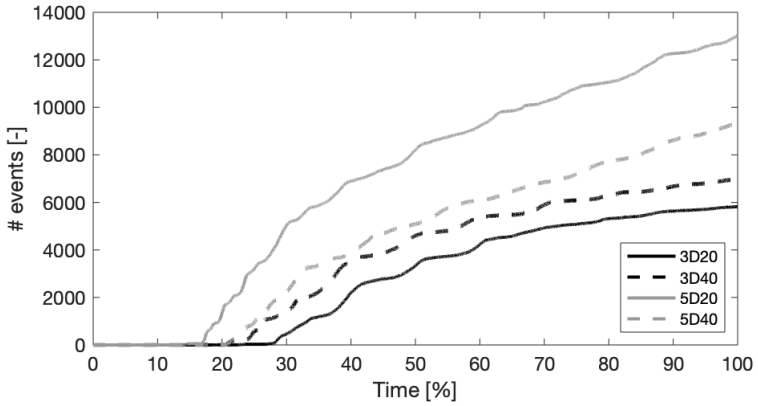

Figure 3.24: Cumulative amount of events during cyclic DTTs.

well, where the plastic deformations for 5D test specimens are slightly lower. This implies that the resistance against closure of the crack is less pronounced for 5D fibres. Increased matrix cracking around the fibres due to higher stresses could be a possible cause. Also elastic deformation of the fibres can attribute to the lower w_{pl}, which is elaborated further on.

However, the difference between the 5D20 and 5D40 test group is remarkable. Due to the increase of fibres in the 5D40 test specimens, an increase in AE events is expected. This is not observed in the experimental results. Because the malfunctioning of an AE sensor was checked and excluded, other causes are inspected. A possible hypothesis is explained here.

In comparison with the 5D40 test specimens, the fibres of the 5D20 test group contain larger tensile stresses. Theoretically, these stresses are two times as large because half the amount of fibres is expected. Therefore, the stresses transferred to the concrete are larger as well, and matrix cracking occurs sooner. When cracks are initiated in an earlier stage, more AE activity is recorded since the friction inside the specimen can transmit signals for a longer period of time. This explains why the same difference between 5D20 and 5D40 test specimens is not observed during monotonic loading. The load and crack width monotonically increase and the earlier development of cracks does not have an influence on the cumulative AE events. In this case, the amount of fibres is most important. Additionally, the reason why this only occurs for the 5D fibres and not for 3D, can be attributed to the higher tensile strength. After reaching the peak force, 3D fibres are more likely to quickly break or deform plastically. Therefore, the concrete matrix itself is less damaged

When analysing the cyclic results for one tests specimen, similar conclusions can be drawn as for the monotonic tests. AE events mainly occur after the peak strength is reached. After this event, the stress significantly drops as a macro-crack is formed and AE activity increases (cycle 5 in Figure 3.25). Before reaching the peak stress, only little AE events are registered, with low energy. When observing one cycle, less

AE events are registered during unloading, as no new cracks are formed. During reloading, the Kaiser effect is noticed. When the crack opening reaches its maximum value before unloading, new cracks are formed and therefore also more AE events registered. This effect will be elaborated further in this section, when calculating the load ratio.

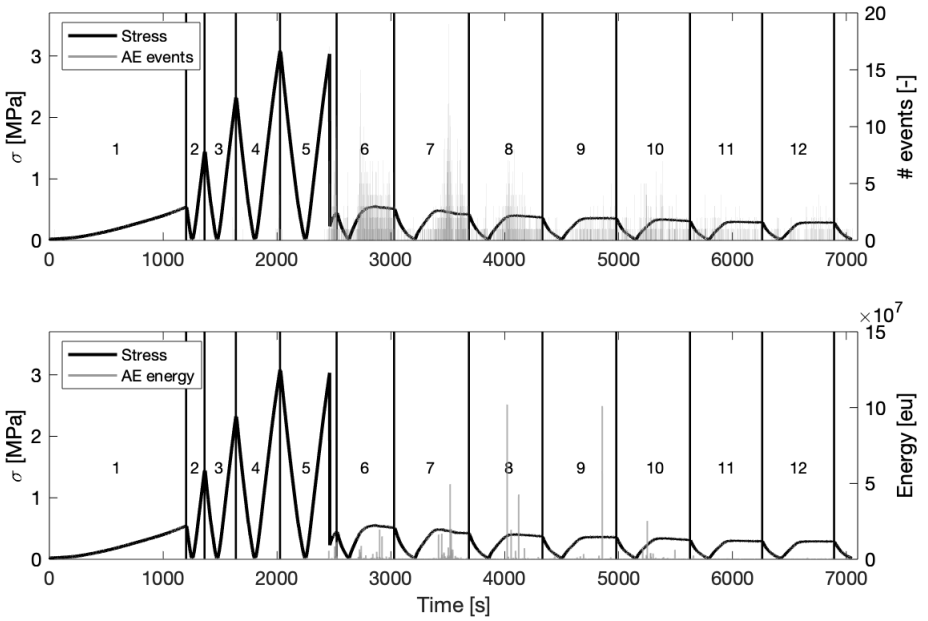

Figure 3.25: Amount of events and the energy received by the AE sensors for specimen 3D20 C1, and nomination of the cycles.

AF-RA analysis

Monotonic DTTs To confirm the different phases of Figure 3.23, an AF-RA analysis is performed as explained in Section 2.2.4. The average frequency is calculated by dividing the counts with the duration time. Further, the rise angle is determined by the division of the rise time with the amplitude. Events caused by noise, resulting in unusual signal characteristics, are first filtered out. Then, the division between tensile and mixed cracks is made by a general rule of thumb. The highest values of AF and RA determine the slope of the criterion, which is equal to 150 $kHz\,V/s$ in this study.

The results are shown in Figure 3.26 for the four different stages of the damage progress, together with the percentages of mixed cracks. Results above the diagonal are most likely caused by tensile cracks. All points beneath this diagonal are mainly caused by mixed cracks. In a direct tensile test, mixed cracks can only be obtained due to the friction between the fibres and concrete. As stated before, phase 1 contains no AE signals. Phase 2 consists of the signals produced during micro-cracking, which

is only caused by matrix cracking. Therefore, all events observed in phase 2 have a low RA value and are sent by tensile cracks. In phase 3, the effect of the fibres is observed, causing an increase of mixed cracks. The final phase only contains little AE events.

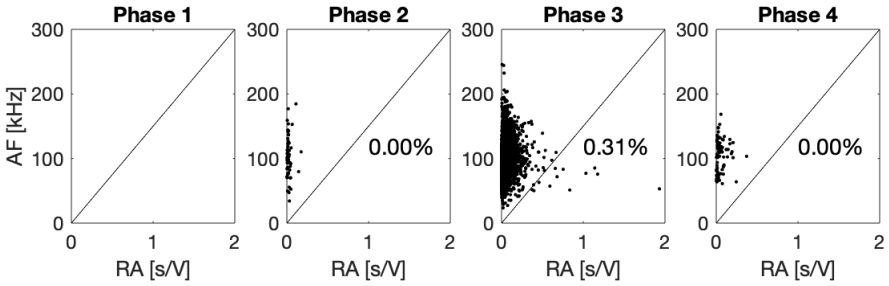

Figure 3.26: AF/RA analysis for different stages of the tensile test for specimen 3D20 M4.

The AF-RA analysis is repeated for representative tests of all test groups in Figure 3.27. As shown in this figure, the amount of mixed cracks increases with the fibre volume. Additionally, 3D fibres result in more mixed cracks than 5D fibres. Table 3.16 confirms both statements. The table shows the mean percentages of mixed cracks for all test groups, calculated for the tests with six AE sensors. The increase in mixed mode cracks for 5D fibres can be explained by their improved anchorage. These are supposed not to pull out during loading because of their "perfect anchorage" and therefore send less shear waves. Beside this effect, also the nominal amount of fibres in the notched section is smaller for the 5D test groups, resulting in fewer AE hits. However, the standard deviation is large, especially for the 5D40 test group.

Table 3.16: Mean percentage and standard deviation of mixed cracks for all test groups during monotonic loading.

	3D20	**3D40**	**5D20**	**5D40**
Mixed cracks [%]	0.25	0.36	0.14	0.26
s	0.08	-	0.00	0.17

Cyclic DTTs Four representative specimens of the cyclic tests groups are analysed by AF/RA as well, in Figure 3.28. In Table 3.17, the mean percentages of mixed cracks for all test groups are shown. The results clearly show the increase of mixed mode failure when the fibre volume fraction is increased, the same is concluded during monotonic testing. Also, 5D fibres show more mixed cracks than 3D fibres. The opposite was found when analysing the monotonic AE results. A possible reason could be the decreased value of w_{pl} for 5D fibres. As the stiffness decreases, the tests last longer and more friction is expected during the cycles. Friction between the fibres and concrete matrix is the main cause of mixed cracks.

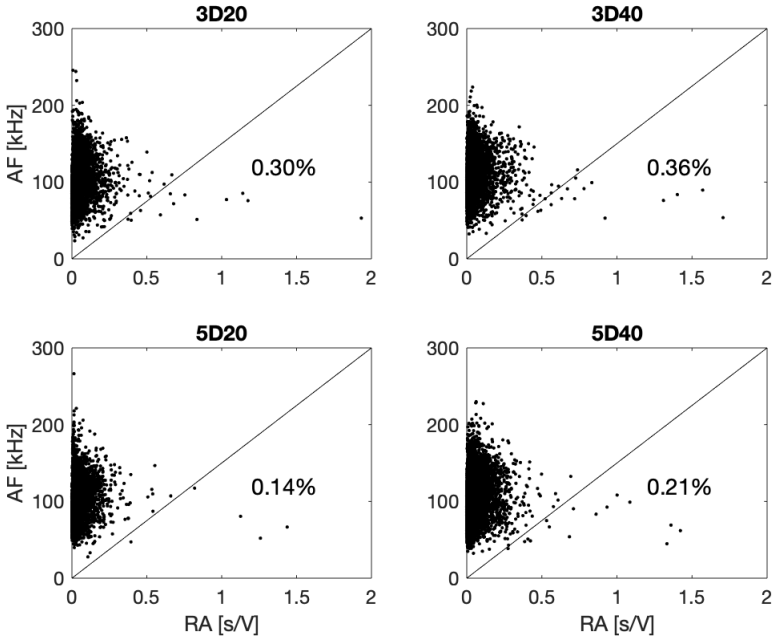

Figure 3.27: AF/RA analysis for all test groups during monotonic loading.

Table 3.17: Mean percentage and standard deviation of mixed cracks for all test groups during cyclic loading.

	3D20	**3D40**	**5D20**	**5D40**
Mixed cracks [%]	0.16	0.32	0.32	0.35
s	0.12	0.11	0.12	0.08

Figure 3.29 contains the evolution of the AF/RA analysis for every load cycle of test specimen 3D20 C1. These cycles are indicated in Figure 3.25. During cycles 1 to 3, almost no hits are received since the specimen is in the elastic phase. In cycle 4, micro-cracking results in several AE hits. These first four cycles mainly contain hits with low RA, as they are sent from matrix cracking. In cycle 5, the peak strength is reached, resulting in more hits. Furthermore, AF sightly decreases and RA increases for cycles after the peak strength, indicating the interaction between the fibres and concrete. However, few hits actually pass the limit between the tensile and mixed mode, because only 0.16% of hits are caused by mixed mode cracks (Figure 3.28).

Localisation

Next to the determination of the failure mode, also the localisation of the AE hits can be shown. Figure 3.30 illustrates the hits in a vertical plane for four representative specimens. Because of the notch, the main cracking occurs in the middle section of the specimen. Therefore the AE hits are filtered to only include the results less than 60 mm away from this middle section. This is the maximum distance the fibres at

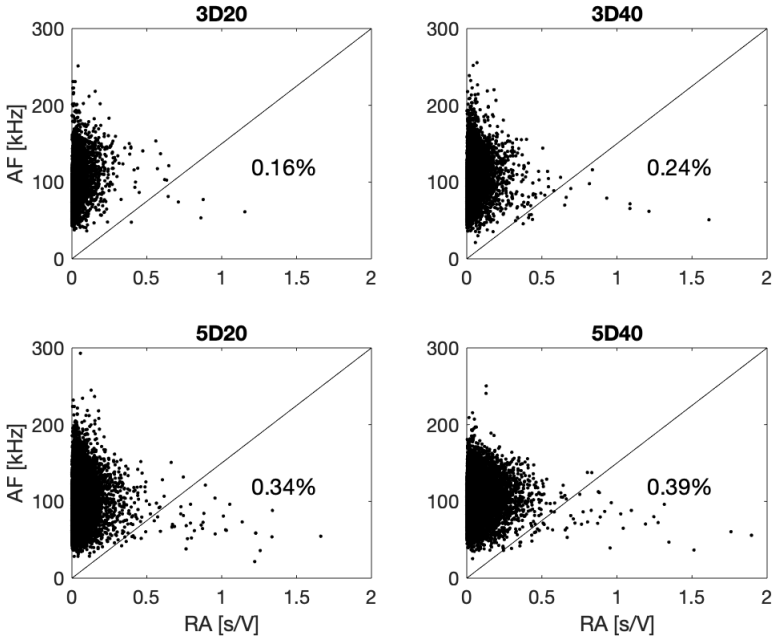

Figure 3.28: AF/RA analysis for all test groups during cyclic loading.

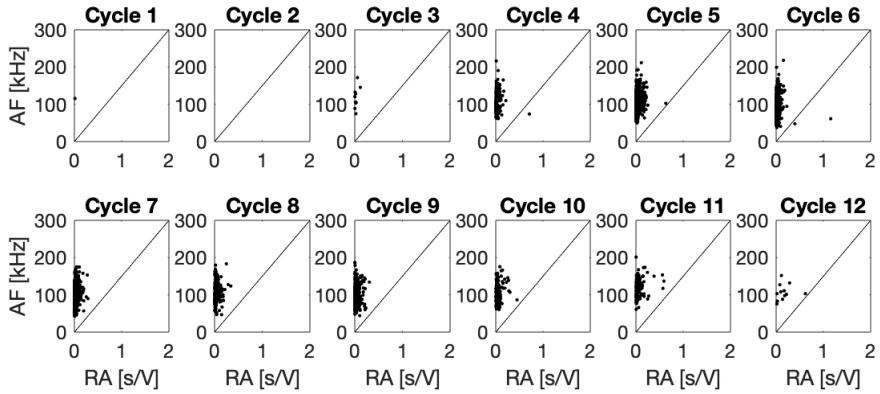

Figure 3.29: AF/RA analysis during every cycle, for specimen 3D20 C1.

the notch can reach, due to their length of 60 mm. Furthermore, all AE hits located outside the specimen, are filtered out.

The localisation of AE activity verifies that most cracks occur around the notched section. Additionally, it can be noticed that the pre-peak cracks, which are indicated in black, occur even more central to the specimen. These cracks develop due to matrix cracking, which only happens in the middle section. AE activity sent from fibre-concrete interaction, can also occur at distances of 60 mm away from the notch.

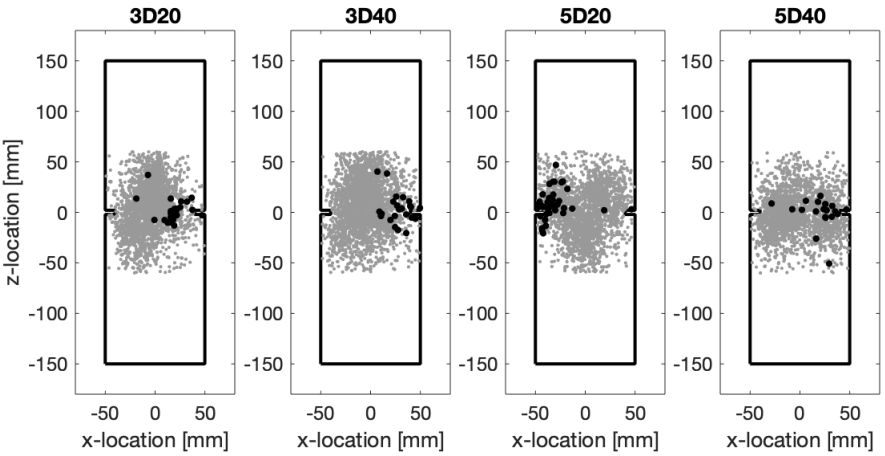

Figure 3.30: Localisation of AE hits during monotonic tests, projected on a vertical plane. The hits in the elastic zone are indicated in black.

The horizontal plane of Figure 3.31 shows that most of the first hits are recorded at the borders of the section. This shows that cracks start at the edge, and continue to grow towards the middle of the section until a large crack is reached and the fibres take over. These first hits are often located in parts of the section where afterwards, little AE activity is observed. The section first cracks at the weakest part, where little amount of fibres are situated and the concrete will more easily crack. Because most signals are sent from the interaction between the fibres and concrete, later results are concentrated around fibre clusters.

Finally, Figure 3.32 also contains the evolution of AE hits through time for a single specimen. The four phases are determined according to Figure 3.23. The linear elastic phase (phase 1) does not contain any hits. In phase 2, micro-cracking starts, and several hits are observed at the southeast side of the cross-section. These are caused by matrix cracking and located at the weakest side of the specimen. In phase 3, most hits are detected because fibre-matrix interaction now takes place. The core of these signals is therefore located at the opposite side of the cracks caused by matrix cracking. The final phase contains few hits, caused by the final remaining fibres in the notched section.

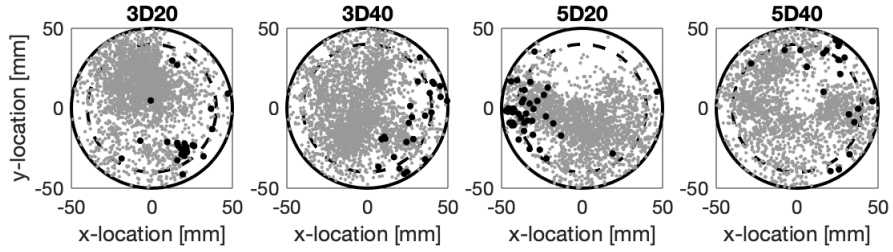

Figure 3.31: Localisation of AE hits during monotonic tests, projected on a horizontal plane. The hits in the elastic zone are indicated in black.

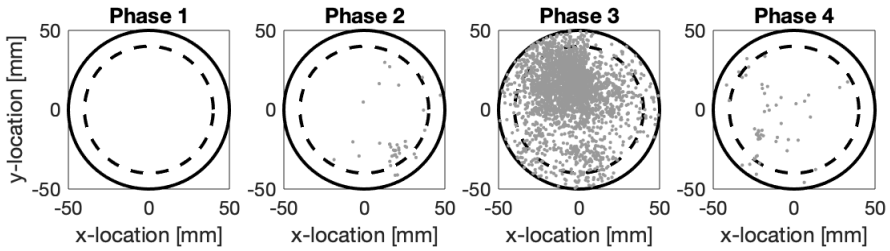

Figure 3.32: Localisation of AE hits for every phase during the monotonic test, for specimen 3D20 M4.

Cyclic DTTs The localisation is determined for the cyclic tests for four representative specimens as well. The same observations are made as for the monotonic tests. Most hits are located in the middle of the specimen, as seen in Figure 3.33. Additionally, the cracks start at the outer edges of the middle section, in areas with little amount of fibres (Figure 3.31). The AE hits caused by fibres are situated at other regions than where the crack initiates.

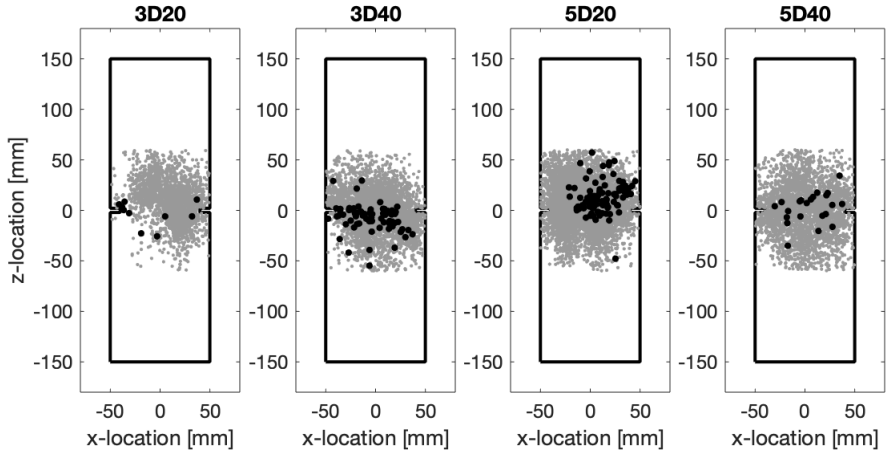

Figure 3.33: Localisation of AE hits during cyclic tests, projected on a vertical plane. The hits in the elastic zone are indicated in black.

The evolution of the location of AE hits is shown in Figure 3.35 for every cycle as indicated in Figure 3.25. The figure clearly illustrates the moment when the peak stress is exceeded. Cycle 3 and 4 contain several AE hits initiated during micro-cracking. Afterwards, in cycle 5, a sudden increase is observed, after reaching the peak strength. Following cycles each contain less AE hits than the cycles before. However, several areas of the section contain a cluster of hits, caused by the discrete fibres which are pulled out of the concrete matrix.

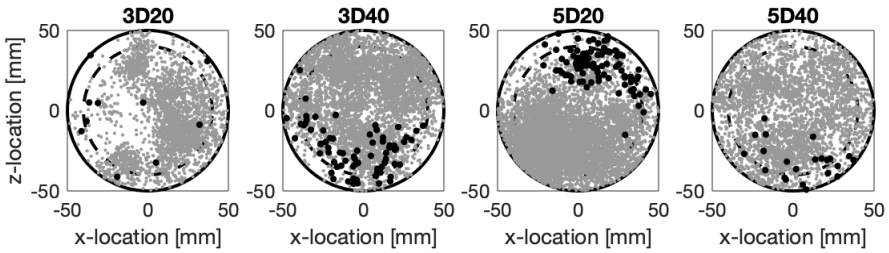

Figure 3.34: Localisation of AE hits during cyclic tests, projected on a horizontal plane. The hits in the elastic zone are indicated in black.

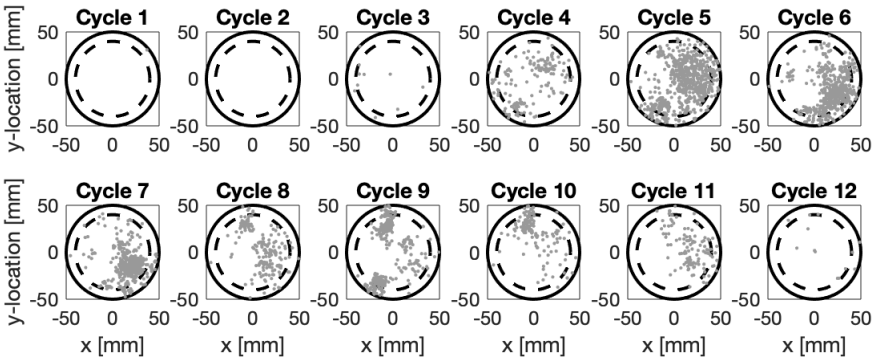

Figure 3.35: Localisation of AE hits during every cycle, for specimen 3D20 C1.

Calm ratio - load ratio

Next to the AF/RA analysis and localisation, the calm ratio - load ratio analysis can be executed for cyclic tests as well. This analysis explains the damage degree in a specimen, as explained in Section 2.2.4. However, before reaching the peak strength only few AE events are registered, certainly during unloading, and the calm ratio is therefore close to zero. After the peak strength, the difference in AE events during unloading and reloading is clearly visible (Figure 3.25). However, as the specimen is already heavily damaged, the calm ratio does not increase for every cycle. Therefore, it is opted to only show the evolution of the load ratio instead.

The evolution of the load ratio is illustrated in Figure 3.36 for every test specimen. The onset of the AE activity is defined here as the first event which is received by three or more sensors. Figure 3.36 clearly shows a decreasing load ratio when the amount of cycles increases. This indicates that more damage is induced in the specimen and therefore AE activity will be observed sooner during reloading. Theoretically, the transition between an undamaged and a damaged specimen is located at 1. In this case, AE events are registered right after reaching the previous maximum load. The graph shown here starts at load ratios higher than 1, illustrating the fact that the specimen is undamaged.

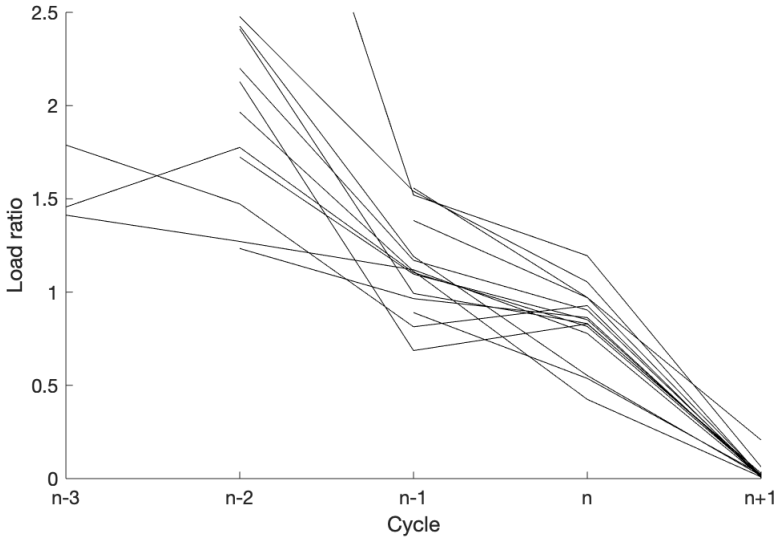

Figure 3.36: Load ratio evolution for all test specimen during cyclic loading.

When after the first cycle, the load increases and more AE activity is registered, the load ratio reaches closer to 1. This shows the existence of the Kaiser effect during cyclic loading. Increasing the load even more in the next cycles leads to a decrease of the load ratio, caused by the damage. After reaching the peak strength (at cycle n) and developing a macro-crack, AE events are constantly registered and the load ratio becomes nearly 0. Because not every specimen develops a macro-crack in the same cycle, the cycles in Figure 3.36 are indicated relative to the cycle at peak stress.

Overall results of the AE measurements

The damage progress inside the specimens can be analysed by observing the AE signals during experimental tests. Generally, almost no hits are detected during the linear elastic phase. Then, right before reaching the peak strength, micro-cracks are formed and few AE hits received. These hits contain little amount of energy, have low RA values and are localised in the weakest area of the cross-section. The evolution of the AE events and energy, AF/RA analysis and localisation therefore all validate the fact that these first cracks are caused by matrix cracking. The peak stress is accompanied by a sudden increase in AE events, caused by the development of a macro-crack inside the concrete.

After the stresses are redistributed, the energy in the signals increases and more mixed mode cracks are received. Also the localisation of the hits shifts to a different area of the cross-section, where most fibres are located. Executing all analysing methods shows that the fibre-concrete interaction causes most of the post-peak signals. These phases are identified in both the monotonic and cyclic DTTs. The cyclic results also show an interesting behaviour when observing the load ratio. The pre-peak cycles only contain AE events after reaching the previous load (Kaiser

effect). The development of a macro-crack can be observed by the evolution of the load ratio towards zero.

The difference in behaviour between all test groups can first of all be determined by the cumulative amount of AE events. More fibres results in more AE activity, caused by the increased fibre-matrix interaction. However, this statement is only valid within a certain fibre type. Comparing 3D and 5D fibres, an increase in AE events for 5D fibres is noticed, caused by the increased tensile strength and end-hooks. This can be related to the damage evolution in Section 3.3.3. The accumulated damage during DTTs is larger for 5D test specimen. Furthermore, the 5D20 specimens unexpectedly show the largest cumulative amount of AE events. These specimens crack earlier, presumably due to the higher stresses caused by the redistribution of the stresses over fewer fibres. Earlier cracking results in more friction during the cyclic tests. Secondly, the test groups differ by the amount of mixed mode cracks. A higher fibre volume fraction results in more mixed cracks, again because of the increased fibre-matrix interaction.

Expanding the common test setup to also include AE monitoring thus proves its worth. The cumulative AE events can be linked to the damage evolution and therefore also stiffness inside the material. AF/RA analysis classifies the cracks and the localisation indicates the exact areas where damage occurs. The load ratio is useful during cyclic loading, to determine the accumulated damage after each loading cycle.

3.4 Conclusion

Chapter 3 discusses the results obtained by performing 24 3PBTs tests and 31 DTTs. Both monotonic and cyclic tests are executed on four SFRC test groups with the same concrete composition of class C40/50. The fibre volume fraction varies between 0.25 $V\%$ and 0.50 $V\%$, and the fibre type is either 3D or 5D, depending on the end-hooks.

First, 3PBTs are performed and σ-$CMOD$ curves are obtained. The monotonic tests confirm that the pre-peak behaviour is not affected by the fibres, and the specimens with a volume fraction of 0.50 $V\%$ show a hardening behaviour. Subsequently, the residual tensile strengths of test group 3D20, 3D40, 5D20 and 5D40 result in the classification of 1b, 1.5b, 1d and 1.5e, respectively. The LVDT data shows that the deformation profiles are linear and the Euler-Bernoulli hypothesis can be used. The same can be said of the cyclic tests. Comparing the monotonic tests with the cyclic tests demonstrates the similarity between both σ-$CMOD$ curves. Therefore it can be concluded that the monotonic curves are the envelope curves of the cyclic results. Further, the loss of stiffness due to the accumulated damage of progressive loading is illustrated by damage curves. During reloading this damage is larger than during unloading. Additionally, a higher fibre volume fraction results in lower damages and 5D fibres cause an increase in damage.

Secondly, DTTs are executed on the same SFRC mixtures and assessed with AE monitoring. The results show that the amount of fibres in the cross-section is a crucial factor to determine the post-peak behaviour. Therefore, new test groups are formed to better resemble the nominal fibre amount. From the monotonic and cyclic tests, σ-w curves are obtained, which indicate again that the envelope curves of the cyclic behaviour can be taken equal to the monotonic curves. From the cyclic results, a linear relation between the crack width at unloading and the plastic crack width is derived. This relation is independent of the fibre characteristics. Consequently, the plastic crack width and monotonic curves are able to determine the elastic stiffness and therefore the damage during cyclic loading.

Next to the σ-w curves, also the acoustic emission signals are analysed. This data gives a good indication on the damage progress inside the material. Four phases have been distinguished: linear elastic phase, micro-cracking, macro-cracking and failure of the specimen. This damage development is based on cumulative AE behaviour, AF/RA analysis, localisation of the AE sources and the load ratio. The signals show the difference between tensile and mixed cracks by analysing AF and RA. Both monotonic and cyclic tests show only few mixed cracks caused by the interaction between the fibres and concrete. Most cracks are therefore tensile cracks which logically follows from DTTs. Next, localisation of the events shows that AE testing is usable to find the source of the cracks. Finally, the cyclic results demonstrate the Kaiser effect, as during reloading most AE events occur after reaching the highest load before unloading. This effect is illustrated by the load ratio. To conclude, AE monitoring proves to be a valuable method to detect, localise and classify damage.

Chapter 4

Sectional analysis

Sectional analysis can be performed using the results of a 3PBT to indirectly obtain results from a DTT or the other way around. The basic principles of sectional analysis are described in Section 4.1. Because of the difficulty and high costs of a DTT, an inverse analysis can be used to estimate the stress - crack opening relation for monotonic loading. In that case, only 3PBTs are needed to obtain the tensile behaviour of SFRC. This analysis is performed in Section 4.2, using sectional analysis. Afterwards a similar analysis is done for cyclic loading. A concrete cylinder is loaded progressively to determine the damage functions of the specimen. The combination of these results and the stress - crack opening relation for monotonic loading can predict the behaviour of a 3PBT under cyclic loading. The algorithm obtained for the cyclic loading is discussed in Section 4.3. A final conclusion is made in Section 4.4.

4.1 General description

To be able to understand the behaviour of SFRC during cracking, sectional analysis is used to observe the cracked section. It is necessary to obtain the stress and deformation profiles of the cross-section during the experiment, to properly execute sectional analysis. Because this study focuses on the results of experimental bending tests, the deformation is not uniform over the whole section. Therefore, the stresses are not evenly distributed, as expected during uniaxial loading.

To cope with this problem, sectional analysis descretises the section in several layers. Each layer represents a part of the section which is uniformly loaded. For every layer, the average deformation and stress can be calculated, using the constitutive laws or stress - crack opening curves. The higher the amount of layers, the more precise the results will be as the differences in deformation in one layer become smaller. However, a higher accuracy is accompanied by a higher computational time.

An overview of the approach is given in Figure 4.1. The notched section is divided into m layers, which is equal to 125 during this study. The height of each layer is therefore equal to 1 mm as the reduced height of the notched section equals

$h_{sp} = 125\,mm$. When the deformation profile over the height is known, the mean crack width w_j of the section can be determined. Applying the constitutive law to this section, results in a certain stress. The stress profile is obtained by performing this approach to all layers. In the following sections, this method is applied to several 3PBTs to obtain more insight in the monotonic and cyclic behaviour of four different types of SFRC.

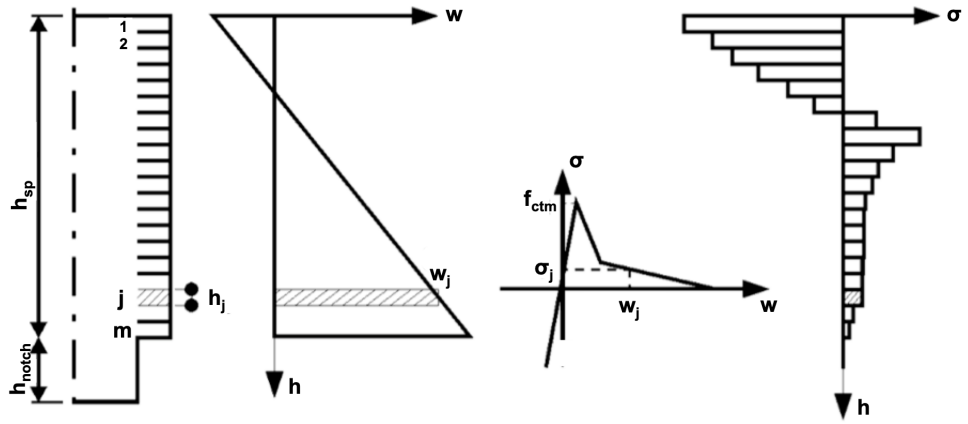

Figure 4.1: Determining the stresses through sectional analysis, adapted from [37].

4.2 Monotonic bending

Chapter 3 described the 3PBTs executed on the steel fibre reinforced concrete. The outcome of the monotonic tests consists of a series of CMODs with the mean values of the associated stresses obtained from three experiments per test group. These results can now be transferred to the desired σ-w curve, which is more easy to interpret. An overview of this section is given in Figure 4.2, indicating the flow of the model.

The model starts with a constitutive law, described in the literature (Section 4.2.1). This relation is an initial guess of the σ-w curve. Then, an analytical optimisation modifies the curve until the best fit between the experimental results and sectional analysis is found. This comparison can only happen if the σ-$CMOD$ curve can be constructed using the σ-w curve. Section 4.2.2 covers this transformation by calculating the deformation and stress profile at different CMODs. Next, the tensile response can be obtained from the results of a bending test in Section 4.2.3, which finalises the model. Section 4.2.4 contains the outcome of the model, for all test groups. The final section (Section 4.2.5) discusses the sensitivity of the obtained algorithm. This section explains the method by which the values of the different parameters of the model are chosen.

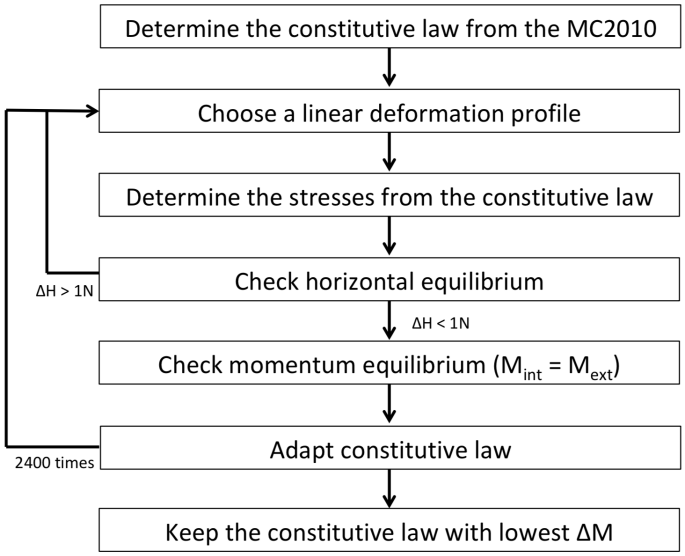

Figure 4.2: Schematic overview of the model for monotonic bending.

4.2.1 Constitutive law

Compression

During flexural tests, the upper part of the section is compressed and therefore a constitutive law is needed to relate the deformations to the stresses. The Thorenfeldt curve is used to define this relation [64]. Although the Thorenfeldt curve describes the behaviour of plain concrete, it can still be used for SFRC as the behaviour in compression is independent of the fibres. Because the concrete composition is identical for all test specimen, the constitutive law in compression is equal for all test groups. The stress - strain relation is shown in Figure 4.3 and described by following formulas [67]:

$$\sigma = \varepsilon \cdot \frac{f_{cm}}{\varepsilon_p} \left(\frac{n}{n - 1 + \left(\frac{\varepsilon}{\varepsilon_p}\right)^{n-k}} \right) \tag{4.1}$$

$$n = 0.80 + \frac{f_{cm}}{17} \tag{4.2}$$

$$k = \begin{cases} 1 & \text{if } 0 < \varepsilon < \varepsilon_p \\ 0.65 + \frac{f_{cm}}{62} & \text{if } \varepsilon_p \leq \varepsilon \end{cases} \tag{4.3}$$

$$\varepsilon_p = \frac{n}{n-1} \cdot \frac{f_{cm}}{E_{cm}} \tag{4.4}$$

with

σ	The stress [MPa]
f_{cm}	The mean cylindrical compressive strength [MPa]
E_{cm}	The mean secant modulus of elasticity of concrete [MPa]
ε	The strain [-]

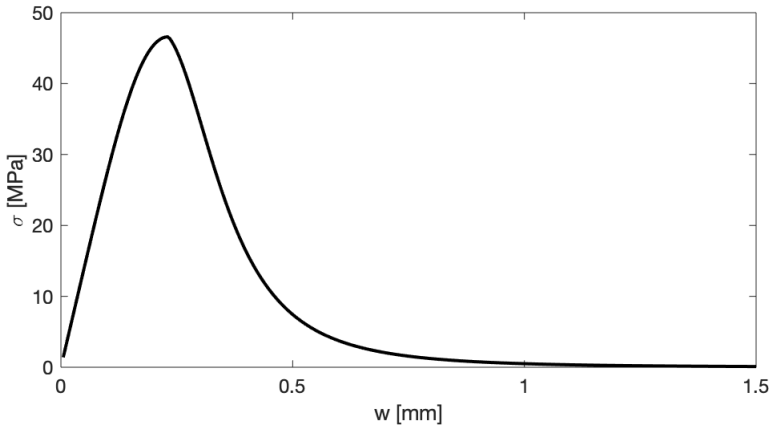

Figure 4.3: Compressive constitutive law based on a Thorenfeldt curve, for $E_{cm} = 35\,GPa$ and $f_{cm} = 46.61\,MPa$.

The compressive strength (f_{cm}) is determined in Section 3.1.3 together with the elastic modulus (E_{cm}). Because the relation between σ and w is desired, the results need to be converted from the strain to the crack opening. The relation of Equation 3.10 correlates both values [29]. The characteristic length l_{cs} in this equation is equal to $125\,mm$, which is the height of the notched section. If the section is compressed, ε and therefore also w becomes negative. The obtained crack width w is thus fictitious because no actual crack opening can be observed. However, the crack width will further in this thesis refer to the deformation of the section.

Tension

The behaviour of SFRC in tension can be described by the constitutive laws mentioned in the Model Code [29] and the paper by di Prisco et al. [21]. These formulas are a first estimation, serving as the base for the future analytical model [67]. The first step in constructing the σ-w curve for tension is to determine the pre-peak behaviour. The Model Code states the mean uniaxial tensile peak strength f_{ctm} is equal to:

$$f_{ctm} = \frac{0.06 \cdot h_{sp}^{0.7}}{1 + 0.06 \cdot h_{sp}^{0.7}} \cdot f_L \tag{4.5}$$

The σ-w curve before this peak stress is constructed with the formulas in Equation 4.6. At around 90% of the uniaxial tensile stress, micro-cracking begins, and the

stiffness decreases [29]. Even though the stiffness decreases, the stress keeps increasing until the uniaxial tensile strength is reached. This part of the constitutive law is independent on the fibres, and therefore valid for plain and fibre reinforced concrete.

$$\sigma = \begin{cases} E_{ci} \cdot \varepsilon & \text{if } \sigma \leqslant 0.9 \cdot f_{ctm} \\ f_{ctm} \cdot \left(1 - 0.1 \cdot \frac{0.00015 - \varepsilon}{0.00015 - 0.9 \cdot f_{ctm}/E_{ci}}\right) & \text{if } 0.9 \cdot f_{ctm} < \sigma \leqslant f_{ctm} \end{cases} \tag{4.6}$$

The tangent modulus of elasticity E_{ci} is calculated according to Equation 3.9.

All needed parameters are calculated in Chapter 3, and the pre-peak behaviour can be determined. Similar to the Thorenfeldt curve, the previous formulas calculate the σ-ε relation of the SFRC. Therefore a conversion to the σ-w curve is needed. Equation 3.10 again relates the crack width to the strain over the characteristic length. As Equation 4.6 is valid before reaching the peak stress, no macro-crack will have been initiated and therefore the crack width is again fictitious. This pre-peak w is equal to the elastic strain over the length l_{cs}. This is illustrated by Figure 4.4, after Hillerborg et al. [35]. The total deformation is equal to the sum of the fictitious crack width and the real crack opening. However, the area beneath the σ-δ curve and the σ-w curve, also called the fracture energy, is identical. This portrays the fact that the elastic strain depends on the stress inside the cracked section.

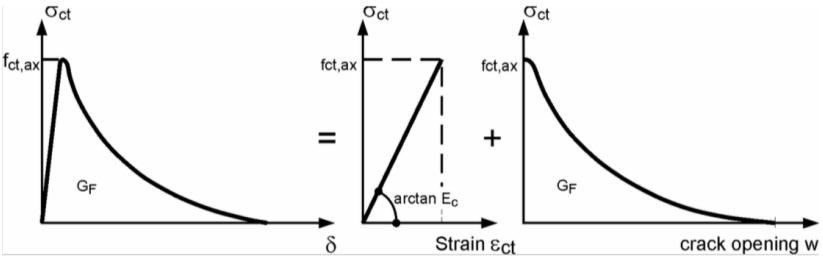

Figure 4.4: Fictitious crack model, measured σ-δ relation separated into a σ-ε and a σ-w relation, taken from [37].

Now that the pre-peak behaviour is determined, the post-peak behaviour can be described with a bilinear curve. The first part is written as Equation 5.1-31 from MC2010 [29], describing the stress - crack width relation for plain concrete. This part of the post-peak curve takes into account the matrix cracking. However, the equation is translated over the elastic crack width at peak strength ($0.00015 \cdot l_{cs}$), as illustrated by Figure 4.4 and Equation 4.7. Therefore, the elastic strain at peak stress will be added to all post-peak crack openings, which slightly overestimates the deformation of the cross-section. However, the elastic deformation is very small compared to the plastic deformation, and the error can thus be neglected. Additionally, the model described in the next sections adjusts this constitutive law to better fit the experimental results.

$$\sigma = f_{ctm} \cdot \left(1 - 0.8 \frac{w - 0.00015 \cdot l_{cs}}{w_1}\right) \tag{4.7}$$

This equation is only valid for $w - 0.00015 \cdot l_{cs} < w_1$, with

w The crack opening [mm]
w_1 $= G_F / f_{ctm}$
G_F The fracture energy [N/mm] $(= 73 \cdot f_{cm}^{0.18})$
ε The strain [-]

The second part of the bilinear curve consists of a linear relation between two points, as explained in Section 2.1.2. This part of the tensile behaviour takes the influence of the fibres into account. Equations 2.5 and 2.6 complete the initial estimate of the constitutive law for SFRC. Figure 4.5 illustrates the total tensile behaviour for test group 3D20.

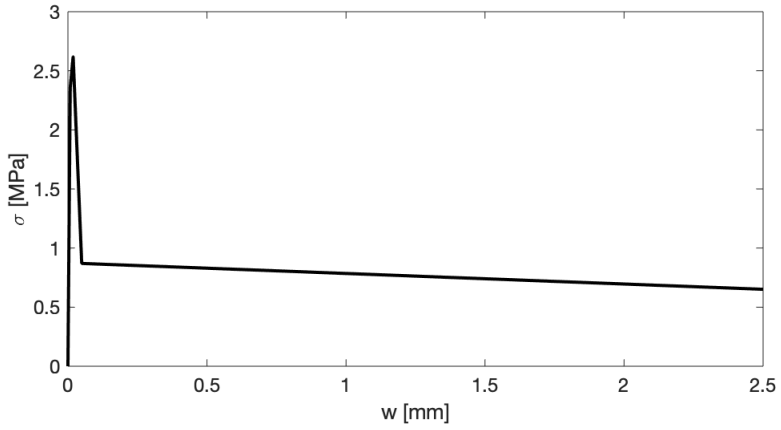

Figure 4.5: Tensile constitutive law for test group 3D20.

4.2.2 Obtaining σ-CMOD from σ-w

When the constitutive laws of both compression and tension are constructed, the σ-$CMOD$ curve can be derived to compare the calculated results to the experimental results of the 3PBTs. To gain this relation, the notched section of the beam needs to be in equilibrium. Both horizontal and momentum equilibrium need to be fulfilled. To obtain the forces acting on the cross-section, first the deformation profile can be constructed. From this, the stresses can be calculated, using the previously defined constitutive law, schematically illustrated in Figure 4.1. These stresses are used to calculate the resulting horizontal force and bending moment.

To find the deformation profile, an Euler-Bernoulli beam is assumed. This assumption is justified by the linear deformation profiles obtained by the LVDT data during flexural testing (Section 3.2.2). Because the deformation profile is linear over the whole cross-section, it can be defined by only two points. One point is already known, positioned at the location where the CMOD is measured. The y-coordinate is equal to $-20\,mm$, as the measuring system is installed $20\,mm$ below the beam.

The x-coordinate for this point is equal to the $CMOD_i$ in every loading step i. The second point is chosen at the neutral axis, where the x-coordinate equals 0, and the y-coordinate equals the height of the neutral axis y_N. This height is altered in an algorithm, which is explained further on, until the horizontal equilibrium is fulfilled.

$$\Delta H_i = b \cdot \sum_{j}^{m} (\sigma_j \cdot h_j) \tag{4.8}$$

The width of the beam b is equal to $150\,mm$, m is the amount of discretisation points and σ_j is the stress for each layer, calculated with the constitutive law and the deformation at point j. The height h_j is dependant on the discretisation, and equal to h_{sp}/m. The neutral axis at the first iteration is chosen in the middle of the section. As the algorithm continues, the neutral axis moves upwards if ΔH is negative, and downwards if ΔH is positive. Every new y_N is chosen in the middle of the remaining interval in which ΔH can be zero. Demanding that $\Delta H = 0$ takes too much computational effort, which is why the iteration process continues until $\Delta H < 1N$ and the interval of a possible y_N is smaller than $0.01\,mm$.

Now that the horizontal equilibrium is fulfilled, the resulting bending moment can be calculated as the difference between the internal and external bending moment:

$$\Delta M_i = |M_{int,i} - M_{ext,i}| = |b \cdot \sum_{j}^{m} (y_j \cdot \sigma_{j,i} \cdot h_j) - M_{ext,i}| \tag{4.9}$$

This ΔM_i can be considered as the error of the constitutive law, as it should be equal to 0. The external bending moment is calculated assuming a simply supported beam.

$$M_{ext,i} = \frac{F_i \cdot L}{4} \tag{4.10}$$

Furthermore, the σ-$CMOD$ relation of the analytical model can be constructed by calculating the stress for every $CMOD_i$. The stresses are obtained by combining Equations 2.4 and 4.10, which is valid for simply supported Euler-Bernoulli beams.

$$\sigma_i = \frac{6M_{int,i}}{bh_{sp}^2} \tag{4.11}$$

4.2.3 Obtaining σ-w from σ-CMOD

Now that the error (ΔM_i) can be calculated between the σ-$CMOD$ curves obtained from 3PBTs and the sectional analysis based on the constitutive law of the MC2010, it needs to be minimised. The error can be reduced by altering the constitutive law in different iterations. Because steel fibres only change the tensile behaviour of concrete, the model is mainly focused on this part of the constitutive law. Therefore only the tensile behaviour of the σ-w relation changes to optimise the constitutive law. The curve is composed out of several points, which are able to move in x- and y-direction to find an optimal relation. The amount of post-peak points (ppp) can

increase to better resemble the behaviour of the SFRC. Here, the chosen amount of post-peak points is six. Before reaching the peak strength, two points describe the elastic behaviour, making a total of eight points. Section 4.2.5 further elaborates the optimal amount of points.

For both directions of every point, N different positions are checked. The point stays in the position of the lowest ΔM, summed over all $CMOD_i$. Next, the algorithm moves to either the other direction of the same point, or to the next point. This implies that for one loop of the algorithm, the error of $2 \times 8 \times N$ different constitutive laws is calculated. The path every point makes, is indicated in Figure 4.6. In x-direction, the points can not surpass the ranges of the adjacent points. In y-direction, the point can go 0.5 MPa upward or downward, as long as it does not become negative. This optimisation happens three times for every post-peak point ($loops = 3$). The optimal number of N and $loops$ is again determined in Section 4.2.5.

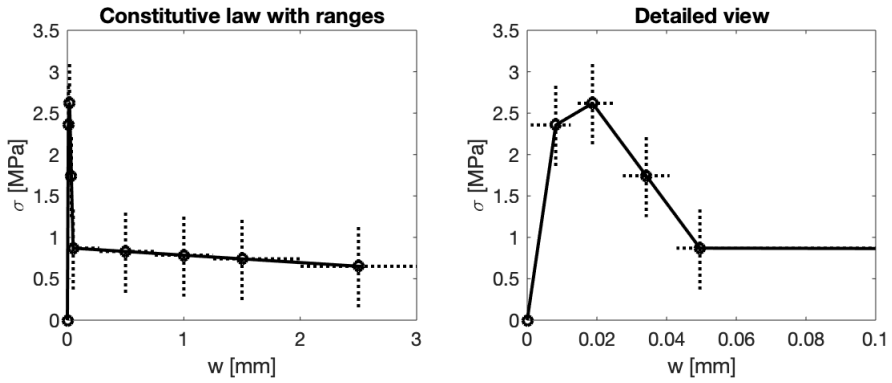

Figure 4.6: Constitutive law for tension with ranges, for 3D20.

4.2.4 Results and discussion

σ-w and σ-CMOD curves

The modelled σ-w curves for both types of fibres and for both volumes, are shown in Figure 4.7 together with the relation proposed by the Model Code [29]. The points which are transformed, starting from the MC2010, are indicated in the figure as well. Mainly the specimens with high percentages of fibres show a large difference between the analytical obtained relations and the relation obtained by the MC2010.

After the stress drop, representing the matrix cracking, the stresses in the cross-section are redistributed and the fibres start to resist the tensile stresses. Therefore the stresses increase again, mainly for the volume fractions of 0.50 $V\%$. When the amount of fibres is higher, more energy can be dissipated in the cracked section. However, as w becomes higher, fibres start to pull-out and break, hence the flattening of the curve for test groups 3D40 and 5D40. This mechanism cannot be accurately captured by the MC2010, because a linear curve represents the post-peak behaviour.

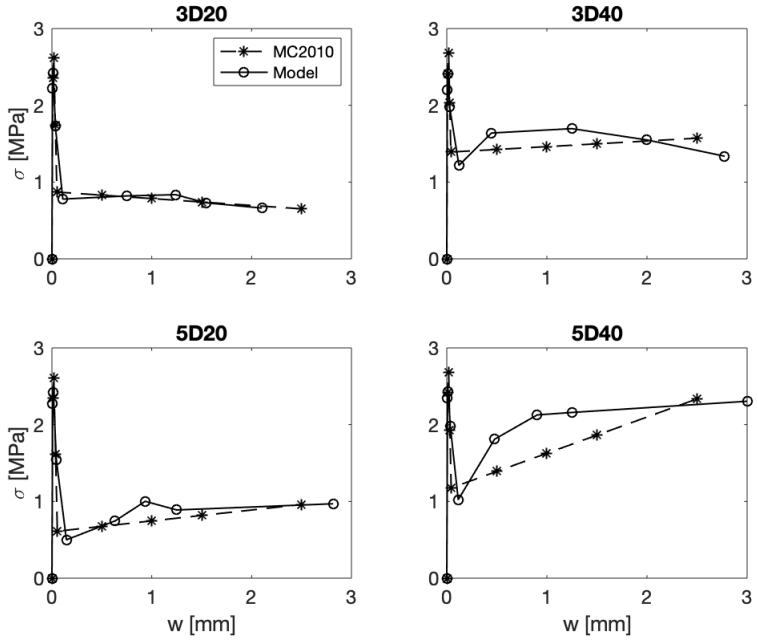

Figure 4.7: σ-w curve for all test specimens.

The bilinear post-peak assumption of the MC2010 is easier to apply, but the uniaxial tensile post-peak behaviour can not be determined precise enough. The non-linear behaviour can be observed in Figure 4.8 as well, where a comparison is made between the experimental results, the modelled results, and the results from the MC2010 for the σ-$CMOD$ curves. The analytical optimisation gives a result closer to the experimental observations, which is logical because the modelled results are fitted to the experiments. However, the Model Code again assumes a linear progression of the strength.

To compare all results, Table 4.1 contains the total error for all compositions. This error is the mean deviation of the modelled bending moment from the experimental bending moment, over all $CMOD_i$. The error for MC2010 is clearly higher. However, the error for the model is really small because this parameter is minimised in the model.

Table 4.1: The average error for all test specimens, calculated with the analytical model and MC2010.

	3D20	**3D40**	**5D20**	**5D40**
Model	0.96%	0.64%	1.63%	1.73%
Model Code 2010	4.10%	7.08%	8.81%	11.48%

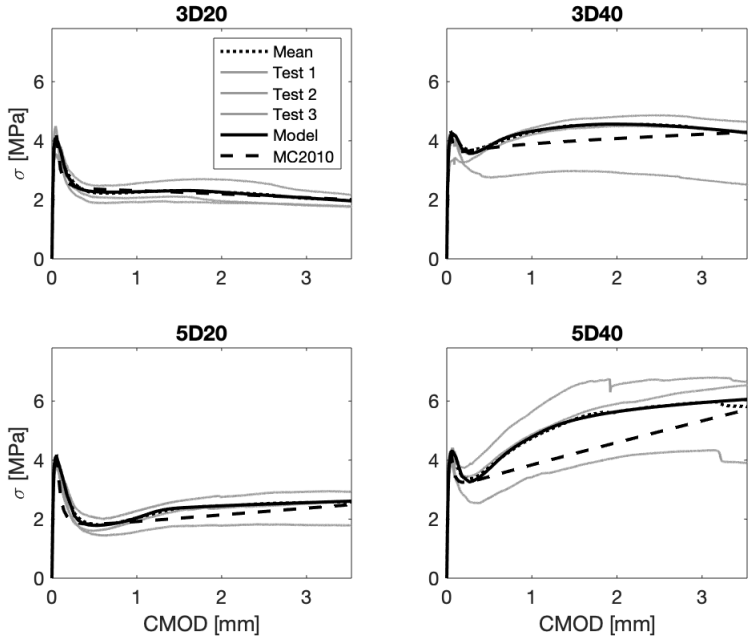

Figure 4.8: σ-$CMOD$ curve for all test specimens, with the mean of the experimental tests and the individual tests included.

Figure 4.8 also shows the experimental results of all twelve executed tests, three tests for every test group. These graphs show that overall, the Model Code gives a good estimation of the tensile behaviour, as the curve stays between the individual test results. Only for CMODs close to the peak strength, the deviation is found to be larger. Overall, the use of the Model Code returns acceptable results for a relatively simple method.

A more detailed graph is shown in Figure 4.9, the curves show that the MC2010 slightly overestimates the peak strength of the material. However, the main difference is found in the steepness of the curve right after the peak strength.

Stress profile

Different stress profiles are shown in Figure 4.10 for all test groups. At low CMODs, the stress profiles are similar for all test specimen. When the CMOD becomes higher, a deviation between the test specimen with different fibre volumes is noticeable. This can be explained by Figure 4.8, where the biggest difference in stress between all test groups is found for higher CMODs. When the amount of fibres is 40 kg/m^3, the stresses in tension become higher as more energy can be absorbed. Due to the increasing stresses in tension, also the stresses in compression need to be higher to meet the requirement of the horizontal equilibrium. The difference in fibre type is less pronounced. Fibres of type 5D can absorb slightly higher stresses, but the influence of the volume of fibres is more important.

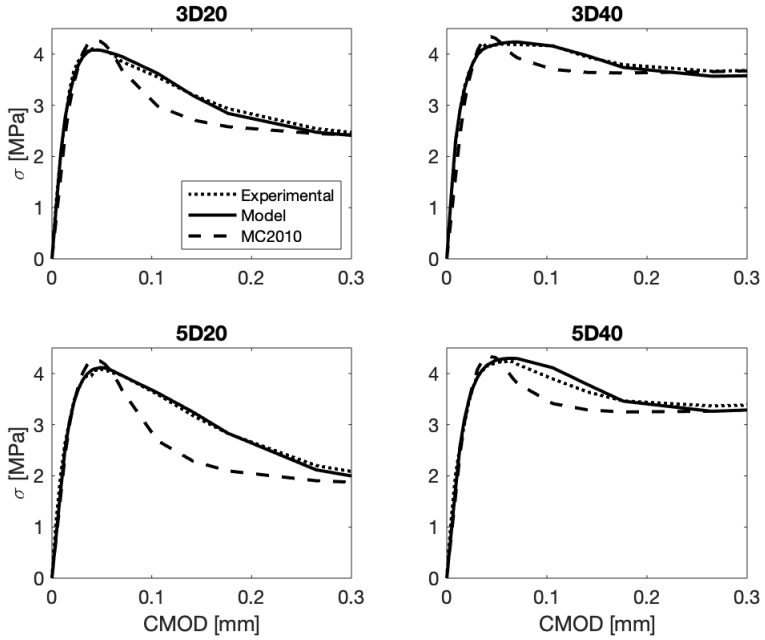

Figure 4.9: Detailed σ-$CMOD$ curve for all test specimens.

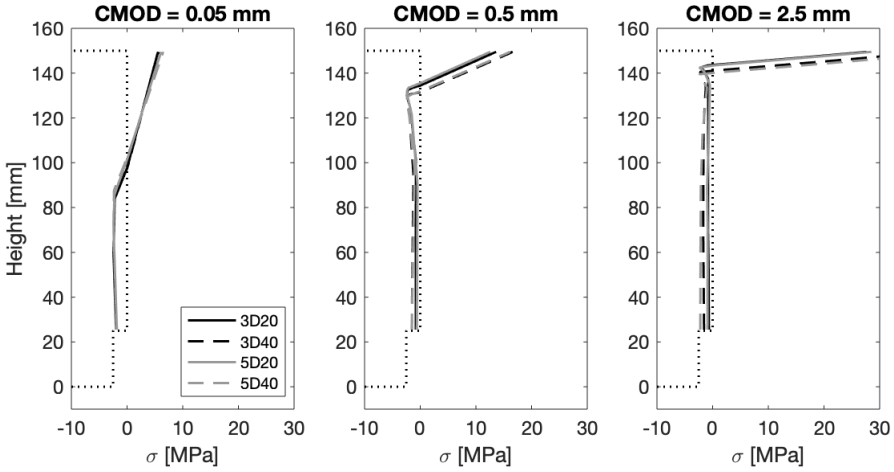

Figure 4.10: Stress profiles at three different CMODs.

The same trend is noticeable in Figure 4.11. Again, the biggest differences occur at higher CMODs. The highest compressive stresses are found for test group 5D40 because the tensile stresses are the highest. The graphs of 3D20 and 5D20 show an interesting progress due to their intersection. First, test group 3D20 has the highest compressive stresses, but afterwards the compressive stresses of 5D20 become higher. Figure 4.7 explains this phenomenon as the tensile stresses are firstly lower for 5D20, but become larger as w increases.

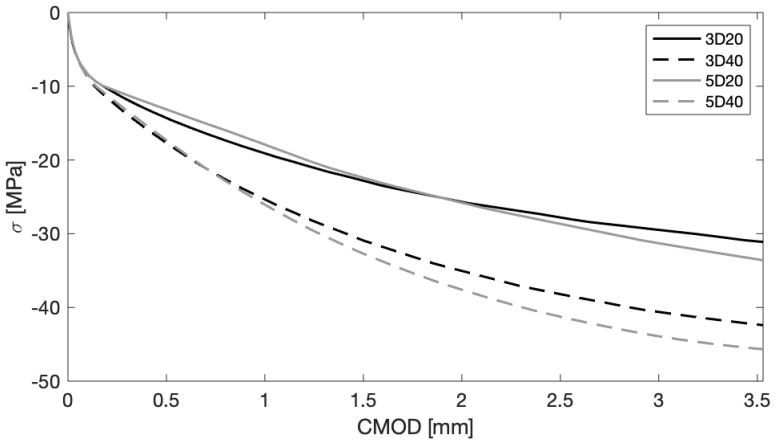

Figure 4.11: Highest compressive stresses.

Deformation profile

Figure 4.12 shows the deformation profiles obtained by the model at three different CMODs, for all test groups. Because the deformation profiles are all similar and no clear distinction can be observed, the height of the neutral axis is shown in Figure 4.13 as well. The neutral axis is lowest for test group 5D40, because of the higher uniaxial tensile strength. To obtain higher compressive stresses to compensate the tensile stresses, the neutral axis is moved downwards.

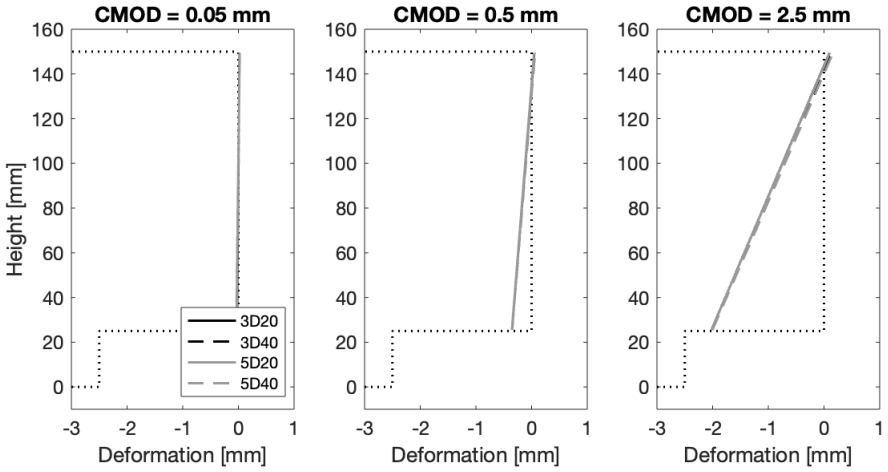

Figure 4.12: Deformation profiles of all test groups during monotonic loading.

To validate the results of the neutral axis, a comparison is made with the measured deformations during the 3PBT in Figure 4.14. Six LVDTs are placed on the beams at different heights: -20, 35, 60, 90, 120 and 145 mm. To calculate the height at which the deformation is zero, linear interpolation is used between all LVDT data.

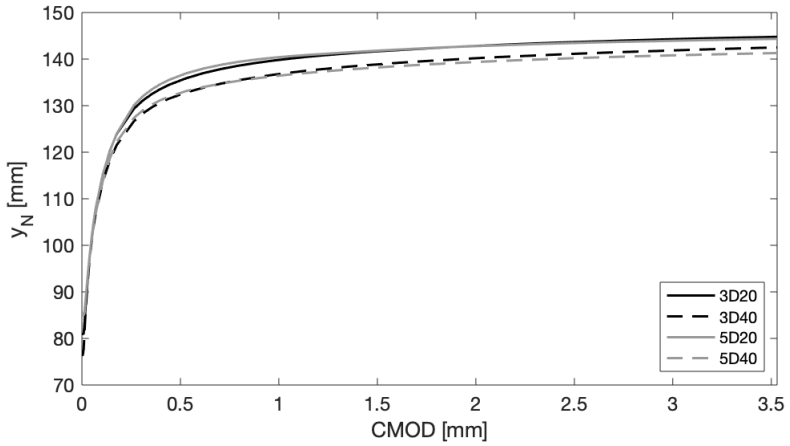

Figure 4.13: Evolution of the neutral axis during monotonic loading.

However, when the neutral axis becomes higher than 145 mm, an extrapolation is used and the results become less reliable. This is indicated with the vertical line in the figure. The model closely resembles the experimental measurements, confirming the calculations.

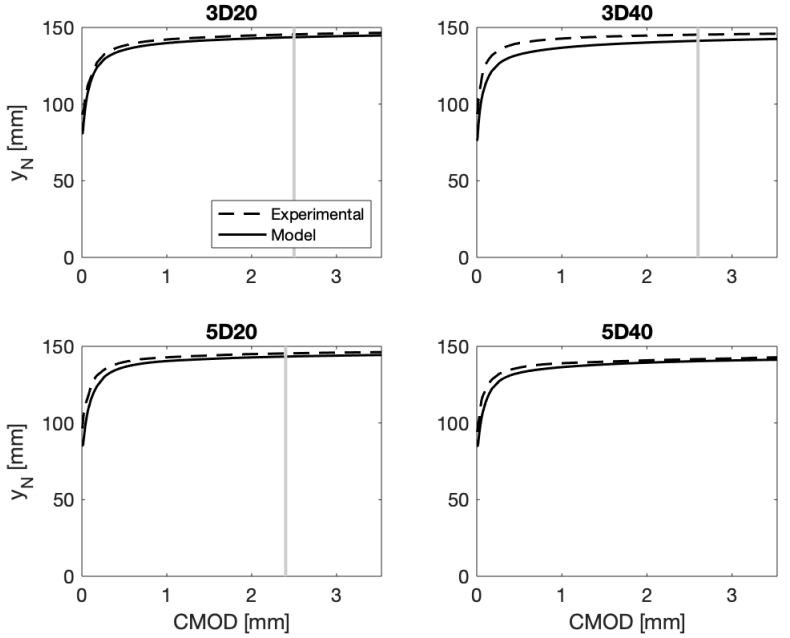

Figure 4.14: Comparison between the experimental and modelled neutral axis during monotonic loading.

Comparison to the DTTs

The results obtained by the model can now be compared to the actual direct tensile tests. However, the deformations are not yet compatible. The model creates a constitutive law where the crack width contains both the elastic and plastic deformations, as shown in Figure 4.4. The elastic strains are assumed to contribute to the cracked section over a length l_{cs}, equal to 125 mm for the bending tests. However, for the cylinders tested in the DTTs, the measured crack width only includes the plastic deformations. Therefore, the elastic deformation should be added according to Hook's law and Equation 3.10:

$$w_{3PBT} = w_{DTT} + \frac{\sigma}{E} \cdot l_{cs} \tag{4.12}$$

Because the modulus of elasticity, determined in Equation 3.9, is large compared to the tensile stresses, the impact of Equation 4.12 is limited. The comparison between the output of the model, and the experimental results is shown Figure 4.15, for the new test groups determined in Table 3.10.

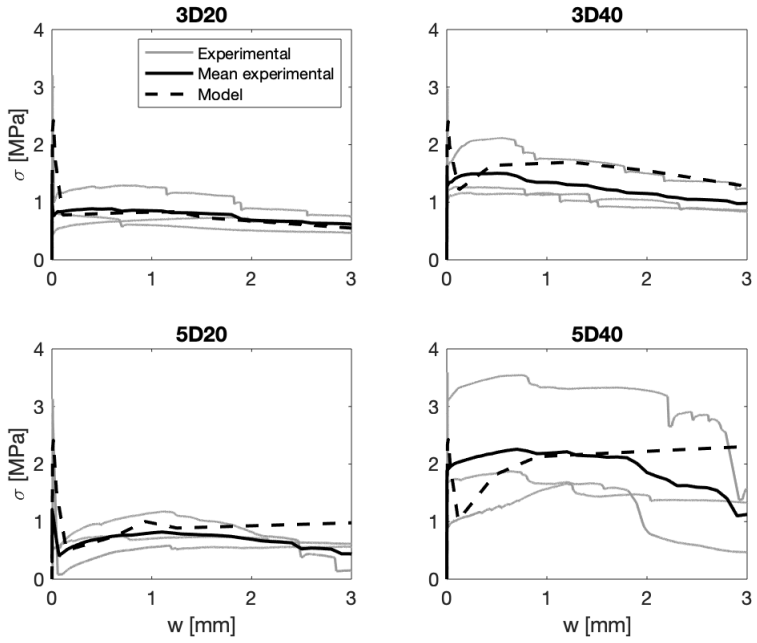

Figure 4.15: Comparison between the experimental obtained DTTs results and the results of the model.

The figure shows good agreements between the post-peak behaviour of both the model and experimental results for smaller CMODs. Especially the model for the 3D fibres shows a good resemblance. The 3D40 experimental tests are slightly lower than the model predicts, which can be explained by Table 3.14. The mean fibre amount of the 3D40 test group (25) is smaller than the average nominal amount

($n_f = 28.4$). Therefore, the experimental post-peak behaviour shows smaller tensile stresses.

The 5D fibres however show weaker agreements, according to the model, the stresses would keep increasing for higher crack openings. For the 5D40 test group, the different behaviour is explained by multiple cracking, which occurred for two out of the three tests shown in the figure. Therefore, the stresses will suddenly drop, and the measured crack width at the notch almost remains the same. This is discussed before, in Section 3.3.3.

The deviating results of test group 5D20 can be attributed to the different behaviour of SFRC in 3PBTs and DTTs. As the model is derived from the results of Figure 3.4, the same trend is observed. In the 3PBTs, the stresses increase with an increasing CMOD. During flexural tests, the influence of the failure of a single fibre is less pronounced than in a DTT due to the better redistribution of the stresses inside the cracked section.

4.2.5 Sensitivity study

This sensitivity study determines the influence of different parameters used in the model. The current model shows good results (error = 1.24%) for an average calculation time of only 72 s. This section performs some alterations of the model to observe the change in error and time, and check whether the model can improve without sacrificing too much time.

Table 4.2: Sensitivity study of the monotonic model.

		Δ error [%]	Δ time [%]
m	$125 \rightarrow 250$	-4.32	+55.26
	$125 \rightarrow 25$	+1.03	-44.93
N	$50 \rightarrow 100$	+3.01	+80.39
	$50 \rightarrow 20$	+19.15	-60.15
loops	$3 \rightarrow 6$	-27.18	+72.05
	$3 \rightarrow 2$	+60.36	-44.85
ppp	$6 \rightarrow 7$	+7.40	+5.81
	$6 \rightarrow 5$	+34.14	-25.01
ΔH	$1 \rightarrow 0.1\ N$	-2.11	-2.99
	$1 \rightarrow 10\ N$	-1.05	-18.87
Change vertical position first		-2.28	+22.98
Ranges change for every loop		+11.46	+45.03
Change constitutive law		+6.42	-8.45

First the parameters m, N, *loops*, the amount of post-peak points and the criterion for ΔH are investigated. The accuracy is increased and decreased for all five parameters to observe the response of the model, summarised in Table 4.2. Changing the discretisation of the section from $m = 125$ to $m = 250$ only slightly improves the result, but the calculation time is increased with around 46 seconds. When m is decreased, the influence on the error is again small, but the calculation time decreases significantly. This result could be expected because the error ΔM is not influenced by m. The algorithm will find the optimal σ-w curve for a certain m. To make

the model accurate enough, a discretisation of 125 layers is chosen. This way the deformation and stress profile are more exact, but the calculation time remains reasonable.

When the discretisation of the ranges is increased from $N = 50$ to $N = 100$, no big change in error is observed. However, taking an even smaller N does have a significant effect on the error. When N decreases, the correct σ-w curve cannot be approached as accurate as before. This indicates that the discretisation of the ranges has an important influence on the error. However, at around $N = 50$ the effect becomes negligible. Figure 4.16 shows the stagnation of the effect of N.

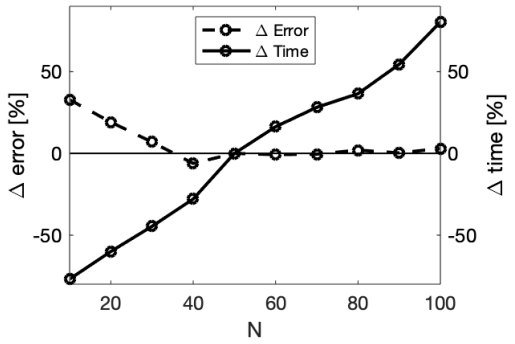

Figure 4.16: Error and time difference for different values of N.

The effect of the amount of loops is the largest. This value indicates the amount of times every point on the constitutive law changes its position. Increasing the loops, decreases the error. But of course, also the calculation time increases for more loops. Changing the amount of loops from 3 to 6 decreases the average error with 27%, but increases the calculation time with one minute. Lowering the amount of loops to 2 results in an error that is 60% larger. For every loop, the position of each point takes into account the new constitutive law, which causes this increase in error. The more loops, the more accurate the result. However, the algorithm will reach a certain limit after which the increase of the amount of loops will not have a significant influence on the error anymore (Figure 4.17).

Next, the amount of post-peak points (*ppp*) in the constitutive law is increased from 6 to 7 and afterwards decreased to 5. A similar conclusion can be made as with the parameters N and *loops*, the higher the parameter, the more accurate the result. However, the decrease in error will again fade as the number of ppp becomes higher. For this case, the limit is reached at around $ppp = 6$, as shown in Figure 4.18.

Finally, the horizontal equilibrium is currently fulfilled when ΔH is lower than $1\,N$. Decreasing this value to $0.1N$ does not have a significant effect on the time or error. The same can be said about increasing this value. The error does not depend on the threshold of the horizontal equilibrium. However, the most accurate result is found when both the horizontal and momentum equilibrium are fulfilled. Therefore, ΔH is kept at the value of $1\,N$.

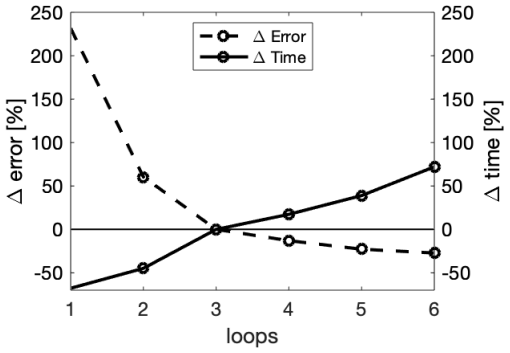

Figure 4.17: Error and time difference for different values of *loops*.

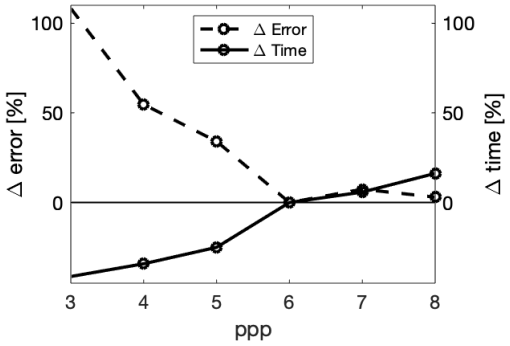

Figure 4.18: Error and time difference for different values of *ppp*.

The parameters used in the sectional analysis show good results for a reasonable calculation time. A summary of all effects is given in Table 4.2, where the difference in error and time are averaged over all four test groups. Parameters N, *loops* and *ppp* determine the amount of constitutive laws checked to find the lowest error. Therefore, the total amount of iterations equals $N \times loops \times ppp \times 2 = 2400$.

Afterwards, also some other characteristics of the model are adjusted. The current model changes the horizontal position of the points of the constitutive law first, and later the vertical position follows. Reversing the order does not improve the error. This small influence on the error is expected because multiple loops are made, cancelling out the effect of the order.

Another alteration concerns the ranges of the points of the constitutive law. Currently these ranges are determined before the iterations start. However, the ranges could also be programmed to change after every loop. These new ranges are then based on the new position of the point, where the error was smallest. Both time and error increase by applying this change to the model.

To conclude, a comparison is made between two different constitutive laws in compression. Currently, the Thorenfeldt curve is used, as shown in Figure 4.3. The same model is now executed with a bilinear curve proposed in Eurocode 2 [27]. The curve remains linear until a strain of 1.75‰, which resembles a crack width of $0.22\,mm$. The ultimate strain equals 3.75‰, the crack width is then $0.44\,mm$. The compressive strength is $f_{ck} = 40\,MPa$, as determined by the concrete class C40/50. Although Figure 4.19 shows a big difference between both curves, the change in error is not that large. The crack width never reaches the peak strength of the material, so the post-peak behaviour in compression does not have an impact on the results. However, the obtained evolution of the neutral axis with the Thorenfeldt curve behaves more similar to the measured values obtained from the LVDTs (Figure 4.20). The real behaviour of the concrete is thus more similar to the Thorenfeldt curve, which is why this constitutive law is chosen.

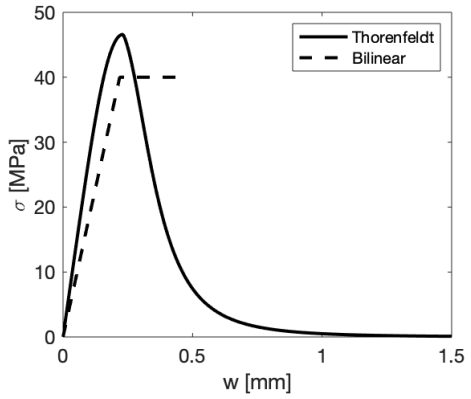

Figure 4.19: Bilinear constitutive law in compression compared to the Thorenfeldt curve.

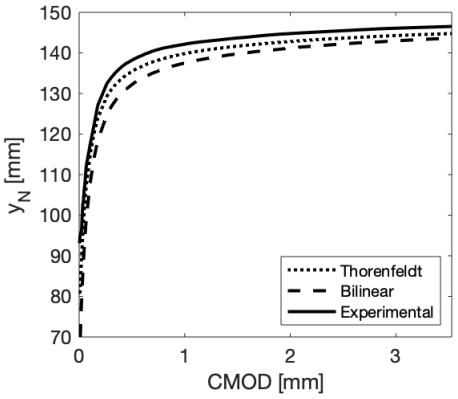

Figure 4.20: Neutral axis evolution of test group 3D20 for the bilinear constitutive law and Thorenfeldt curve.

4.3 Cyclic bending

In the previous section, the monotonic tensile behaviour is predicted by applying sectional analysis to the notched section and demanding a horizontal and bending equilibrium. However, the goal of this thesis is to predict the cyclic behaviour of SFRC. Joining the results of the monotonic model and the experimental results, a cyclic model is presented. This model predicts unloading and reloading curves, starting from the results of the previous monotonic model. The modelled σ-CMOD curves, which are similar to the experimentally obtained σ-CMOD curves, are the starting point for each individual cycle.

First, the damage curves are discussed in Section 4.3.1, derived from the cyclic DTTs. Secondly, a model is proposed to find the unloading curves of bending tests in Section 4.3.2. Afterwards, Section 4.3.3 expands the model and adds reloading of the specimen as well. Section 4.3.4 then compares the results of the unloading and reloading model to the experimental tests. A sensitivity study is executed to optimise the parameters of the model in Section 4.3.5. After the model is finished, a possible application is discussed in Section 4.3.6 which indicates the practicality of the created model.

4.3.1 Damage curves

The loss of stiffness during cyclic loading of SFRC can be described by damage curves. These curves are determined in two separate ways. The stiffness can either be derived from the experimental results of the DTTs, or by using the linear relation between the crack opening at unloading and the plastic deformation (Equation 3.7), both extensively explained in Section 3.3.3. The two methods are implemented in the model, to observe the difference in results. However, the second option has a great advantage compared to the first one. If the plastic deformation is determined

as a function of the unloading deformation, no new DTTs need to be performed in future research to obtain the damage curves. The monotonic bending behaviour is able to predict the envelope curves of the cyclic DTTs. Further, using w_{pl} and the constitutive laws, the damage curves can be composed for every test group. This constitutive law can either be equal to the experimental σ-w curves, or the modelled ones. The latter means that the damage curves only depend on the monotonic bending tests. However, both options are investigated in this section, to compare with the experimental cyclic DTTs.

The damage functions according to the plastic deformation are compared to the mean experimental curves in Figure 4.21. It should be noted that the measured crack width in the tensile tests is transformed to the crack width in a 3PBT by Equation 4.12. By transforming w, the damage curves can be used in the sectional analysis, which utilises measurements of the 3PBTs. However, the influence of this transformation is small because the elastic deformations are really small compared to the plastic deformations.

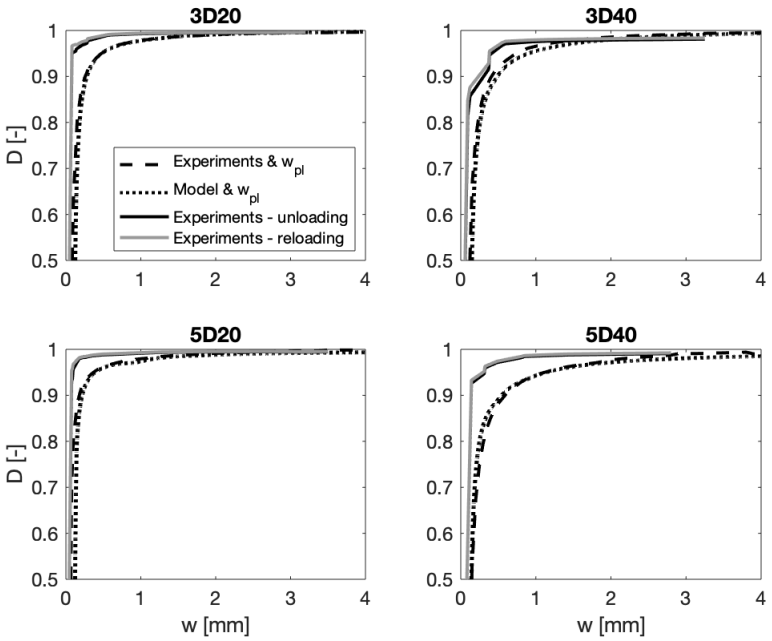

Figure 4.21: Mean unloading and reloading damage functions for DTTs, compared to the plastic deformation method.

The first two curves in Figure 4.21 show the damage curves obtained by using the linear relation between the plastic deformation and unloading deformation (Equation 3.7). The first curve utilises the experimentally obtained monotonic direct tensile curve and the second curve uses the results of the monotonic model to predict the constitutive law. Both curves are hardly distinguishable. However, the modelled monotonic DTTs only need results of a monotonic 3PBT to compose the damage

curves, which is a great advantage. The fact that unloading and reloading curves cannot be composed separately is expected to be negligible due to the similarity of the two last curves, representing the experimental damage curves. As these damages are almost identical, no large influence is expected. Due to the convenience of using the modelled constitutive law, the option using the experimental monotonic DTTs is not further discussed. The two remaining methods are further identified as the "Experimental" and "Model" option.

4.3.2 Unloading

The overview describing the model which determines the unloading curve during a cyclic bending tests, is given in Figure 4.22. The next paragraphs elaborate the figure in more detail.

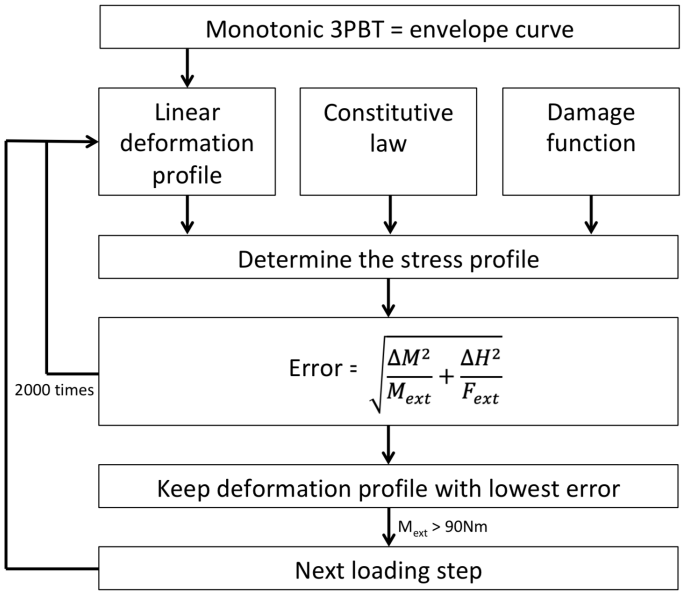

Figure 4.22: Schematic overview of the model for cyclic bending during unloading.

Deformation profile

The unloading algorithm tries to find the deformation profile that satisfies the horizontal and bending equilibrium the most. This deformation profile is a linear curve, assuming an Euler-Bernoulli beam. Section 3.2.2 confirms that this assumption is valid. Therefore, two points can describe the whole deformation profile in the notched section. The two points defining this profile in the proposed model are the CMOD with coordinates (CMOD, $-20\,mm$) and the upper most fibre of the beam (δ_{top}, $150\,mm$). The CMOD at every loading step of the unloading path, is restricted by two boundaries, defined as follows:

$$CMOD_i \in [0; CMOD_{i-1}] \tag{4.13}$$

The upper limit is equal to the CMOD at the previous step, where the external bending moment is larger and therefore the crack width is larger as well. This condition forces the CMOD to decrease while the external force decreases. The CMOD is bounded by 0 as well, as the lower fibres of the beam are not expected to be compressed. The limits of the top of the section, at a height of $y = 150\,mm$, are:

$$\delta_{top,i} \in [\delta_{top,i-1}; 0] \tag{4.14}$$

This value remains negative, as the upper fibre never experiences tension. The limit $\delta_{top,i-1}$ describes the deformation of the upper fibre at the previous loading step. The deformation decreases as the external loading decreases. The boundaries of both Equation 4.13 and 4.14 are only imposed to reduce the calculation time. Expanding the limits results in a similar output of the model, but with an increased calculation time and/or reduced accuracy. Even more narrow intervals for both the $CMOD_i$ and $\delta_{top,i}$ are determined in Section 4.3.5.

The two points describing the deformation profile both vary between the intervals of Equations 4.13 and 4.14. The point at $y = -20\,mm$ changes N_{CMOD} times and the interval at the top fibre is divided in N_{top} crack widths. Therefore, a total of $N_{CMOD} \times N_{top}$ deformation profiles can be constructed.

It should be noted that when the unloading curve starts, $i = 1$ and Equations 4.13 and 4.14 become invalid. However, the deformation profile of the first unloading point is taken equal to the one obtained in the monotonic model. The sectional analysis of the previous model obtained deformation profiles of the beam during the whole monotonic bending process.

Stress profile

After the deformation profile is determined, the stress profile can be calculated using the damage functions of Section 4.3.1 and the constitutive laws calculated in Section 4.2. The previously determined deformation profile results in a crack width at every height of the section. In the monotonic model, this crack width is immediately correlated to a certain stress, using the constitutive law. During unloading, this same relation cannot be used because of the accumulated damage. The damage is calculated according to the highest crack width the section has endured before unloading, and can be derived from Figure 4.21. This figure shows three different options to implement the damage into the model. These are all compared later on in this chapter.

Unloading of a layer of the section occurs when the crack width decreases as well as the external force applied to the specimen. When the specimen is unloaded, a certain irreversible plastic deformation remains present even when no external force is applied. This plastic deformation is calculated with the damage curves. The stiffness with which the specimen unloads, is calculated as follows:

$$K_i = (1 - D) \cdot K_0 \tag{4.15}$$

The stiffness of the uncracked specimen (K_0) is determined using the tangent modulus of elasticity (Equation 3.9) and the characteristic length $l_{cs} = 125\,mm$. Therefore K_0 equals:

$$K_0 = \frac{E_{ci}}{l_{cs}} = \frac{35.91\,GPa}{125\,mm} = 287.2\,\frac{MPa}{mm} \tag{4.16}$$

An example of an unloading curve is shown in Figure 4.23. This curve starts at the constitutive law, and has a slope equal to K_i. Figure 4.23 shows that when the unloading curve reaches $\sigma = 0\,MPa$, the stresses becomes 0 instead of compressive stresses. However, due to the fibres present in the section, some compressive stresses can occur for positive crack widths. The fibres resist the closing of the cracks due to several phenomena: when the fibres have reached an irreversible strain, they are pulled out of the concrete, or get broken. This effect is neglected in the model. The algorithm assumes no resistance of the fibres when unloading.

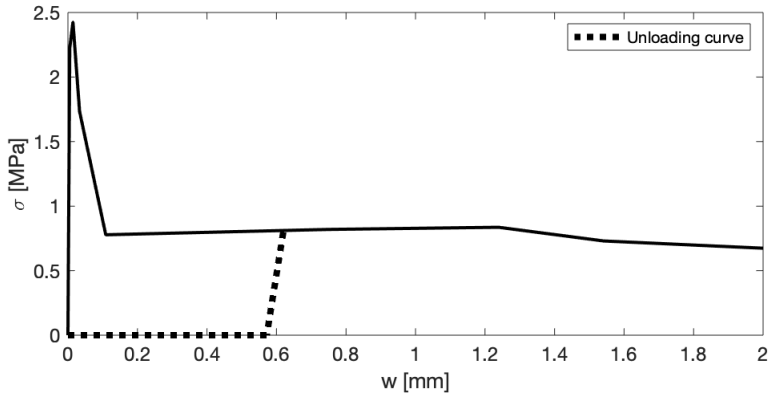

Figure 4.23: σ-w with unloading for test group 3D20.

While the test specimen is unloaded, certain elements of the section may reload. This is counter-intuitive, but it occasionally occurs at layers around the neutral axis. Even though the deformations at the top (δ_{top}) and at the bottom (CMOD) decrease monotonically, it does not necessarily imply that the deformation of every layer will monotonically decrease. This is caused by the fact that the height of the neutral axis evolves. In this model, the assumption is made that the reloading happens with the same stiffness as the unloading stiffness (K_{ul}). This assumption can be made because Figure 4.21 shows that both the unloading and reloading damage curves are similar. Figure 4.23 is therefore also a representation of the local reloading path.

When neither unloading nor reloading occurs in a certain layer, the constitutive law determines the stress belonging to the crack width, as happened for the monotonic model as well. This is the case for crack widths greater than the monotonic crack width, or for compressed layers. The first option only occurs for small crack widths

around the neutral axis. The latter option assumes no effect of damage in the compressed zone of the section. As the crack width never reaches the plastic zone of the Thorenfeldt curve, this assumption is valid.

Error

The algorithm starts at the monotonic σ-$CMOD$ curve, at a certain unloading point. Then, for N_M different unloading steps, the optimal deformation profile can be found, composed of a CMOD and the deformation at the top of the section (δ_{top}). The algorithm calculates the result for a multitude of deformation profiles, all between the borders of Equations 4.13 and 4.14. Instead of calculating the error for a large number of CMODs, the algorithm decreases the search area every time a minimal error is found. Therefore, $N_{CMOD} \times N_{top}$ deformation profiles will be composed for N_{loop} loops. From all $N_{CMOD} \times N_{top} \times N_{loops}$ deformation profiles, the one with the smallest error is kept. This error is determined by Equations 4.17, 4.18 and 4.19.

$$Error_i = \sqrt{\left(\frac{\Delta H_i}{F_{ext,i}}\right)^2 + \left(\frac{\Delta M_i}{M_{ext,i}}\right)^2} \tag{4.17}$$

$$\Delta H_i = b \cdot \sum_{j}^{m} (\sigma_j \cdot h_j) \tag{4.18}$$

$$\Delta M_i = |M_{int,i} - M_{ext,i}| = |b \cdot \sum_{j}^{m} (y_j \cdot \sigma_{j,i} \cdot h_j) - M_{ext,i}| \tag{4.19}$$

The error indicates the deviation of the horizontal equilibrium and moment equilibrium, similar to Equations 4.8 and 4.9 from the monotonic algorithm. However, the cyclic algorithm adds both normalised deviations to indicate the total error of the model.

When the error is minimised, the optimal deformation and stress profile is found and the algorithm can move on the next unloading step until the external bending moment is small enough. The amount of loading steps in one unloading cycle equals N_M. The lower boundary of the external force is taken equal to $0.7\,kN$, associated with a bending moment of $90\,Nm$, and similar to the experimental results. M_{ext} does not reach zero, as the deformation of the section will then always become zero as well. This is a deviation of the reality, due to the fact that the resistance of the fibres is not modelled. The results of the model are discussed in Section 4.3.4.

4.3.3 Reloading

After the unloading of the specimen, reloading starts to complete the whole cyclic behaviour. The reloading curves are described in this section. The algorithm is similar to the algorithm of the unloading path, as shown in the overview of Figure 4.24. The overview is very similar to the overview of unloading. However, the start and ending of both algorithms are different.

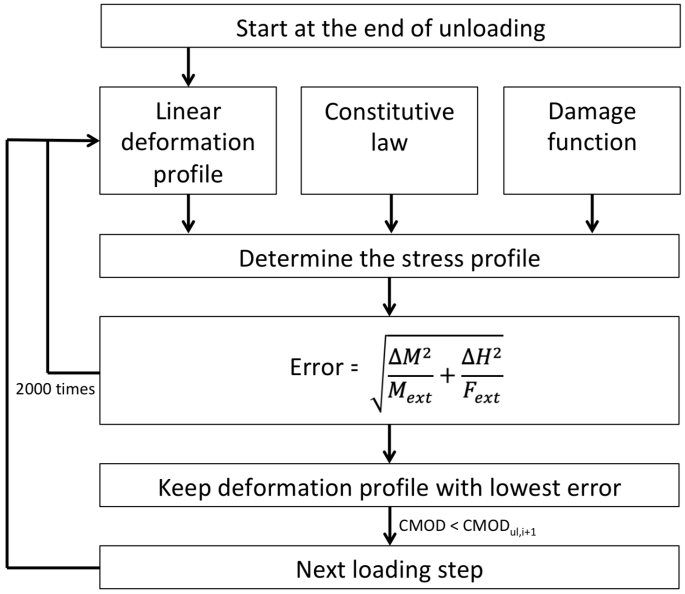

Figure 4.24: Schematic overview of the model for cyclic bending during reloading.

Deformation profile

The deformation profile is again composed of two points, due to the Euler-Bernoulli assumption. The bottom point is equal to the CMOD, at a height of $-20\,mm$. The upper point is defined at a height of $150\,mm$, which indicates the upper fibre of the specimen. The crack widths at both heights are restricted by the following intervals:

$$CMOD_i \in [CMOD_{i-1}; \min(3 \cdot CMOD_{i-1}, CMOD_{i-1} + 0.8\,mm)] \tag{4.20}$$

$$\delta_{top,i} \in [\max(3 \cdot \delta_{top,i-1}, \delta_{top,i-1} - 0.07\,mm); \delta_{top,i-1}] \tag{4.21}$$

The CMOD must be larger then the CMOD at the previous loading step. The CMOD therefore increases with an increasing external load. However, it is also restricted by an upper limit. Section 4.3.5 explains why this exact boundary is chosen. The smaller the interval of both points, the higher the accuracy. The limit can also be chosen at a higher value, but the σ-w curves will be similar although the accuracy would be worse. Additionally, when the CMOD becomes larger than the CMOD at the next unloading point, the reloading curve is stopped and a next cycle starts. Next, the deformation of the upper point of the section can never exceed the lower limit. However, it is always greater than the deformation at the previous loading step. The crack width increases when the external load becomes larger.

The model operates in the same way as the unloading algorithm. A multitude of deformation profiles is composed in between the boundaries of Equations 4.20 and 4.21. The intervals of the CMOD and δ_{top} are respectively divided into N_{CMOD} and N_{top} values. It should also be noted that the first reloading point is chosen equal to

the end of unloading. Therefore, the first deformation and stress profile is already determined during unloading. A continuous progression of both profiles through one cycle is expected.

Stress profile

When the deformation profile is determined, the stress profile can be calculated. This profile depends on the constitutive law and the deformation profile, as well as the damage curve. To determine the damage induced in the specimen at a certain height of the section, the history of that layer needs to be known. The highest crack width this section ever endured, determines the damage and therefore the stiffness during reloading. The damage is calculated using the functions of Figure 4.21, depending on this maximal crack width.

A certain layer of the section can either reload or unload. Most layers will reload, as the crack width becomes higher. The stress can then be determined using the stiffness, which is the slope of the reloading curve. Figure 4.25 shows a reloading path. However, when the reloading curve reaches the constitutive law, the stress is calculated using this constitutive law obtained in Section 4.2.

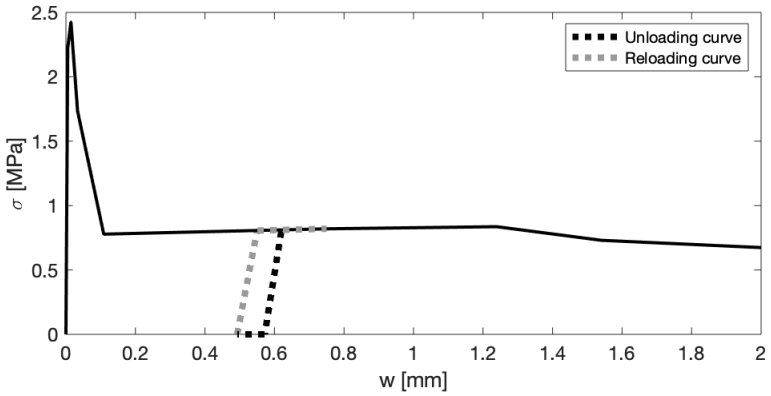

Figure 4.25: σ-w with unloading and reloading for test group 3D20.

The layers at a height close to the neutral axis, can locally show an unloading behaviour as the neutral axis does not remain at the same height throughout the cycle. Unloading of the layers occurs with the same stiffness as reloading. Additionally, for layers experiencing compression, the constitutive law determines the stress.

In the next loading step, M_{ext} increases with a certain unloading step, and the same scheme is followed to achieve a new deformation and stress profile. The unloading step is determined in Section 4.3.5.

Error

Reloading starts at the end of unloading. Therefore the first deformation and stress profile can be determined on beforehand. However, after every loading step, the external bending moment increases and the deformation profile with the lowest error can be found, bounded by Equations 4.20 and 4.21.

During reloading, the error is determined in the same way as for unloading. Equations 4.17, 4.18 and 4.19 show the deviation of a perfect equilibrium for every loading step. When the deformation profile with the lowest error is found, the algorithm moves on to the next loading step until the CMOD of the next unloading cycle is reached.

4.3.4 Results and discussion

σ-CMOD curves

Comparison between the modelled and experimental damage As mentioned before, the algorithm can be executed for multiple damage curves. The first option makes use of the experimental cyclic DTTs. In the second option, the damage is calculated by using the linear relation between w_{pl} and w_{unl} shown in Figure 3.17. Together with the modelled constitutive laws of Section 4.2, the damage is obtained. Figure 4.21 shows the damage curves of both options. The results of the damage curves are compared in Figures 4.26 and 4.27 for the 3D and 5D fibres respectively. More detailed figures of the first five cycles, are shown in Figure 4.32 and discussed later on.

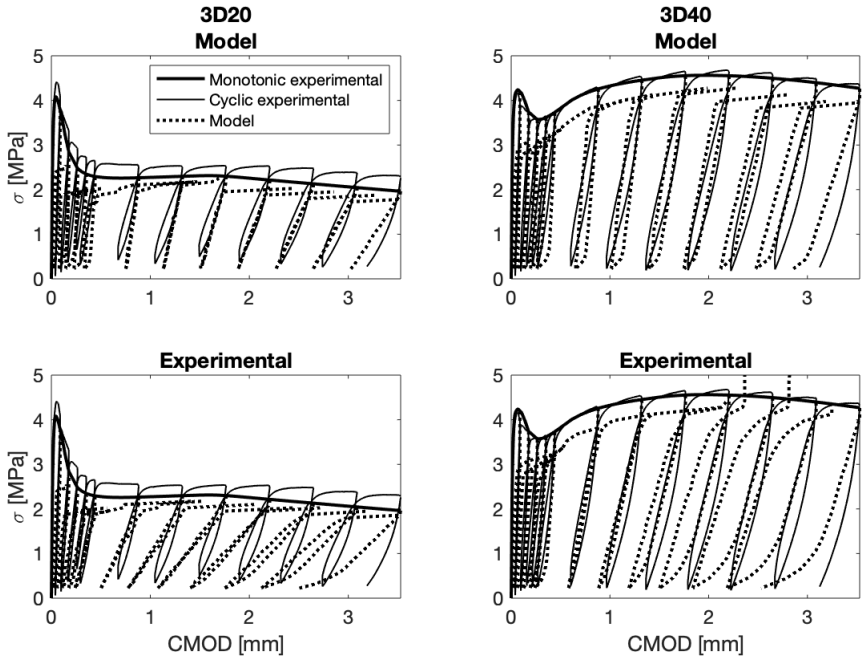

Figure 4.26: Cyclic results for 3D fibres.

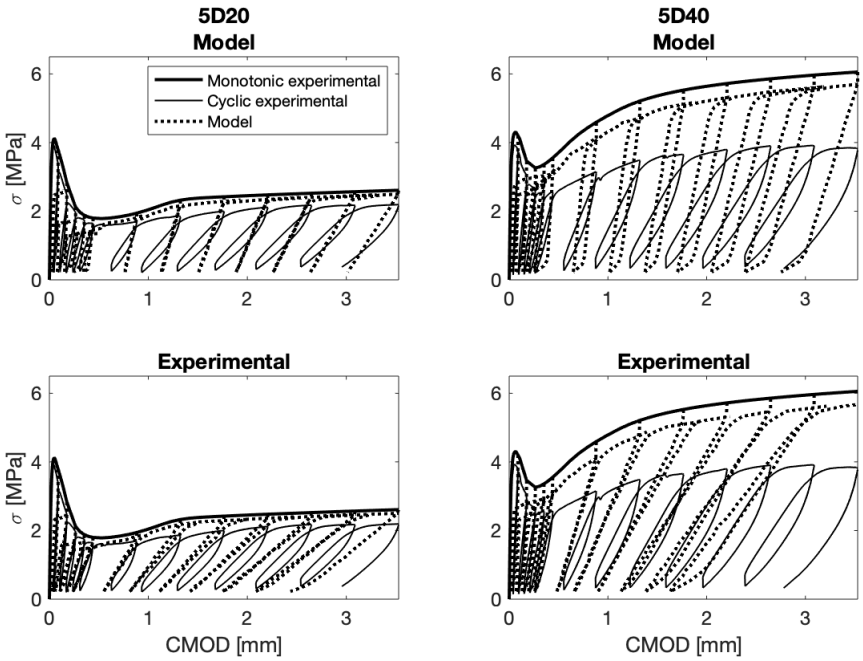

Figure 4.27: Cyclic unloading results for 5D fibres.

The first curves are composed using the monotonic model and linear relation. As stated before, only monotonic 3PBTs are needed to obtain the damage in the specimen. Hence, this method matches the experimental results of the 3PBT well, taking into account the little input needed.

Figure 4.28 shows the differences in tensile post-peak behaviour for the cyclic DTTs and monotonic model. This figure explains some of the deviations in Figures 4.26 and 4.27. The 3D20 test group shows a lower cyclic envelope curve. Therefore, the damage obtained by the cyclic experimental DTTs is larger then the damage obtained with the linear fit of w_{pl}. Because the cyclic DTTs are highly dependant on the fibre distribution, the experimental results are less reliable than the modelled results.

Next, the 3D40 specimens show similar results for both methods. Figure 4.28 illustrates the good agreement between the modelled and experimental post-peak behaviour. The biggest difference between both cyclic curves are the deflections of the unloading path at low stresses. This effect is caused by the resistance of fibres during closing of the crack and will be discussed later on.

For the 5D20 test group, the stiffness obtained with the linear relation between w_{pl} and w_{unl}, is too large compared to the experimental results. This is mainly explained by Figure 3.17. The plastic deformations of test group 5D20 are generally smaller than for the other groups, resulting in higher damages. Figure 4.28 does not show large deviations between the experimental and modelled constitutive law.

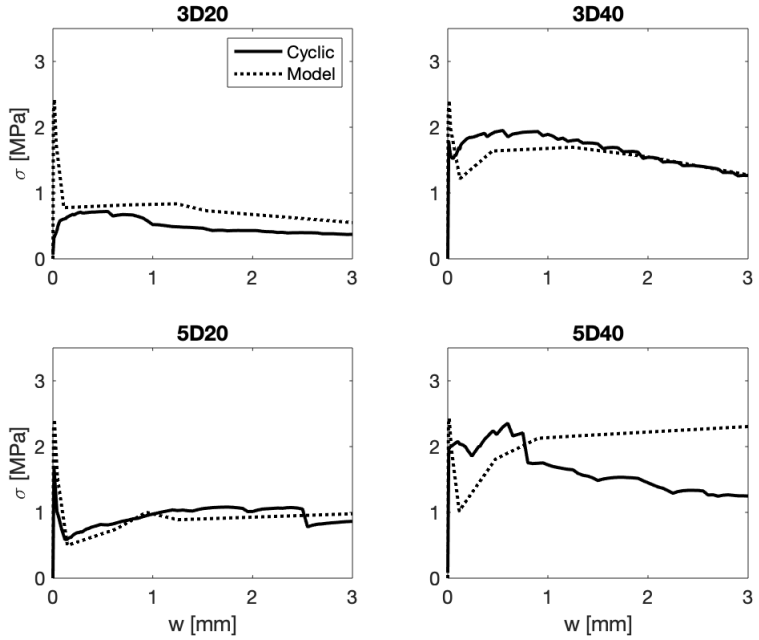

Figure 4.28: Comparison of the envelope of the cyclic DTTs and monotonic model.

Finally, 5D40 test specimens show a large deviation between the modelled and experimental σ-w curve. The lower tensile strength for the experimental results at high crack widths causes an increase in damage for the experimental σ-w curve, as observed in Figure 4.27. Multiple cracking results in decreased tensile stresses. However, the most obvious reason for the deviating result between the cyclic DTTs and modelled results, is the starting curve of the model. Large differences between the monotonic and cyclic 3PBTs are observed.

Using the envelope curve of the cyclic 5D40 tests Because of the large difference between the monotonic and cyclic 3PBTs, the calculations are performed again, when using the envelope curve of the cyclic results instead of the monotonic results. The modelled constitutive law changes as well as the starting curve for the cyclic model.

The new results are shown in Figure 4.29, the modelled damage is too low and the experimentally obtained damage is too large. The difference in cyclic behaviour between the experimental and cyclic curves is thus not only caused by the high monotonic tensile strength. The cyclic curves of the modelled damage are too steep because of the overestimation of w_{pl}. The experimentally obtained damage is too large because of multiple cracking. Even though these curves do show better results, they are not further used in this section. The next changes are implemented on the original curves of Figure 4.27 to be able to observe the exact alterations of a single modification.

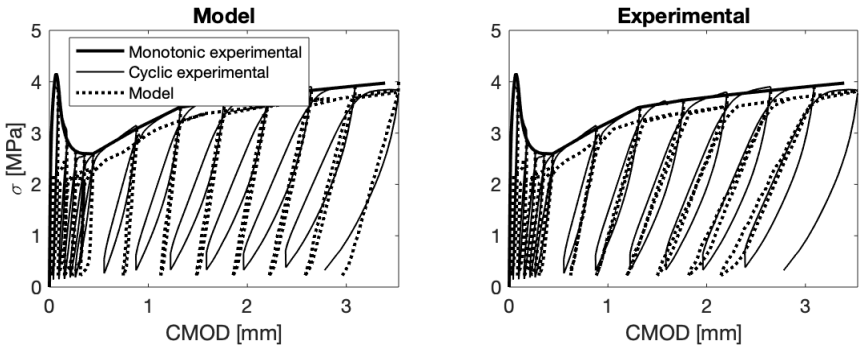

Figure 4.29: Results of the 5D40 test group using the cyclic envelope curve.

Separate relations of w_{pl} for 3D and 5D fibres As mentioned before, the stiffness of the 5D20 and 5D40 test group remains too large during cyclic loading, caused by the relation in Figure 3.17. The main conclusions which can be made when using this linear approach is first of all that the damage is underestimated for low crack widths. This is the case for 3D fibres as well as 5D fibres. Additionally, the damage of 5D fibres is generally underestimated throughout the whole test. Finally, for high crack widths, the damage of 3D fibres is overestimated. These effects are all related to the observations in Figure 3.17. Therefore, it can be said that the model functions as expected, but the input could be improved. Therefore, the linear equations of Figure 3.20 are implemented in the model as well, where a difference is made between the 3D and 5D fibres.

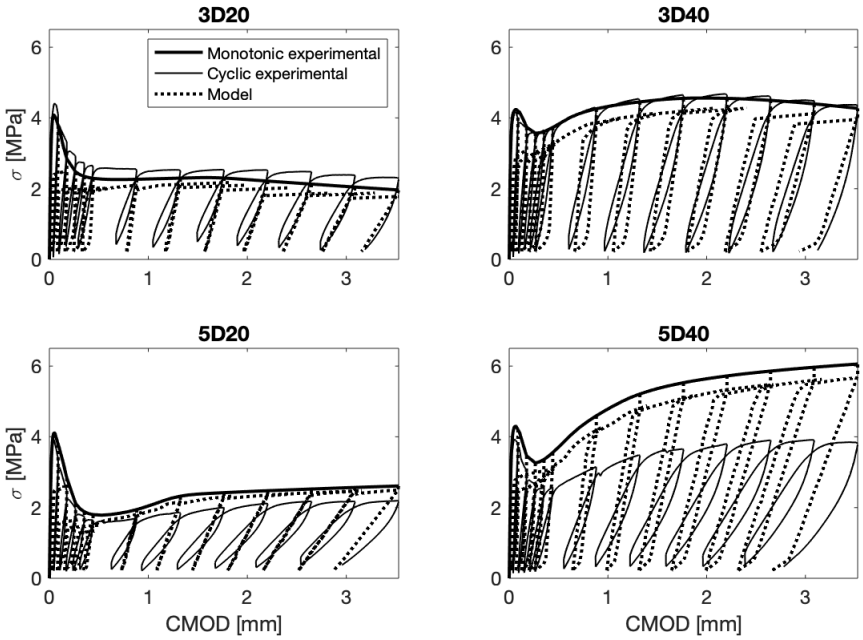

Figure 4.30: Results when separate linear relations are used.

The results now show a better representation of the experiments for high CMODs. However, for lower CMODs the results still deviate. Figure 3.20 illustrates this effect as well, where w_{pl} is overestimated at small crack widths by the linear relations. This implies that, in reality, a single linear relation does not suffice to represent the total post-peak behaviour of SFRC. A bilinear fit could be used to better match the experimental results. The first linear relation then represents the small crack widths (e.g. $w_{unl} \in [0; 0.5\,mm]$) and a second relation contains the larger values (e.g. $w_{unl} \in [0.5; 4\,mm]$).

Influence of the fibres during closing of the crack During the unloading process, the σ-CMOD curves show a deflection at low external forces. This can be attributed to the aforementioned neglected influence of the fibres during unloading. The resistance offered by the fibres can cause compression at positive crack widths. The exact influence of the fibres is not studied in this research, but an estimation is made in Figure 4.31. After reaching the elastic strain of the fibres, the fibres cause compression in the lower zone of the specimen. For the 3D and 5D fibres, these strains are taken equal to 0.8% and 1.1% respectively [10]. The stiffness in the compressed zone of the cracked section is assumed to be equal to the stiffness in the tensile zone. Although this is a rough estimation, the curves in Figure 4.31 clearly show a positive impact. The unloading curves are less prone to deflect towards zero. A new equilibrium is found for larger crack widths. However, the hysteresis behaviour gets lost as the difference between unloading and reloading is now eliminated.

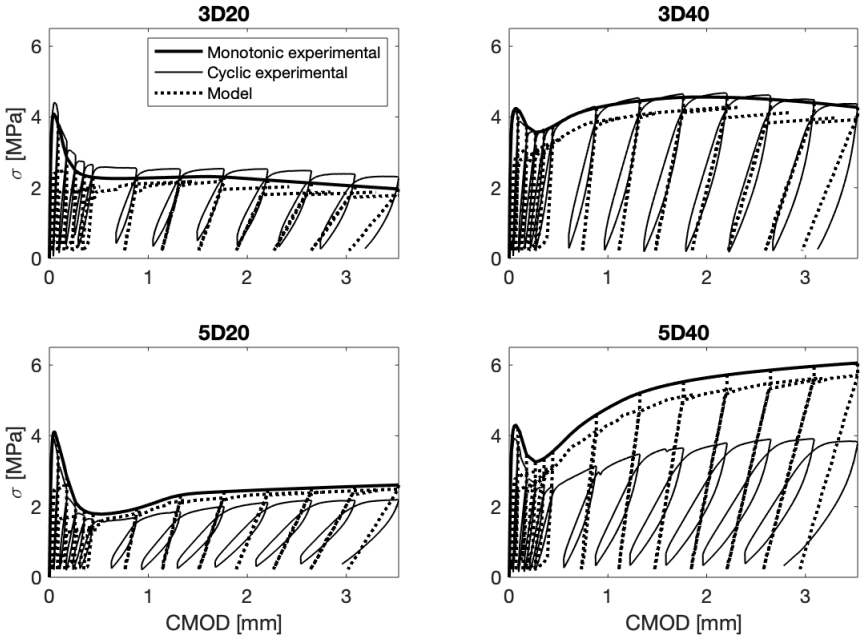

Figure 4.31: Illustration of the influence of fibres during unloading.

Cyclic behaviour at low CMODs A final remark is the decrease of accuracy for low CMODs, as shown in Figure 4.32. The stiffness is generally overestimated at low crack widths. This is observed in Figure 3.17 as well. Additionally, when the external force becomes small, a large deflection is noticed towards 0. This is explained before, by the incomplete implementation of the resistance of the fibres during closing of the crack. Additional research can therefore optimise this behaviour at low CMODs.

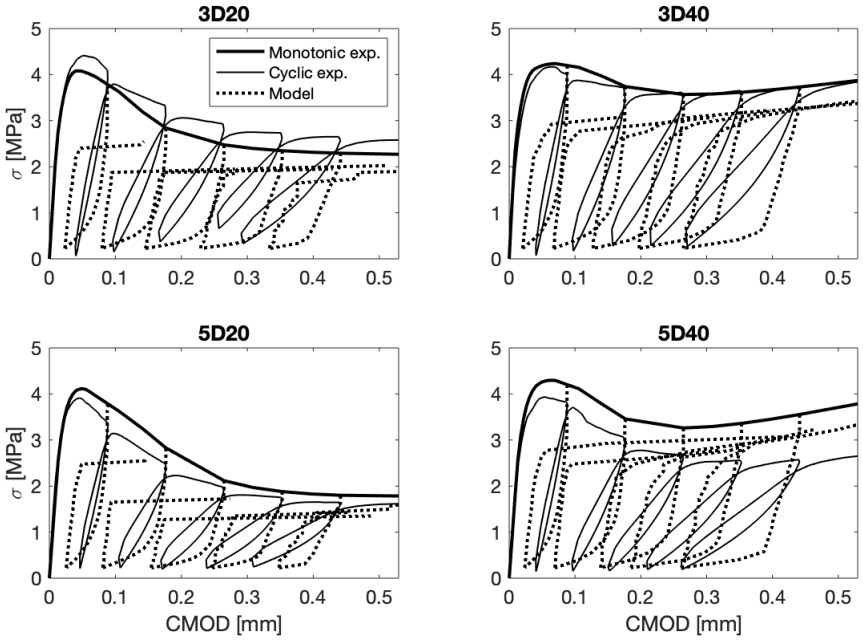

Figure 4.32: Detail of the modelled cyclic behaviour.

Stress profile

The evolution of the stress profile during one cycle is illustrated in Figure 4.34 and the locations at which the stress profile is calculated, are shown in Figure 4.33.

The progression of the stress profile shows the behaviour of SFRC under cyclic loading. During unloading, the stresses in the section decrease. The tensile as well as the compressive stresses are smallest at point C. However, there are still stresses present in the section because the external loading force does not reach 0. Also, the same difference between the test groups can be observed as during the monotonic loading. The higher the fibre volume, the higher the stresses become because more energy can be dissipated. Additionally, 5D40 fibres reach the highest stresses, as observed before. At point D, the tensile peak stress is limited due to the damage induced in the section. For the same crack width, the tensile stresses are lower than calculated by the constitutive law. Finally, when reaching point E, the compressive stresses are highest due to the increased crack width.

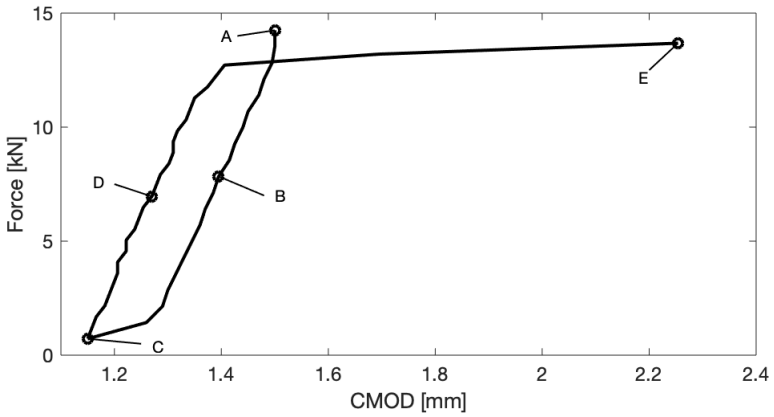

Figure 4.33: Example of the locations where the stress profile is calculated.

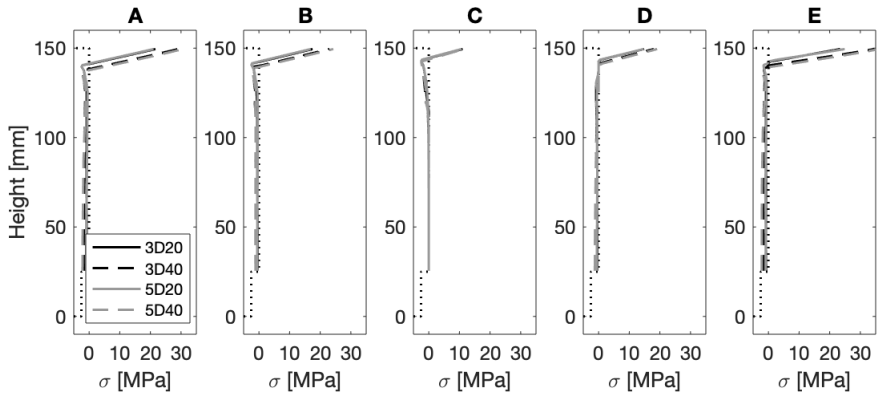

(a) Complete stress profile.

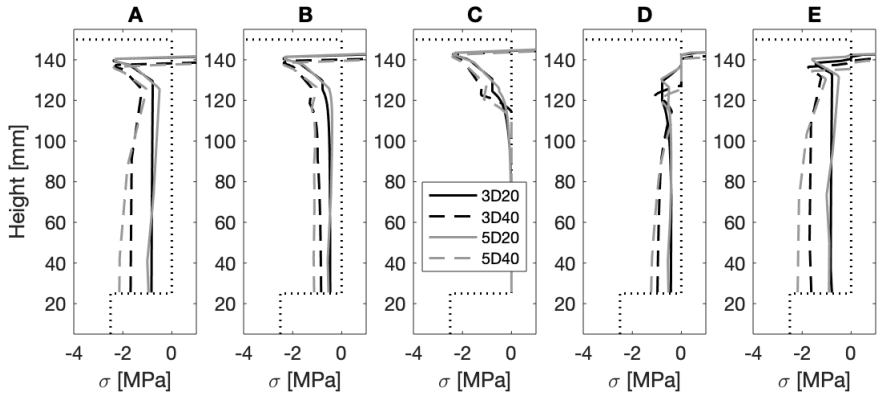

(b) Detail of the tensile stress profile.

Figure 4.34: Stress profiles of all test groups during one cycle starting at $w_{unl} = 1.5\,mm$.

Because the tensile stresses in the notched section are not clear in Figure 4.34a, more detailed curves are shown in Figure 4.34b. As expected, the tensile stresses of the test specimens with 0.50 $V\%$ of fibres are clearly higher. Observing the evolution of the tensile stresses results in several additional conclusions. Profiles A, B and C illustrate the unloading process. The crack widths decrease, and so do the stresses, in accordance with the damage of each layer. As the compression stresses remain fairly high, the section maintains its equilibrium with the high tensile stresses around the neutral axis. To reach these high tensile stresses, the concrete may not be severely damaged. Therefore, an increase in neutral axis is expected during unloading. The following section confirms this statement. The lower the crack widths, the lower the tensile stresses, as is observed in profile C of Figure 4.34b.

After unloading, reloading starts which is indicated by the evolution between profiles C, D and E. During reloading, the compressive stresses increase and so do the tensile stresses. As the crack width increases, the tensile stresses follow, determined by the calculated stiffness. This is observable in the lower part of the cross-section, but the stresses around the neutral axis decreased in profile D. Because the neutral axis now decreases, the concrete around this axis is already damaged and the previous high tensile stresses cannot be reached for small crack widths. However, when the crack width becomes larger than before unloading, the tensile stresses are restored.

Deformation profile

The deformation profiles of all test groups are shown as well in Figure 4.35. From these profiles, it can be concluded that the crack width decreases and increases again during one cycle. However, deviations between the test groups can hardly be made due to the small differences. Therefore the evolution of the neutral axis in the specimens is shown in the following figures as well.

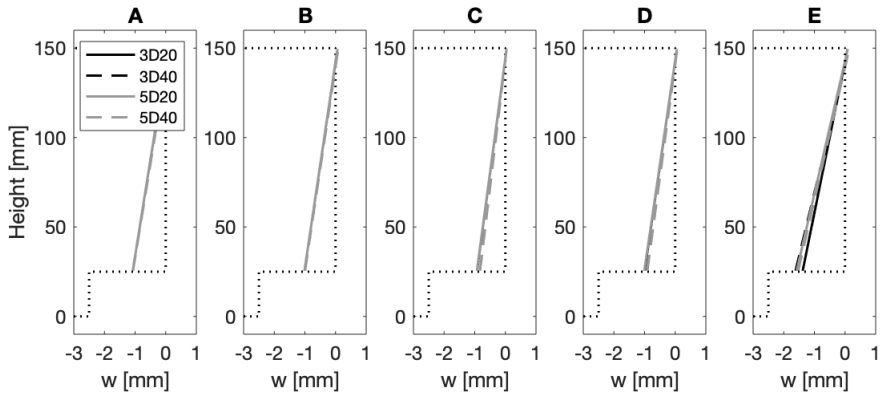

Figure 4.35: Deformation profiles of all test groups during one cycle starting at $w_{unl} = 1.5\,mm$.

In Figure 4.36, the difference between all test groups is shown. The neutral axis of the highest fibre volumes is lower, because the tensile strength is higher. Additionally, the expected increase during unloading and decrease during reloading is observed. This is consistent with the findings of the stress profile.

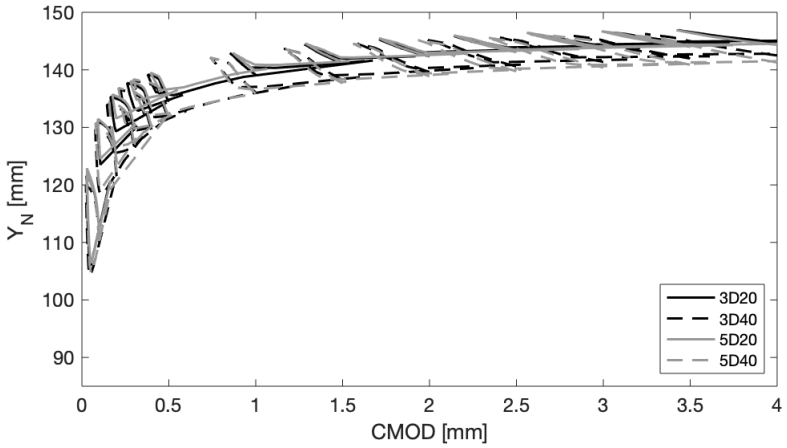

Figure 4.36: Evolution of neutral axis during cyclic loading, obtained from the experimental results.

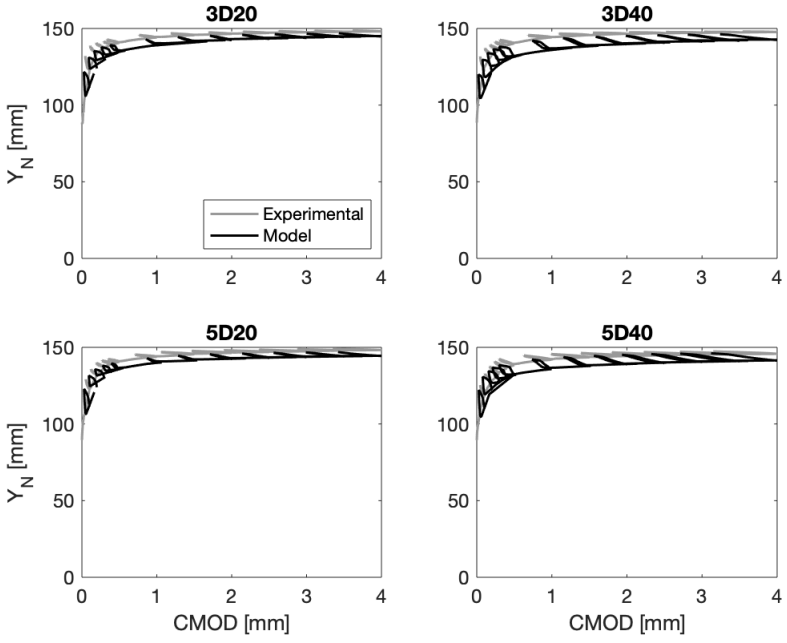

Figure 4.37: Comparison between the experimental and modelled neutral axis during cyclic loading.

Comparing the modelled neutral heights to the LVDT values of the experiments, shows similar trends, indicated in Figure 4.37. However, the modelled neutral axis is lower than the experimental results, which is caused by two effects. First of all, this model is based on the monotonic curves. In Figure 4.13, the model underestimates the neutral axis as well, this trend is continued in the current model. Secondly, the fibres have an influence on the stress profile during cyclic loading. The fibres in the cross-section can cause compressive stresses for positive crack widths. This is not taken into account in the model. Therefore, the tensile stresses need to increase, which causes the neutral axis to move upwards.

Comparison to the DTTs

In the previous discussion, the experimental and modelled results of a 3PBT are compared. However, the method to obtain these results indirectly also develops results for DTTs. The obtained damage curves give an indication on the unloading and reloading curves during a DTT. Therefore, the experimental results are compared to the modelled curves in Figure 4.38. These modelled curves are composed using the separate linear relations of w_{pl} for 3D and 5D fibres.

As expected by Figure 3.20, the damage of low crack widths is underestimated. Therefore, a bilinear relation to obtain w_{pl} is suggested. However, this is not included in the current study.

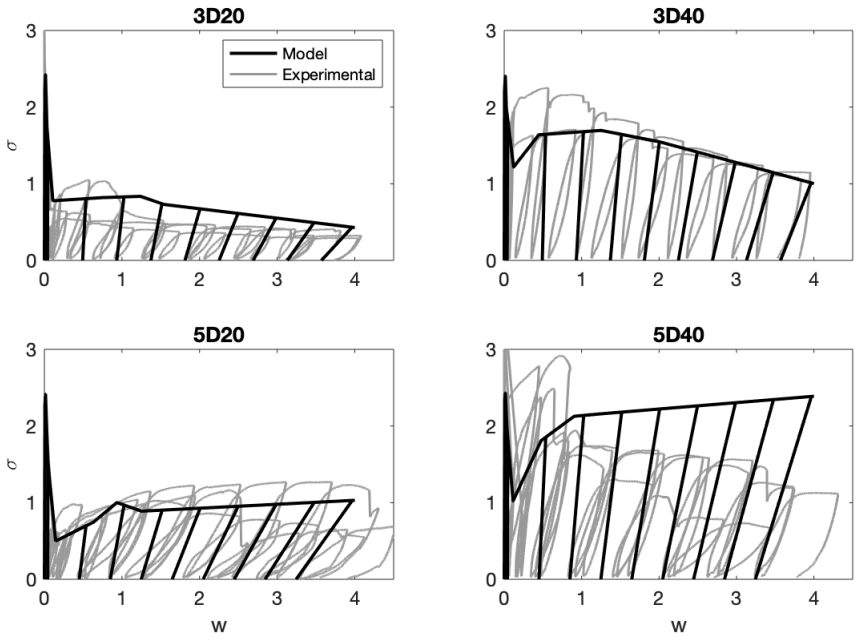

Figure 4.38: Comparison between experimentally obtained σ-w curve and model.

Validation

To validate the model, the cyclic behaviour of every test group is predicted, without starting from the modelled monotonic 3PBT. Previously, every cycle is modelled on its own, starting from the modelled σ-CMOD curves. However, in this section only the first cycle starts from the modelled σ-CMOD curve, all following cycles depart from the end of the previous cycle. The deformation profile of the beginning of every cycle is calculated with the reloading profile of the previous cycle. Figure 4.39 illustrates the results.

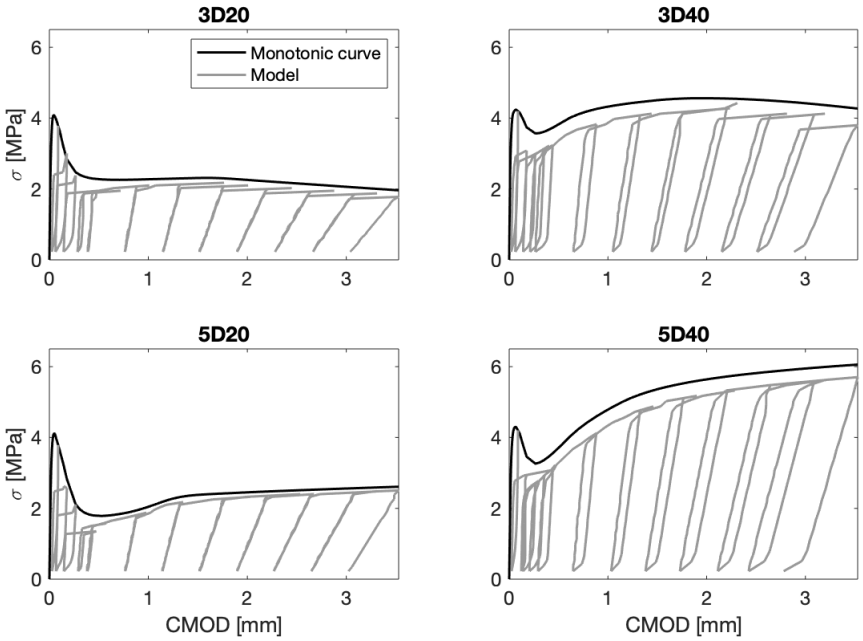

Figure 4.39: Cyclic results without starting from the monotonic curve.

These cyclic curves show that the progression of the cyclic behaviour is independent on the starting point of each cycle. In other words, the end of the reloading path closely represent the monotonic behaviour. The model obtains good results by only using the modelled constitutive law and linear relation of Equation 3.7 as inputs. This verifies the working principle of the model. Steady results are expected when implementing the right input parameters.

4.3.5 Sensitivity study

The model described in the previous sections, where the modelled damage is used and no adaptions are made, has a mean calculation time of 63 s. This is calculated for both unloading (32 s) and reloading (31 s), during all 12 cycles. The corresponding error is equal to 5.16%. This section tries to optimise both the error and calculation time. The error which is defined for the cyclic model is equal to the deviation from

an equilibrium in horizontal forces and bending moments, as determined in Equation 4.17. Therefore, it is not equal to the deviation from the experimental results, as was the case for the monotonic model.

First of all, the values which indicate the borders of the intervals in Equations 4.13 and 4.14 can be optimised. During unloading, both $CMOD_i$ and $\delta_{top,i}$ are bounded by 0 as the lower side of the beam is always in tension, and the upper part compressed. However, these boundaries can be optimised to reach a more accurate result with the same calculation time. For instance the CMOD will never become lower than the CMOD at the previous loading step, minus $0.5\,mm$. For smaller CMODs, this lower boundary can be taken equal to the previous CMOD divided by 2. These limits are obtained from the results of all test groups. Therefore, Equation 4.13 becomes:

$$CMOD_i \in \left[\max\left(CMOD_{i-1} - 0.5\,mm, \frac{CMOD_{i-1}}{2}\right); CMOD_{i-1}\right] \tag{4.22}$$

A similar conclusion is made for the deformation at the top of the specimen. Equation 4.14 now becomes:

$$\delta_{top,i} \in \left[\delta_{top,i-1}; \min\left(\delta_{top,i-1} - 0.04\,mm, \frac{\delta_{top,i-1}}{2}\right)\right] \tag{4.23}$$

Figure 4.40 shows the difference between the previous intervals and the intervals obtained in this section. The difference in σ-$CMOD$ curve is negligible for both methods, as well as the time difference. However, the mean error in the left figure is much higher than the error of the right figure. The mean error over all test groups is now 4.09% and the calculation time $59\,s$. This decrease in error is only attributed to the difference in the unloading path, which evolves from an error of 4.37% to 2.23%. Therefore, the new intervals during unloading are chosen to complete this study. All following alterations are compared to these results. Table 4.3 gives an overview of the difference in error and calculation time.

Table 4.3: Impact of the optimised boundaries.

	Δ error [%]	Δ time [%]
Smaller boundaries	-20.73	-7.22

The boundaries of the deformation profile during reloading are not adapted here as they are already optimised in Section 4.3.3. However, an explanation of Equations 4.20 and 4.21 is given. The boundaries are based on the previous findings during unloading, but applied in the other direction. However, because of the large deflection of the reloading path for high external moments, the borders are slightly increased. This way, it is ensured that the large gain in deformation of the section can be replicated by the model.

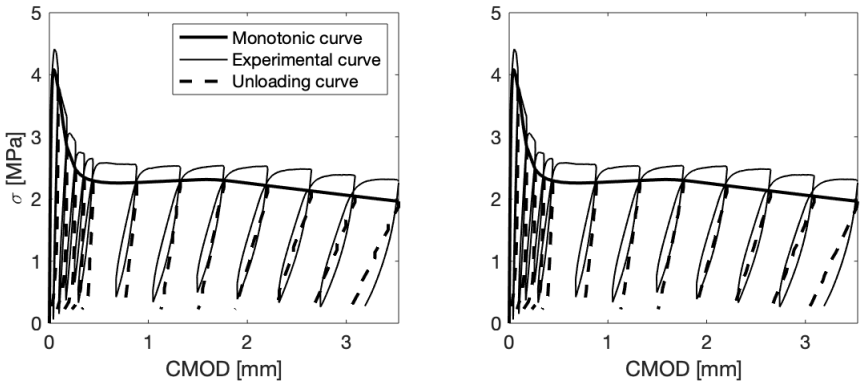

Figure 4.40: Comparison between the interval of Equations 4.13 and 4.14 (left) and Equations 4.22 and 4.23 (right).

Table 4.4 contains an overview of the next changes made to the model. The parameters N_{top}, N_{CMOD} and N_{loops} of the model are determined based on a sensitivity study. It has been decided to make the parameters of both the unloading model and the reloading model equal, to obtain a uniform model. It is assumed that the influence of these parameters is equal during unloading and reloading.

Table 4.4: Sensitivity study of the cyclic model.

		Δ error [%]	Δ time [%]
N_{top}	$100 \rightarrow 144$	-26.77	+45.33
	$100 \rightarrow 49$	+80.41	-44.38
Step size	/2	+2.81	+82.55
	×2	+12.77	-24.50

It is important to notice that both N_{CMOD} and N_{loops} determine the step size of the CMOD value. The amount of deformation profiles which need to be calculated, is equal to $N_{CMOD} \times N_{loops}$, and can be related to the calculation time. Secondly, N_{CMOD}^{Nloops} preferably has the same magnitude as N_{top}, as both values indicate the step-size of the deformation profile. Following equations determine the relation between the three parameters. N_{loops} is taken equal to 2, as a higher number implies the decrease of N_{CMOD}. When N_{CMOD} is too small (< 7), the cyclic behaviour cannot be approached well.

$$N_{loops} = 2 \tag{4.24}$$

$$N_{top} = N_{CMOD}^{N_{loops}} \tag{4.25}$$

In Figure 4.41, the deviation of the error and time compared to the results of $N_{top} = 100$, $N_{CMOD} = 10$ and $N_{loops} = 2$ are shown. These deviations are calculated as the mean value for all test groups. It can be observed that the time increases quasi-linear with the amount of deformation profiles. However, the rate of the

change in error becomes smaller when N_{top} increases. Therefore, it is chosen to use $N_{top} = 100$ as the error deflects around this point. Figure 4.41 shows that this value results in a good trade-off between the time and error during both unloading and reloading. Because Figure 4.41a and 4.41b show similar curves, the assumption that the influence of N_{top} is independent on either the unloading or reloading path, is valid.

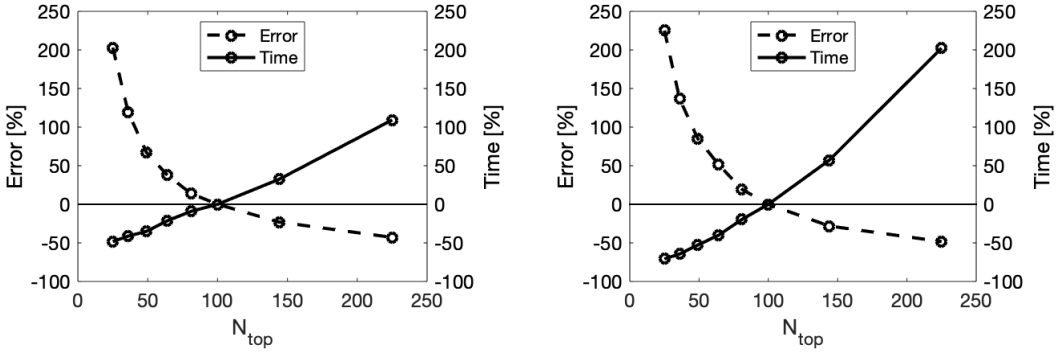

(a) Unloading. (b) Reloading.

Figure 4.41: Error and time difference for different values of N_{top}.

Next to these parameters, also m is determined. Similar to the monotonic model, this parameter indicates the amount of layers in which the notched section is divided. This value is kept equal to 125 so both models are compatible.

Further, the amount of loading steps (N_M) during unloading and the loading step during reloading, need to be determined as well. Even though these parameters do not influence the error, they still need to be accurate to find a smooth cyclic behaviour without sacrificing too much computational time. Therefore, N_M is taken equal to 20, and the step size during reloading is 30 Nm and 60 Nm for specimens with a fibre volume of 0.25V% and 0.50V%, respectively. The difference between step sizes for different fibre volumes is made because of the large difference in post-peak behaviour. A similar amount of loading steps is achieved during unloading and reloading for all test groups with the values mentioned in this paragraph. Table 4.4 shows the influence of the loading steps when they are halved or doubled.

4.3.6 Extension to multiple loading cycles

The model produced in this chapter has already proven to function during progressive cyclic loading. However, it would be a great benefit if this model could also predict the behaviour of SFRC if the loading pattern is bound between two limits. If this is possible, the amount of loading cycles until failure could be determined between constant external forces. Additionally, S-N curves can be composed without executing a multitude of tests.

Two characteristics of the described model make the current sectional approach not ideal for applying constant cyclic loading. First of all, the damage is expected to be 0 before reaching the peak strength. Therefore this new approach cannot start at an undamaged specimen. However, this is solved by applying the model after a crack is formed. In this example, cyclic loading starts at $CMOD_y = 0.5\,mm$. The remaining lifetime can then still be calculated. Secondly, no difference exists between the unloading and reloading curves when using the modelled damage, based on the linear relation between w_{unl} and w_{pl}. Therefore, the upper boundary of the external force should be high enough, so an increase in crack width can be generated. The latter problem is solved by using the experimentally obtained damage curves, which differentiate between unloading and reloading.

Figure 4.42 demonstrates a possible cyclic behaviour between two constant boundaries. As seen in the figure, fatigue occurs in three stages. First, the deformation rapidly increases. Then the CMOD slowly increases for every cycle and the crack propagates. Eventually the crack width suddenly increases up until failure. This fatigue behaviour is expressed by the Paris' law in Section 2.1.4 and Figure 2.9.

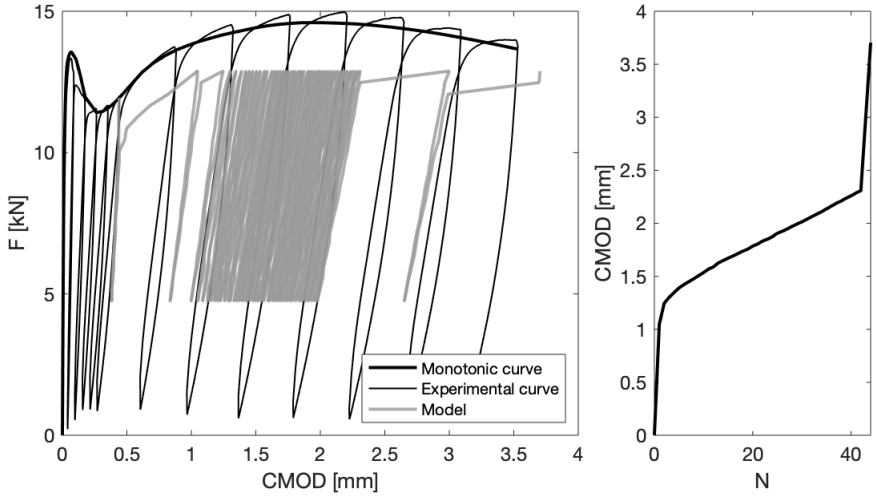

Figure 4.42: Cyclic behaviour of test specimen 3D40 bounded by constant external forces of 35% and 95% of the peak force.

The result of Figure 4.42 shows that test group 3D40 fails after 44 cycles for a stress level of 95% ($N = 44$, $S = 95$). Figure 2.10 (left) shows general S-N curves, derived from different experiments in literature, for plain concrete and SFRC. According to these curves, the modelled result of this study is realistic. The differences in results can be attributed to the different properties of the material. The concrete composition as well as the fibre characteristics differ. Additionally, the modelled loading cycles start after cracking, which shortens the lifetime. However, obtaining the result of Figure 4.42 only takes 2.6 minutes, which is a strong advantage over the experimental testing. This calculation time linearly increases with N.

Although the extension to multiple loading cycles has some drawbacks, the behaviour is consistent with the Paris' law and the model returns realistic values of the remaining lifetime. Therefore, the model is a useful attempt to gain knowledge on the fatigue behaviour. Obtaining the damage evolution before reaching the peak stress, and differentiating between the unloading and reloading damage can still improve the results.

4.4 Conclusion

In this chapter, sectional analysis is applied on the notched section of a concrete prism during three-point bending tests. By dividing this section into several layers, and assuming a uniform deformation in each layer, the stress profile inside the cross-section can be obtained by a constitutive law. Two conditions are imposed to find the right deformation profile. The horizontal as well as the momentum equilibrium need to be fulfilled. When these conditions are met, the correct deformation and stress profile is found.

This method is first used to find the optimal constitutive law, by adapting the post-peak behaviour of the Model Code. Minimising the difference between the experimentally obtained σ-CMOD curve and the modelled one results in a σ-w relation which approaches the DTTs well. The model is also able to make an acceptable estimate of the neutral axis evolution and stress profiles.

Afterwards, a second model is composed to find the cyclic σ-CMOD curves as well. Knowing the damage progress and the monotonic behaviour, the cyclic behaviour can be predicted. After every cycle, the damage increases depending on the test group, and therefore the stiffness of the SFRC decreases. However, it is observed during the experiments that the plastic deformation, equal to the remaining crack width at the end of unloading, is only dependant on the crack width at the beginning of unloading. Therefore, the damage is determined independent on the fibres characteristics and corresponds well to the experimentally obtained damage.

Some interesting results can be obtained from this cyclic model. First of all, the σ-$CMOD$ curves are a good approximation of the experimental ones, without using the experimental DTTs as an input. Additionally, the stress and deformation profiles can be constructed with this model, throughout the entire test. For that reason, new insights in the behaviour of SFRC have been developed. For instance the increase of the neutral axis during unloading is explained by the compressive stresses which remain high during unloading. Also the assumption of a linear deformation profile during flexural loading is proven to be valid.

However, it is concluded that the model has some shortcomings. For instance the relation between w_{pl} and w_{unl}, here assumed to be linear and independent of the fibres, is more dependent on the fibre type than initially expected. A separate relation for 3D and 5D fibres improves the results. Secondly, the influence of the fibres during closure of the crack is not modelled accurately. The model implies that no compressive stresses can be found in the cross-section, when the crack width is

positive. However, the resistance of fibres during unloading could cause compressive stresses. It is confirmed that this effect indeed modifies the final output, but the exact impact of the fibres is not modelled.

Both the monotonic and cyclic model are optimised by performing a sensitivity study. The parameters used in both models are chosen in such a way that the error is acceptable but the computational time is not too large. The final monotonic model can create a σ-w relation in 72 s, with an average deviation of the experimental results of 1.24%. The cyclic model needs a calculation time of 59 s, to obtain an error of 4.09%. The latter error is equal to the deviation from a global equilibrium of the cracked section.

Lastly, an extension to more loading cycles between constant stress levels is made. The result shows fatigue behaviour according to the Paris' law and is in agreement with expectations from the SN-curves from literature. Even though the model is originally developed for progressive loading cycles, with some improvements it can be extended to obtain the lifetime of SFRC.

Chapter 5

Conclusion

The main conclusions of this research are described in this chapter (Section 5.1). The general findings of the cyclic behaviour during experimental tests and sectional modelling are summarised. Section 5.2 includes suggestions for further research, which could not be studied within this thesis.

5.1 Overall conclusion of the study

Steel fibre reinforced concrete is a promising material due to the increase of post-cracking tensile strength. However, a lack of building codes limits the use of SFRC in structural applications. Improved insights are needed to make optimal use of this composite material. This research focuses on its cyclic behaviour, as lots of structures are prone to fatigue failing, caused by repeated loads. Previous research proved that fibres can improve the cyclic behaviour of concrete, which is verified in this study by experimental testing. Additionally, a model is developed to predict this behaviour. The accumulated damage inside the material is a critical input of the model, and therefore analysed in more detail.

The research started by executing different experimental tests, including the monotonic and cyclic loading of four different steel fibre reinforced concrete compositions. Acoustic emission is applied to the test setup to gain supplementary information about the damage evolution. The results of a previous study on three-point bending tests are analysed as well as the output of direct tensile tests, executed within this research. Both tests conclude that the monotonic stress - crack opening curves can be taken equal to the cyclic envelope curves. Also the damage inside the specimen can be derived from these tests. The stiffness during unloading and reloading is related to the degree of damage.

The damage progress is studied by analysing the acoustic emission results as well. Micro-cracks form inside the concrete matrix and propagate until a macro-crack is formed, this is accompanied by reaching the peak load. Afterwards, the stress drops and the amount of AE signals increases. Most signals are then sent by the interaction between the fibres and concrete matrix. These insights have been acquired from

observing the amount of AE events, applying the AF/RA analysis and localising the events. Overall, the detection, localisation and classification of AE signals can be related to the degree of damage inside the specimen.

Next to the experimental tests, two models are developed based on sectional analysis. The first model is able to construct the constitutive law from results of a three-point bending test. These σ-w curves are more easy to interpret. Direct tensile tests can directly obtain this relation, but the complexity of the test setup makes a bending test more convenient. The second model uses these constitutive laws, as well as the damage determined by the experiments, to predict the cyclic behaviour. The model captures the experimental behaviour well, by only using the monotonic three-point bending tests as input, as well as the damage.

It was concluded that the crack width after unloading can be determined independent of the fibre type and volume. This means that the damage can be obtained by only using the constitutive law, as well as the relation determining the crack width after unloading. Therefore, the cyclic behaviour of SFRC can be predicted in the future by only executing monotonic three-point bending tests. As these tests are less complex compared to direct tensile tests, this research strongly proves its value. However, the relation determining the plastic deformation can still be improved, which is elaborated in the next section. The evolution of the stress and deformation profile can now be easily obtained, without being hindered by the unpredictable distribution of steel fibres.

5.2 Suggestions for future work

Some improvements could be added to the proposed model, to optimise the results. Firstly, the input of the model can be improved by executing more tests, mainly monotonic flexural and cyclic tensile tests. The current research is based on only 24 3PBTs and 31 DTTs. As the post-cracking behaviour of SFRC is highly dependant on the amount of fibres inside the cross-section, a larger test group can improve the experimental results. The constitutive laws can be more accurate, and an advanced relation concerning the crack opening after unloading could be developed. Additionally, the current research is limited by only two kinds of fibres, and two volume fractions. Executing tests on more specimens, with different fibre properties, can make the model more robust. Furthermore, the execution of tensile tests measured with LVDTs can improve the results as well. The pre-peak behaviour is now poorly captured by the clip gauges. LVDTs can measure the elastic strains, resulting in improved observations of the damage progress. In the current proposal, the damage before macro-cracking is assumed to be zero. This can either be validated or disputed by LVDT testing.

Secondly, the exact effect of the fibres on the closure of a crack could not yet be defined. Deformed, pulled-out or broken fibres offer a certain resistance when closing a crack. This can possibly result in compressive stresses at positive crack openings. Quantification of this effect can enhance the model. An improved analysis of AE

signals may offer a solution to this problem. A combination of the AF/RA analysis, localisation and evolution of the amount of AE events can provide insight into the distribution of the damage over the cross-section. These results could be linked to the resistance of the fibres during closing of the crack.

Finally, the model can be enhanced by only relating the AE activity to the damage evolution. When this is possible, in situ measurements of AE signals can eventually predict the cyclic behaviour of fibre reinforced concrete structures subjected to repeated loading. Consequently, the improved knowledge on SFRC could increase the use of SFRC and fulfil its potentials.

Bibliography

[1] R. Abbasnia and H. Ziaadiny. Behavior of concrete prisms confined with FRP composites under axial cyclic compression. *Engineering Structures*, 32(3):648–655, 2010.

[2] D. Aggelis. Classification of cracking mode in concrete by acoustic emission parameters. *Mechanics Research Communications*, 38(3):153–157, 2011.

[3] D. Aggelis, D. Soulioti, N. Sapouridis, N. Barkoula, A. Paipetis, and I. Matikas. Acoustic emission characterization of the fracture process in fibre reinforced concrete. *Construction and Building Materials*, 25(11):4126–4131, 2011.

[4] A. Amin and S. Foster. Predicting the flexural response of steel fibre reinforced concrete prisms using a sectional model. *Cement and Concrete Composites*, 67:1–11, 2016.

[5] N. Banthia, C. Zanotti, and M. Sappakittipakorn. Sustainable fiber reinforced concrete for repair applications. *Construction and Building Materials*, 67(C):405–412, 2014.

[6] B. Barragán, R. Gettu, M. Martín, and R. Zerbino. Uniaxial tension test for steel fibre reinforced concrete - a parametric study. *Cement and Concrete Composites*, 25(7):767–777, 2003.

[7] J. Barros and J. Figueiras. Flexural behavior of SFRC: Testing and modeling. *Journal of Materials in Civil Engineering*, 11(4):331–339, 1999.

[8] Bekaert. *Datasheet: 3D 80/60BG.*

[9] Bekaert. *Datasheet: 5D 65/60BG.*

[10] Bekaert. *Reinforcing the future*, 2012. Technical document.

[11] B. Boulekbache, M. Hamrat, M. Chemrouk, and S. Amziane. Flexural behaviour of steel fibre-reinforced concrete under cyclic loading. *Construction and Building Materials*, 126:253–262, 2016.

[12] P. Cachim, J. Figueiras, and P. Pereira. Fatigue behavior of fiber-reinforced concrete in compression. *Cement and Concrete Composites*, 24(2):211–217, 2002.

[13] A. Caratelli, A. Meda, Z. Rinaldi, and P. Romualdi. Structural behaviour of precast tunnel segments in fiber reinforced concrete. *Tunnelling and Underground Space Technology incorporating Trenchless Technology Research*, 26(2):284–291, 2011.

[14] X. Chen, J. Bu, and L. Xu. Effect of strain rate on post-peak cyclic behavior of concrete in direct tension. *Construction and Building Materials*, 124:746–754, 2016.

[15] X. Chen, Y. Huang, C. Chen, J. Lu, and X. Fan. Experimental study and analytical modeling on hysteresis behavior of plain concrete in uniaxial cyclic tension. *International Journal of Fatigue*, 96:261–269, 2017.

[16] X. Chen, L. Xu, and J. Bu. Experimental study and constitutive model on complete stress-strain relations of plain concrete in uniaxial cyclic tension. *KSCE Journal of Civil Engineering*, 21(5):1829–1835, 2017.

[17] M. De Smedt, K. De Wilder, L. Vandewalle, and E. Verstrynge. Acoustic emission-based analysis of damage mechanisms in steel fibre reinforced concrete under monotonic and cyclic loading. *Proceedings of the 10th International Conference on Fracture Mechanics of Concrete and Concrete Structures (FraMCoS-X), Bayonne, France*, pages 1–11, 2019.

[18] M. De Smedt, K. De Wilder, E. Verstrynge, and L. Vandewalle. Monotonic and cyclic pull-out behaviour of 3D and 5D hooked-end steel fibres from a concrete matrix. *Proceedings of the 12th fib International PhD Symposium in Civil Engineering*, pages 43–50, 2018.

[19] M. De Smedt, R. Vrijdaghs, C. Van Steen, E. Verstrynge, and L. Vandewalle. Damage analysis in steel fibre reinforced concrete under monotonic and cyclic bending by means of acoustic emission monitoring. *Cement and Concrete Composites (in review)*, 2020.

[20] X. Destree and J. Mandl. Steel fibre only reinforced concrete in free suspended elevated slabs: Case studies, design assisted by testing route, comparison to the latest SFRC standard documents. *Tailor Made Concrete Structures: New Solutions for Our Society*, pages 437–443, 2008.

[21] M. di Prisco, M. Colombo, and D. Dozio. Fibre - reinforced concrete in fib model code 2010: principles, models and test validation. *Structural Concrete*, 14(4):342–361, 2013.

[22] M. di Prisco, G. Plizzari, and L. Vandewalle. Fibre reinforced concrete: new design perspectives. *Materials and Structures*, 42(9):1261–1281, 2009.

[23] D. Dupont and L. Vandewalle. Distribution of steel fibres in rectangular sections. *Cement and Concrete Composites*, 27(3):391–398, 2005.

[24] G. Etse, A. Caggiano, and S. Vrech. Multiscale failure analysis of fiber reinforced concrete based on a discrete crack model. *International Journal of Fracture*, 178(1-2):131–146, 2012.

[25] European Committee for standardization. *EN 1990: Basis of structural design.* Brussel, 2002.

[26] European Committee for Standardization. *EN 14651: Test method for metallic fibered concrete - measuring the flexural tensile strength (limit of proportionality (LOP), residual).* 2005.

[27] European Committee for standardization. *EN 1992: Design of concrete structures.* Brussel, 2005.

[28] European Committee for Standardization. *EN 12390-3: Testing hardened concrete - Part 3: Compressive strength of test specimens.* 2019.

[29] Fédération international du béton (fib). *fib Model Code for Concrete Structures.* Wilhelm Ernst Sohn, Germany, 2010.

[30] F. Germano, G. Tiberti, and G. Plizzari. Experimental behavior of SFRC columns under uniaxial and biaxial cyclic loads. *Composites Part B*, 85:76–92, 2016.

[31] F. Germano, G. Tiberti, and G. Plizzari. Post-peak fatigue performance of steel fiber reinforced concrete under flexure. *Materials and Structures*, 49(10):4229–4245, 2016.

[32] B. Graybeal and F. Baby. Development of direct tension test method for ultra-high-performance fiber-reinforced concrete. *ACI Materials Journal*, 110(2):177–186, 2013.

[33] C. Grosse and M. Ohtsu. *Acoustic Emission Testing.* Springer, 2008.

[34] V. Guerini, A. Conforti, G. Plizzari, and S. Kawashima. Influence of steel and macro-synthetic fibers on concrete properties. *Fibers*, 6(3):47, 2018.

[35] A. Hillerborg, M. Moder, and P.-E. Petersson. Analysis of crack formation and crack growth in concrete by means of fracture mechanics and finite elements. *Cement and Concrete Research*, 6(6):773–781, 1976.

[36] H. Lambotte, C. Ladang, C. Xhonneux, J. Horemans, P. Magera, and C. Ployaert et al. *Betontechnologie (in Dutch).* Belgische Betongroepering, Brussel, 2015.

[37] S. Lappa. *High Strength Fibre Reinforced Concrete - Static and fatigue behaviour in bending.* Thesis, Delft University of Technology, 2007.

[38] C. Lee and H. Kim. Orientation factor and number of fibers at failure plane in ring-type steel fiber reinforced concrete. *Cement and Concrete Research*, 40(5):810–819, 2010.

[39] J.-H. Lee. Influence of concrete strength combined with fiber content in the residual flexural strengths of fiber reinforced concrete. *Composite Structures*, 168:216–225, 2017.

[40] M. Lee and B. Barr. An overview of the fatigue behaviour of plain and fibre reinforced concrete. *Cement and Concrete Composites*, 26(4):299–305, 2004.

[41] B. Li, Y. Chi, L. Xu, C. Li, and Y. Shi. Cyclic tensile behavior of SFRC: Experimental research and analytical model. *Construction and Building Materials*, 190:1236–1250, 2018.

[42] B. Li, L. Xu, Y. Chi, B. Huang, and C. Li. Experimental investigation on the stress-strain behavior of steel fiber reinforced concrete subjected to uniaxial cyclic compression. *Construction and Building Materials*, 140:109–118, 2017.

[43] V. Li and T. Matsumoto. Fatigue crack growth analysis of fiber reinforced concrete with effect of interfacial bond degradation. *Cement and Concrete Composites*, 20(5):339–351, 1998.

[44] F. Minelli. *Plain and Fiber Reinforced Concrete Beams under Shear Loading: Structural Behavior and Design Aspects*. Thesis, Università di Brescia, 2005.

[45] A. Mudadu, G. Tiberti, F. Germano, G. A. Plizzari, and A. Morbi. The effect of fiber orientation on the post-cracking behavior of steel fiber reinforced concrete under bending and uniaxial tensile tests. *Cement and Concrete Composites*, 93:274–288, 2018.

[46] A. Naaman. Engineered steel fibers with optimal properties for reinforcement of cement composites. *Journal of Advanced Concrete Technology*, 1(3):241–252, 2003.

[47] T. Nguyen-Tat, N. Ranaivomanana, and J.-P. Balayssac. Characterization of damage in concrete beams under bending with Acoustic Emission Technique (AET). *Construction and Building Materials*, 187:487–500, 2018.

[48] M. Noorsuhada. An overview on fatigue damage assessment of reinforced concrete structures with the aid of acoustic emission technique. *Construction and Building Materials*, 112:424–439, 2016.

[49] K. Ohno and M. Ohtsu. Crack classification in concrete based on acoustic emission. *Construction and Building Materials*, 24(12):2339–2346, 2010.

[50] M. Ohtsu et al. Recommendation of RILEM TC 212-ACD: acoustic emission and related NDE techniques for crack detection and damage evaluation in concrete - Measurement method for acoustic emission signals in concrete. *Materials and Structures*, 43(9):1177–1181, 2010.

[51] M. Ohtsu et al. Recommendation of RILEM TC 212-ACD: acoustic emission and related NDE techniques for crack detection and damage evaluation in concrete - Test method for damage qualification of reinforced concrete beams by acoustic emission. *Materials and Structures*, 43(9):1183–1186, 2010.

[52] A. Parvez and S. Foster. Fatigue behavior of steel-fiber-reinforced concrete beams. *Journal of Structural Engineering*, 141(4), 2015.

[53] S. Paschalis and A. Lampropoulos. Ultra-high-performance fiber-reinforced concrete under cyclic loading. (technical paper). *ACI Materials Journal*, 113(4):419, 2016.

[54] T. Pfister, D. Pfanner, F. Stangenberg, and Y. S. Petryna. Modeling of concrete response under fatigue. *Computational Modelling of Concrete Structures*, pages 295–303, 2003.

[55] A. Pompo, P. Stupak, L. Nicolais, and B. Marchese. Analysis of steel fibre pull-out from a cement matrix using video photography. *Cement and Concrete Composites*, 18(1):3–8, 1996.

[56] N. Pugno, M. Ciavarella, P. Cornetti, and A. Carpinteri. A generalized Paris law for fatigue crack growth. *Journal of the Mechanics and Physics of Solids*, 54(7):1333–1349, 2006.

[57] F. Ranjbaran, O. Rezayfar, and R. Mirzababai. Experimental investigation of steel fiber-reinforced concrete beams under cyclic loading. *International Journal of Advanced Structural Engineering*, 10(1):49–60, 2018.

[58] RILEM Technical Commitee. RILEM TC 162-TDF: Test and design methods for steel fibre reinforced concrete - Uni-axial tension test for steel fibre reinforced concrete. *Materials and Structures*, 34(235):3–6, 2001.

[59] S. Seitl, H. Šimonová, Z. Keršner, and A. Canteli. Evaluation of concrete fatigue measurement using standard and non-linear regression model. *Applied Mechanics and Materials*, 121-126:2726–2729, 2012.

[60] S. Shah and Z. Li. Localization of microcracking in concrete under uniaxial tension. *ACI materials journal*, 91(4):372–381, 1994.

[61] L. Sorelli, A. Meda, and G. Plizzari. Steel fiber concrete slabs on ground: A structural matter. *ACI Structural Journal*, 103(4):551–558, 2006.

[62] M. Soutsos, T. Le, and A. Lampropoulos. Flexural performance of fibre reinforced concrete made with steel and synthetic fibres. *Construction and Building Materials*, 36:704, 2012.

[63] Y. Tanigawa and S. Hatanaka. Stress-strain relations of steel fiber reinforced concrete under repeated compressive load. *Cement and Concrete Research*, 13(6):801–808, 1983.

[64] E. Thorenfeldt, A. Tomaszewicz, and J. Jensen. Mechanical properties of high-strength concrete and application in design. *Proceedings of the Symposium Utilization of High-Strength Concrete*, pages 149–159, 1987.

[65] J. van Mier and M. van Vliet. Uniaxial tension test for the determination of fracture parameters of concrete: state of the art. *Engineering Fracture Mechanics*, 69(2):235–247, 2002.

[66] L. Vandewalle. *Ontwerp van constructiecomponenten: Beton, deel 1 (in Dutch)*. CuDi VTK vzw, KU Leuven, 2017.

[67] R. Vrijdaghs. *Creep of synthetic fiber reinforced concrete - A multi-scale and two-phased approach*. Thesis, KULeuven, 2019.

[68] M. Wevers. Listening to the sound of materials: Acoustic emission for the analysis of material behaviour. *NDT and E International*, 30(2):99–106, 1997.

[69] F. Xiangqian, H. Shaowei, L. Jun, and W. Congjie. Acoustic emission properties of concrete on dynamic tensile test. *Construction and Building Materials*, 114:66–75, 2016.

[70] S. Yin, R. Tuladhar, F. Shi, M. Combe, T. Collister, and N. Sivakugan. Use of macro plastic fibres in concrete: A review. *Construction and Building Materials*, 93(C):180–188, 2015.

[71] R. Zollo. Fiber-reinforced concrete: an overview after 30 years of development. *Cement and Concrete Composites*, 19(2):107–122, 1997.